UQAR

UNIVERSITÉ DU QUÉBEC À RIMOUSKI

Détection et localisation non invasives des fuites des masques N95 par intelligence artificielle et thermographie infrarouge

Mémoire présenté dans le cadre du programme de Maîtrise en ingénierie – volet recherche (3108) en vue de l'obtention du grade de Maître ès sciences (M.Sc.)

Département de mathématique, d'informatique et génie

PAR

© MOHAMED ARBANE

30 janvier 2026

Composition du jury :

— **Pr. Maxime Berger**, président du jury, Université du Québec à Rimouski
— **Pr. Yacine Benahmed**, examinateur , Université du Québec à Rimouski
— **Pr. Jean Brousseau**, directeur de recherche, Université du Québec à Rimouski
— **Pr. Yacine Yaddaden**, codirecteur de recherche, Université du Québec à Rimouski
— **Pr. Xavier Maldague**, codirecteur de recherche, Université Laval

Moi, Mohamed ARBANE, déclare que ce mémoire intitulé, « Détection et localisation non invasives des fuites des masques N95 par intelligence artificielle et thermographie infrarouge » et le travail qui y est présenté sont de ma propre rédaction. Je confirme que :

- Ce travail a été réalisé entièrement et principalement pendant ma candidature à un diplôme de recherche au sein de cette université.
- Lorsque toute partie de cette thèse a été précédemment soumise pour l'obtention d'un diplôme dans cette université, cela a été clairement indiqué.
- Lorsque j'ai consulté les travaux publiés par d'autres, cela est toujours clairement attribué.
- Lorsque j'ai cité la source est toujours indiquée. À l'exception de telles citations, cette thèse est entièrement le fruit de mon propre travail.
- J'ai reconnu toutes les principales sources d'aide.
- Lorsque la thèse est basée sur un travail que j'ai réalisé en collaboration avec d'autres, j'ai clairement indiqué ce qui a été fait par les autres et ce à quoi j'ai contribué moi-même.

Signé :

_____

« *L'important en science n'est pas tant d'obtenir de nouveaux faits que de découvrir de nouvelles façons de penser ceux que l'on possède déjà.* »

William Lawrence Bragg

UNIVERSITÉ DU QUÉBEC À RIMOUSKI

Résumé

Département de mathématique, d'informatique et génie

Maîtrise en ingénierie – volet recherche (3108)

Détection et localisation non invasives des fuites des masques N95 par intelligence artificielle et thermographie infrarouge

par Mohamed ARBANE

La qualité de l'étanchéité des pièces facilaes filtrantes (PFF N95) est cruciale pour garantir une protection optimale contre les particules aéroportées, notamment dans les milieux de soins et industriels. De faibles fuites autour du joint facial peuvent compromettre jusqu'à 50 % de l'efficacité filtrante, mettant en danger l'utilisateur en l'exposant à des agents pathogènes ou à des particules nocives. Les approches traditionnelles de vérification de l'étanchéité (tests qualitatifs au saccharine ou Bitrex, tests quantitatifs PortaCount®) restent limitées à des contrôles ponctuels, coûteux et inadaptés à une surveillance continue lors du port réel du masque.

Cette recherche s'appuie sur deux bases de données complémentaires : *un controlled dataset* de fuites calibrées (0,8 mm–3,5 mm), annoté et mesuré avec précision pour l'entraînement et l'évaluation, et un ensemble de séquences thermographiques capturées auprès de participants humains portant des FFR N95 en conditions réelles (mouvements de tête, port de différents types de masques).

Pour localiser avec précision les fuites, le contour du masque est segmenté dynamiquement à l'aide d'un U-Net optimisé, affiné en temps réel par le Segment Anything Model 2 pour suivre le périmètre sous variations d'angle et de luminosité. Ce contour est ensuite subdivisé en cent régions d'intérêt (ROI) : pour chaque ROI, les variations thermiques liées à l'expiration sont converties en spectrogrammes par transformée de Fourier rapide (FFT). Une méthode de sélection du ROI central, basée sur l'intersection de lignes issues de ROI périphériques et une normalisation du signal, fournit une référence respiratoire stable. En corrélant la signature spectrale de chaque ROI à celle du centre du masque, l'algorithme localise la fuite en moins d'une seconde, avec une précision submillimétrique.

La détection des fuites s'appuie ensuite sur un modèle hybride CNN–SVM qui exploite les caractéristiques des spectrogrammes pour classer chaque segment du contour en « fuite » ou « étanche ». Cette étape atteint un taux de réussite supérieur à 95 % sur les deux jeux de données, confirmant la fiabilité du système.

Pour valider la présence des fuites au niveau pixel, nous recourons à la méthode PBC-OFDI (*Pixel-wise Breathing Cycle Optical Flow Differential Imaging*) : un suivi optique du ROI central extrait les phases d'expiration/inspiration, puis un calcul différentiel des températures génère des cartes de fuite visibles sur un fond atténué, mettant en évidence les zones de fuite.

Testée sur mannequin et participants humains, la solution démontre une robustesse remarquable face aux mouvements, aux variations de masque et aux changements d'éclairage. Non invasive, en temps réel et embarquable, elle ouvre la voie à une surveillance continue des FFR N95 dans les environnements critiques, renforçant significativement la sécurité des utilisateurs.

UNIVERSITY OF QUEBEC AT RIMOUSKI

Abstract

Department of Mathematics, Computer Science and Engineering

Research Master's degree in engineering (3108)

Driver fatigue detection using Artificial Intelligence

by Mohamed ARBANE

Ensuring the seal integrity of Filtering Facepiece Respirators N95 (FFR N95) is essential for optimal protection against airborne particles, especially in clinical and industrial settings. Even minor leaks around the facial seal can reduce the mask's filtration efficiency by up to 50 %, exposing users to pathogens or harmful particulates. Traditional fit-testing methods—whether qualitative (saccharin or Bitrex) or quantitative (PortaCount®)—are limited to intermittent checks, are costly, and cannot continuously monitor mask performance during real-world use.

This work is based on two complementary datasets : a controlled dataset of calibrated leaks (0.8 mm–3.5 mm), precisely annotated and measured for model training and evaluation, and thermal video sequences collected from human participants wearing FFR N95 masks under realistic conditions (head movements, various mask types).

To localize leaks with high precision, the mask contour is dynamically segmented using an optimized U-Net architecture, refined in real time by the Segment Anything Model 2 (SAM2) to track the perimeter despite changes in head pose and ambient lighting. The extracted contour is subdivided into one hundred Regions of Interest (ROIs). For each ROI, respiratory-induced thermal variations are converted into spectrograms via the Fast Fourier Transform (FFT). A rigorous method for selecting the central ROI—based on the intersection of lines drawn between peripheral ROI pairs and subsequent signal normalization—yields a stable breathing reference. By correlating each ROI's spectral signature with that of the central reference, the algorithm pinpoints leak locations in under one second with submillimeter accuracy.

Leak detection is then performed by a hybrid CNN–SVM model that leverages these spectrogram features to classify each contour segment as "leak" or "sealed," achieving over 95 % accuracy on both datasets.

Finally, to validate leak presence at the pixel level, we employ Pixel-wise Breathing Cycle Optical Flow Differential Imaging (PBC-OFDI) : optical-flow tracking of the central ROI extracts expiration and inspiration phases, and differential temperature mapping generates visual leak overlays on a dimmed background, highlighting areas of unfiltered airflow.

Evaluated on both mannequins and human participants, the solution demonstrates remarkable robustness to motion, mask variations, and lighting changes.

Non-invasive, real-time, and deployable, it paves the way for continuous monitoring of FFR N95 masks in critical environments, significantly enhancing wearer safety.

Remerciements

Je tiens tout d'abord à exprimer ma profonde gratitude à mon directeur de recherche, **Jean Brousseau**, pour m'avoir accueilli, guidé et soutenu tout au long de mon parcours de maîtrise. Ses conseils avisés, sa grande disponibilité et sa confiance ont été les piliers de la réussite de ce projet.

Mes remerciements s'adressent également à mes co-directeurs, **Yacine Yaddaden** et **Xavier Maldague**. J'ai énormément appris à leurs côtés ; la pertinence de leurs suggestions et la richesse de leurs idées ont considérablement nourri ma réflexion scientifique. Je les remercie pour le temps précieux qu'ils m'ont accordé.

Je souhaite également remercier chaleureusement **Ali Bahloul** et **Clothilde Brochot** pour leur accompagnement lors de nos réunions. Leurs orientations et leurs idées ont été cruciales pour surmonter les défis rencontrés durant ce travail.

Je tiens à exprimer ma reconnaissance envers tous mes collègues étudiants ayant collaboré au projet sur les masques, avec une mention toute particulière pour **Geoffrey Marchais**. C'est avec lui que j'ai débuté ce projet et partagé la majeure partie de mon temps en laboratoire , je le remercie pour sa collaboration précieuse et pour les moments forts vécus tout au long de ce parcours.

Je tiens à exprimer ma gratitude aux membres du jury, **Yacine Benhamed**, **Maxime Berger**, **Yacine Yaddaden**, **Jean Brousseau** et **Xavier Maldague**, pour avoir accepté d'évaluer ce travail et pour le temps consacré à sa lecture critique.

Sur un plan plus personnel, je remercie mes amis, tant au Canada qu'à l'étranger, qui m'ont encouragé sans relâche durant ce voyage académique. Un grand merci à mes parents et à mes frères pour leur soutien indéfectible malgré la distance.

Enfin, je dédie une mention toute particulière à mon épouse. Tu es ma motivation et mon inspiration quotidienne. Merci d'avoir été mon pilier tout au long de cette maîtrise

Table des matières

Résumé **xii**

Abstract **xvi**

Remerciements **xix**

1 Introduction générale **1**
1.1 Mise en contexte 1
1.1.1 Limites des méthodes actuelles de fit testing 2
1.2 Objectifs 3
1.2.1 Objectif général 3
1.2.2 Objectifs spécifiques 3
1.3 Méthodologie suivie 4
1.3.1 Revue de littérature 5
1.3.2 Définition des axes de travail 5
1.3.3 Étude méthodologique sous conditions contrôlées : surface plane chauffée et mannequin respiratoire (inverser les deux conditions) 5
1.3.4 *Étude in vivo* : visages humains en environnement non contrôlé 6
1.4 Contributions 7
1.4.1 Revues internationales & Conférences internationales . . . 7
1.4.2 Événements et conférences de recherche nationaux 8
1.5 Structure du mémoire 8

2 Revue de littérature **11**
2.1 Les fondamentaux 11
2.1.1 Évaluation critique des méthodes classiques d'ajustement des PFF 12
2.1.2 Analyse spatiale des fuites par thermographie infrarouge 14

2.1.3 Intelligence artificielle et thermographie : vers une détection optimisée des fuites 16
2.2 Bases de données 17
2.2.1 College of Medicine and Public Health, Flinders University [3] 18
2.2.2 Department of Medical Sciences, College of Medicine, The Catholic University of Korea [19] 18
2.2.3 Ruijin Hospital dataset [18] 19
2.2.4 SafeRespirator dataset [24] 20
2.2.5 Banc d'essai dataset [23] 21
2.2.6 Bases de données utilisées 22
2.3 Méthodes et approches existantes 23

3 Advanced Infrared Face Mask Segmentation Using a Custom Lightweight U-Net Model 28
Abstract 29
3.1 Introduction 29
3.2 Related works 30
3.3 Data description 30
3.4 Proposed approach & complexity analysis 30
3.5 Results & discussion 32
3.6 Concluding remarks 33
3.7 Acknowledgment 33

4 Real-Time Leak Localization in N95 Respirators Using Infrared Imaging and Deep Learning with Optimal ROI Signal Correlation 36
Abstract 37
4.1 Introduction 37
4.2 Related Work 38
4.3 Data Collection 39
4.4 Proposed Framework & Methodology 40
4.4.1 Reducing Motion Impact via Segmentation 40
4.4.2 Selection of Region of Interest 41
4.4.3 Correlation Methods 41
4.4.4 Validation via Visualization of Leak Regions 42
4.5 Results & Discussion 42

4.6 Conclusion & Future Work 43
References 43

5 Infrared Imaging and Deep Learning for Enhanced Detection and Localization of Mask Leaks 46
Abstract 47
5.1 Introduction 47
5.2 Related Work 48
5.3 Methodology 49
5.3.1 Experimental Setup 49
5.3.2 Flat Panel and Mannequin Head Configurations 50
5.3.3 Human Subject Testing 50
5.3.4 Infrared Imaging System 51
5.3.5 Data Collection and Preprocessing 51
5.4 Leaks Localisation Methodology & Proposed Approach 52
5.4.1 Mannequin Head : Controlled Leak Localization Methodology 52
5.4.2 Proposed Classification Model 53
5.4.3 Correlation Method 54
5.4.4 Human Participants (Validation Protocol) 55
5.5 Experiments & Results 56
5.5.1 Overview of Metrics and Evaluation Protocol 56
5.5.2 Experimental Metrics 57
5.5.3 Mannequin (Controlled Environment) Results 58
5.5.4 Human Participants Results 59
5.6 Comparative Analysis and Results Discussion 60
5.6.1 Comparative Analysis 60
5.6.2 Results Discussion 61
5.6.3 Conclusion & Future Work 62
References 63

6 Conclusion générale 67
6.1 Objectifs accomplis 68
6.2 Limitations connues 69
6.3 Perspectives et travaux futurs 70
6.4 Retour d'expérience 71

Annexe A **73**

Annexe B **87**

Annexe C **95**

Bibliographie **99**

Table des figures

2.1 Exemples de données et le matériel utilisé [3]. 18
2.2 Exemples de données Kim et al. [19]. 19
2.3 Exemples de données hôpital Ruijin [18]. 20
2.4 Exemples de données SafeRespirator [24]. 21
2.5 Exemples de données banc d'essai [23]. 22
3.1 Illustration of a participant with four distinct facial areas. 30
3.2 Overview of a sample : the original (left) and the labeled image (right). 31
3.3 Comparison of accuracy precision recall and F1-score across models. 31
3.4 The proposed model training on different EPOCHS. 33
3.5 Overview of the proposed model segmentation on IR images. . . 33
4.1 Sample thermal frames from four participants. 39
4.2 Segmentation workflow for N95 masks in IR images using U-Net and SAM2. 40
4.3 Visualization of central ROI placement strategies. 40
4.4 PBC-OFDI visualization for participant 22. 43
4.5 PBC-OFDI visualization for participant 02. 43
5.1 Controlled Testing Setup and Leak Introduction. 50
5.2 Modeling of the Mannequin and Plate Surfaces. 50
5.3 Installation Setup with Simulated Breathing Cycles. 51
5.4 Human Participant Testing Setup. 51
5.5 Segmentation Process using SAM2 and U-Net. 54
5.6 SAM2 Segmentation Architecture. 54

Liste des tableaux

2.1 Comparaison des bases de données utilisées. 23
3.1 COMPARISON BETWEEN THE PROPOSED MODEL AND state-of-the-art U-NET MODELS. 33
4.1 Correlation metrics for participant 29. 41
4.2 Correlation metrics for participant 11. 41
4.3 Correlation metrics for participant 02. 42
4.4 Correlation metrics for participant 22. 42
4.5 Correlation metrics for participant 33. 42
5.1 Summary of Leak Information and Measurements. 51
5.2 Comparison between state-of-the-art model and proposed method. 58
5.3 Correlated ROIs by Pearson Correlation for Two Participants with Different Fit Factors. 61

Liste des abréviations

FFR	**F**iltering **F**acepiece **R**espirator
IR	**I**nfra**R**ed
IA	**I**ntelligence **A**rtificielle
CNN	**C**onvolutional **N**eural **N**etwork
SVM	**S**upport **V**ector **M**achine
ROI	**R**egion **O**f **I**nterest
FFT	**F**ast **F**ourier **T**ransform
SAM2	**S**egment **A**nything **M**odel 2
PFF	**P**iece **F**aciale **F**iltrant
PBC-OFDI	**P**ixel-wise **B**reathing **C**ycle **O**ptical **F**low **D**ifferential **I**maging
IoU	**I**ntersection **o**ver **U**nion
TSI	**T**hermo **S**ystems **I**ncorporated
RGB	**R**ed **G**reen **B**lue
N95 FFR	**N95 F**iltering **F**acepiece **R**espirator
QNFT	**Q**uantitative **F**it **T**est
HEPA	**H**igh **E**fficiency **P**articulate **A**ir
MV	**M**inute **V**entilation
Br	**B**reath **R**ate
ASL 5000	**A**dvanced **S**imulation **L**ung 5000
CAO	**C**onception **A**ssistée par **O**rdinateur
NIOSH	**N**ational **I**nstitute for **O**ccupational **S**afety and **H**ealth
XCorrNorm	**Cross C**orrelation **Norm**alisée
mIoU	**m**ean **I**ntersection **o**ver **U**nion
cGAN	**c**onditional **G**enerative **A**dversarial **N**etwork
SSGAN	**S**emantic **S**egmentation **G**enerative **A**dversarial **N**etwork
U-Net	**U**-shaped **Net**work
StAH	**S**tandard **A**nthropomorphic **H**eadform
Vivo	**V**ivo (en environnement réel)
FF	**F**it **F**actor
Fit-test	**F**it-**T**est (Test d'ajustement quantitatif)
Fit-check	**F**it-**C**heck (Contrôle d'étanchéité)
Bitrex	**B**itrex (agent de test qualitatif)
ATS	(Format de données propriétaire utilisé par les systèmes infrarouges FLIR)
AUC	**A**rea **U**nder the **C**urve
SC	**S**eparable **C**onvolutions
GLCM	**G**ray-**L**evel **C**o-occurrence **M**atrix

NIR	**N**ear-**I**nfra**R**ed
3D-CNN	**3D C**onvolutive **N**eural **N**etwork
ResNet	**Res**idual **Net**work
ES	**E**dge **S**egmentation
IRSST	**I**nstitut de **R**echerche **R**obert-**S**auvé en **S**anté et en **S**écurité du **T**ravail
FI3E	**F**orum **I**nnovation, **I**ngénierie, **I**nformatique et **E**ntrepreneuriat
SNR	**S**ignal-to-**N**oise **R**atio
OSHA	**O**ccupational **S**afety and **H**ealth **A**dministration
PPE	**P**ersonal **P**rotective **E**quipment
VIA	**V**GG **I**mage **A**nnotator
TP / FP / FN	**T**rue **P**ositive / **F**alse **P**ositive / **F**alse **N**egative
mAP	**m**ean **A**verage **P**recision

À ma famille et à mes proches, je dédie ce projet en vous remerciant chaleureusement pour votre amour et votre encouragement.

Chapitre 1

Introduction générale

1.1 Mise en contexte

Les pièces faciales filtrantes (PFF) N95 jouent un rôle critique pour la protection respiratoire en milieu de soins, en particulier lors d'épidémies et pandémies [10]. Leur efficacité dépend étroitement de l'étanchéité du joint facial : même de petites fuites entre le masque et le visage peuvent réduire drastiquement la performance de filtration [36]. Des études montrent que les fuites au niveau du joint facial contribuent plus à l'exposition de l'utilisateur qu'une éventuelle pénétration à travers le matériau filtrant [33, 13]. Par exemple, un N95 mal ajusté pourrait laisser passer entre 30 % et 95 % des aérosols, contre un niveau de fuite minime pour un respirateur correctement testé et ajusté, ce qui correspond à un taux d'infection d'environ 12% avec masque ajusté, comparé à 42–80 %, sans ajustement adéquat. Ces chiffres illustrent combien une bonne étanchéité est indispensable pour assurer la protection du porteur. En contexte hospitalier et de réponse à une pandémie (comme la COVID-19), où les soignants sont fortement exposés, garantir l'ajustement efficace des N95 revêt une importance capitale pour réduire les transmissions [28].

1.1.1 Limites des méthodes actuelles de fit testing

Avant l'utilisation d'un masque N95, des tests d'ajustement standardisés (fit tests) sont généralement réalisés pour valider l'adéquation de la PFF N95 avec le porteur. Il en existe deux types principaux :

— **Tests qualitatifs** : par exemple les essais à la saccharine ou au Bitrex où l'on diffuse un aérosol au goût sucré ou amer autour du masque ; si le porteur perçoit ce goût, l'ajustement est jugé défaillant. Ces méthodes qualitatives fournissent donc une évaluation subjective de l'ajustement du masque.

— **Tests quantitatifs** : typiquement, à l'aide d'un appareil comme le PortaCount®, qui mesurent objectivement le rapport de concentration de particules aérosolisées à l'intérieur et à l'extérieur du masque, fournissant un indice numérique (facteur d'ajustement) de l'étanchéité [6].

Si les tests quantitatifs sont considérés comme la référence en termes de fiabilité, **ils nécessitent un équipement spécialisé, du temps et du personnel formé**. En pratique, les protocoles classiques de test d'ajustement impliquent souvent un contact physique direct entre l'appareil de test et le masque (sondes, adaptateurs, etc.). C'est le cas pour chaque installation de masque et l'assistance de personnel qualifié, ce qui les rend fastidieux et chronophages [41]. De plus, cette approche invasive soulève des préoccupations de contamination croisée et de risque de transmission d'infections lors des tests, un problème exacerbé en période où il est crucial de limiter les interactions rapprochées. Par conséquent, ces méthodes conventionnelles ne se prêtent pas à une surveillance régulière ou continue de l'ajustement : elles offrent un instantané de l'ajustement dans des conditions contrôlées, mais ne permettent pas d'assurer un suivi en temps réel pendant le port du masque [38]. En pratique quotidienne, les utilisateurs ont tendance à s'appuyer sur contrôle d'étanchéité (fit check) (vérification à l'aide des mains ou par de grandes inspirations une fois le masque en place) ; or, des recherches ont montré que ces contrôles sommaires par le porteur sont peu fiables

et manquent de sensibilité, ne parvenant pas à détecter de nombreuses fuites. Il existe donc un besoin criant de méthodes de vérification de l'ajustement plus rapides, non invasives, sans contact et continues, pouvant être déployées facilement en milieu clinique sans compromettre la sécurité.

1.2 Objectifs

Au regard des limites des procédures de tests d'ajustement traditionnelles , il devient impératif de disposer d'un outil rapide, non invasif et fiable pour vérifier l'étanchéité des respirateurs à pièce faciale filtrante N95 (FFR N95). Cette thèse s'inscrit dans cette dynamique en proposant un cadre intégrant l'imagerie infrarouge (IR) et l'intelligence artificielle (IA) pour détecter et localiser les fuites en temps réel. Les objectifs ci-après ont été formulés pour balayer de façon cohérente l'ensemble du cycle de conception, de validation et d'application du système.

1.2.1 Objectif général

Développer un cadre IR-IA capable de détecter et de localiser, en temps réel, les fuites se produisant sur un FFR N95, de manière à réduire la dépendance aux fit tests conventionnels et permettent de fournir une évaluation continue de l'étanchéité dans les milieux cliniques et industriels.

1.2.2 Objectifs spécifiques

1. **Segmentation dynamique du masque** : Concevoir un réseau de segmentation IR léger, basé sur un U-Net à convolutions séparables et enrichi des mécanismes d'attention du *Segment Anything Model 2*(SAM2), afin d'extraire automatiquement et en continu le contour du masque, malgré les mouvements de tête et les fluctuations thermiques.

2. **Classification binaire fuite / pas-de-fuite** Mettre en œuvre une chaîne de traitement combinant :
   — l'extraction de caractéristiques spatio-temporelles via *ResNet-50*,
   — un classifieur robuste (SVM) entraîné pour distinguer les états *fuite* et *pas-de-fuite* avec une précision minimale visée de $\geq$ 95 % sur des scénarios variés.
3. **Cartographie pixel-par-pixel de la fuite** Développer une méthode de corrélation spectrale « contour centre ». Elle s'appuie sur une analyse FFT suivie de corrélations (Pearson, Spearman, Kendall, XCorrNorm) entre les signaux thermiques issus de régions d'intérêt (ROI) périmétriques et celui du centre respiratoire, afin de quantifier l'intensité de la fuite pour chaque pixel. La visualisation finale s'effectue par projection *PBC-OFDI*.
4. **Validation expérimentale multi-niveaux** Évaluer l'ensemble du cadre sur trois plateformes :
   — **surfaces planes chauffées**, pour l'étalonnage des seuils thermiques ;
   — **mannequins respiratoires**, reproduisant divers débits et scénarios de fuite ;
   — **participants humains**, impliquant des respirations semi-contrôlées et des mouvements naturels.

   Les performances (sensibilité, spécificité, temps de traitement) seront comparées aux facteurs d'ajustement mesurés par *PortaCount*®.

1.3 Méthodologie suivie

Dans ce projet, nous avons adopté une approche méthodologique progressive afin d'approfondir la problématique des fuites sur les PFF N95 et d'atteindre les objectifs définis tout en capitalisant sur les recherches existantes. Les étapes principales retenues sont détaillées dans les sous-sections qui suivent.

1.3.1 Revue de littérature

Cette phase consiste avant tout à passer en revue un ensemble d'articles de conférences et de revues scientifiques portant sur la détection des fuites des PFF N95 à l'aide de l'imagerie infrarouge et de l'intelligence artificielle. Elle nous offre une vision approfondie de l'état de l'art et des progrès déjà accomplis dans ce domaine, tout en nous aidant à comprendre les différentes étapes méthodologiques employées pour développer ces systèmes. Grâce à cette analyse, nous pourrons évaluer les performances des approches existantes, identifier leurs limites ainsi que les pistes d'amélioration nécessaires pour concevoir un dispositif de détection optimal. Cette étape est donc cruciale pour orienter nos futurs axes de recherche. Plus spécifiquement, notre revue de littérature portera sur les techniques de traitement d'images thermiques et les modèles d'IA appliqués à la localisation et à la classification des fuites sur les PFF N95.

1.3.2 Définition des axes de travail

Pour développer un système fiable de détection des fuites sur les respirateurs à pièce faciale filtrante N95, il est essentiel de bien comprendre l'influence du cycle respiratoire—alternance inspiration / expiration—sur la distribution thermique autour du contour du masque. Cette compréhension guide le choix des capteurs, des algorithmes et des scénarios d'essai. Deux axes expérimentaux complémentaires ont donc été définis :

1.3.3 Étude méthodologique sous conditions contrôlées : surface plane chauffée et mannequin respiratoire (inverser les deux conditions)

— **Objectif :** Analyser, dans un contexte dépourvu de bruit externe, la corrélation entre le signal thermique des fuites calibrées (contour) et le signal respiratoire (centre).

— **Dispositif :**

1. Utilisation de données préalablement construites par l'équipe de projet : surfaces planes et mannequins équipés d'un système mécanique reproduisant le cycle respiratoire humain (même fréquence et même volume courant).
2. Acquisition simultanée d'images IR et de mesures de débit afin de disposer d'un signal respiratoire de référence parfaitement aligné temporellement.

— **Résultats :** Quantifier la relation spectrale et temporelle entre les séries thermiques "contour" et "centre" (coefficients de corrélation, retards de phase, signatures fréquentielles).

— Établir les seuils et paramètres du module de corrélation qui serviront de base au transfert vers l'étude in *vivo*.

1.3.4 *Étude in vivo* : visages humains en environnement non contrôlé

— **Objectif :** Adapter et valider le système construit sur mannequins aux conditions réalistes : morphologies variables, mouvements.

— **Dispositif :**

1. Synchronisation avec les mesures de Facteur d'ajustement par PortaCountR® pour constituer la référence.
2. Intégration d'un module de segmentation dynamique (U-Net allégé + SAM2) afin de maintenir l'extraction précise du contour malgré les mouvements naturels de la tête et les déplacements du masque.

— **Résultats :**

1. Démontrer que la segmentation intégrée protège la performance en conditions réelles en isolant correctement le masque à chaque séquence.

2. Vérifier que la méthode de corrélation contour/centre conserve une détection et une localisation fiables.

1.4 Contributions

Les travaux réalisés durant ma maîtrise ont donné lieu à plusieurs publications scientifiques et présentations qui reflètent et non reflèctent chacune des étapes méthodologiques du mémoire :

1.4.1 Revues internationales & Conférences internationales

— **Arbane, M.**, Yaddaden, Y., Brousseau, J., Brochot, C., Marchais, G., Bahloul, A. and Maldague, X., 2025. *Real-Time Leak Localization in N95 Respirators Using Infrared Imaging and Deep Learning with Optimal ROI Signal Correlation*. In EEITE 2025 – the 6th IEEE International Conference in Electronic Engineering and Information Technology. IEEE. (Statut : Présenté)

— **Arbane, M.**, Yaddaden, Y., Brousseau, J., Marchais, G., Brochot, C., Bahloul, A. and Maldague, X., 2025. *Infrared Imaging and Deep Learning for Enhanced Detection and Localization of Mask Leaks*. Infrared Physics & Technology, Elsevier . (Statut : Soumis)

— Marchais, G., **Arbane, M**., Topilko, B., Brousseau, J., Brochot, C., Yaddaden, Y., ... & Maldague, X. (2024). SafeRespirator : Comprehensive Database for N95 Filtering Facepiece Respirator Leak Detection Including Infrared, RGB Videos, and Quantitative Fit Testing. IEEE Access.(Statut : Accepté)

— Marchais, G., Topilko, B., **Arbane, M.**, Brousseau, J., Brochot, C., Yaddaden, Y., ... & Maldague, X. (2024, October). A Test Bench for Replicating Human Breathing : Evaluating Thermal Effects of N95 Filtering Facepiece Respirator Leaks–Preliminary Findings. In 2024 9th International Conference on Computer Science and Engineering (UBMK) (pp. 695-700). IEEE.(Statut : Accepté)

— **Arbane, M.**, Marchais, G., Topilko, B., Yaddaden, Y., Brousseau, J., Brochot, C., Bahloul, A. and Maldague, X., 2024, October. *Advanced Infrared Face Mask Segmentation Using a Custom Lightweight U-Net Model*. In 2024 IEEE International Multi-Conference on Smart Systems & Green Process (IMC-SSGP) (pp. 1-6). IEEE.(Statut : Présenté)

1.4.2 Événements et conférences de recherche nationaux

— **Arbane, Mohamed**. "Amélioration de la segmentation sémantique faciale en IR. Forum Innovation, Ingénierie, Informatique et Entrepreneuriat (FI3E 2024) a reçu le prix du meilleur poster de recherche".

— **Mohamed Arbane** et Barthelemy Topilko de l'UQAR : "Développement de modèles multiphysiques finals pour l'étude du flux d'air et des effets thermiques pendant l'utilisation de masques N95 et intégration de l'IA ". Présentation à l'association québécoise pour l'hygiène, la santé et la sécurité du travail (AQHSST 2024)

1.5 Structure du mémoire

Ce mémoire est découpé comme suit :

— Le chapitre Revue de littérature une revue de la littérature liée à la thématique est présentée, ainsi qu'une discussion des limites identifiées.

— Le Chapitre 3 présente l'article accepté à la conférence IEEE, dans lequel nous introduisons une variante allégée de l'architecture U-Net. Spécialement adaptée aux images infrarouges, cette version réduit significativement le nombre de paramètres tout en améliorant l'IoU par rapport aux modèles de l'état de l'art. Le chapitre décrit l'ensemble du processus : conception du réseau, stratégie d'entraînement et évaluation sur la base de données Vivo.

— Le Chapitre 4 s'appuie sur un second article IEEE. Nous y montrons comment l'ajout du module d'attention SAM2 renforce la robustesse de la segmentation/reconnaissance lors des mouvements de la tête et des déplacements du masque. Après l'extraction dynamique du contour, nous proposons une méthode de visualisation de la fuite par corrélation spectrale, puis comparons systématiquement notre approche aux techniques de visualisation classiques. Les gains obtenus en précision et en temps de traitement sont discutés, ainsi que les limitations restantes (notamment la sensibilité aux variations thermiques rapides).

— Le Chapitre 5 correspond à l'article soumis au journal Infrared Physics & Technology (Elsevier). Nous y déployons les modèles mis au point dans le Chapitre 4 sur des données collectées auprès de participants humains. Après avoir justifié le choix des seuils de corrélation—déterminés à partir des essais en environnement contrôlé—nous évaluons les performances par rapport aux fit tests mesurés avec le PortaCount®. Nous présentons en outre un classifieur ResNet-SVM permettant de discriminer automatiquement les signaux de fuite/pas-de-fuite, et discutons la transférabilité du cadre IR-IA vers la pratique clinique.

— La Conclusion générale propose un bilan des techniques examinées, en

valorisant leurs forces et en identifiant leurs limites, et suggère des perspectives à explorer dans notre recherche.

— L'Annexe A présente l'article scientifique intitulé « SafeRespirator : Comprehensive Database for N95 Filtering Facepiece Respirator Leakage Detection Including Infrared, RGB Videos, and Quantitative Fit Testing ». Dans le cadre de ce travail, mes contributions spécifiques ont consisté à élaborer une méthode originale de calibration entre la caméra thermographique infrarouge et la caméra RGB visuelle, ainsi qu'à synchroniser efficacement ces deux dispositifs. J'ai également développé les procédures d'extraction des informations thermiques pertinentes à partir des images capturées et mené l'analyse approfondie de ces données.

— L'Annexe B présente les résultats issus d'une première expérimentation réalisée en environnement contrôlé, visant à mieux comprendre les caractéristiques thermiques associées aux fuites sur les PFF N95. Cet article constitue une étape préliminaire essentielle pour le développement des méthodes de détection et de localisation des fuites dans des conditions maîtrisées.

— L'Annexe C présente le premier poster présenté lors de l'événement FI3E à l'UQAR , et le deuxième poster présenté à la conférence WIAC 2025 en Italie qui se concentre davantage sur les résultats avancés, la validation expérimentale et les perspectives futures du projet.

Chapitre 2

Revue de littérature

Ce chapitre présente un état de l'art des méthodes élaborées par plusieurs équipes pour détecter et localiser les fuites des PFF N95.

La section 2.1 présente les approches fondamentales, suivie par la section 2.2 qui décrit les principales bases de données utilisées. Ensuite, la section 2.3 examine le travail effectué dans d'autres recherches, et une discussion sur les limitations des approches présentées dans ce chapitre.

2.1 Les fondamentaux

Des études montrent de façon constante que la moindre fuite au joint facial peut drastiquement compromettre la protection offerte par les PFF N95 . Les fuites au joint facial ont été identifiées comme un contributeur majeur au nombre d'aérosols potentiellement infectieux pénétrant dans un PFF, dépassant souvent l'efficacité intrinsèque du filtre [7, 27]. En d'autres termes, même un PFF N95 très performant offre peu d'avantages si l'air contourne via des interstices autour du visage. Des mesures démontrent que la majeure partie des fuites internes d'aérosol se produit via ces interstices plutôt qu'à travers le média filtrant lui-même [27]. Par conséquent, même de petites fuites peuvent augmenter significativement l'exposition du porteur aux agents pathogènes aéroportés [4].

Les études épidémiologiques et de modélisation soulignent les risques sanitaires posés par un mauvais ajustement du PFF. Dans les milieux cliniques,

un PFF N95 dont le joint n'est pas adéquat peut offrir beaucoup moins que son niveau nominal de 95%. Une étude par modélisation a prédit qu'un PFF N95 dont l'ajustement a été testé ou n'a pas été testé (présentant des fuites faciales typiques) ne réduirait la probabilité d'infection qu'à environ 42–80%, contre environ 12% pour un PFF N95 correctement fit-testé [5]. Des essais cliniques lors d'épidémies virales ont confirmé ces préoccupations : un large essai randomisé n'a trouvé aucune différence significative de taux d'infection grippale entre les porteurs de N95 non fit testés et les porteurs de masques chirurgicaux, suggérant que des PFF N95 mal ajustés peuvent ne pas mieux protéger que des masques chirurgicaux [29, 17]. En contraste, une autre étude a montré que les N95 fit-testés offraient une protection significativement meilleure contre les infections virales respiratoires que les PFF non fit-testés [25].

Ces résultats soulignent que les défaillances d'ajustement et les fuites compromettent de manière critique la protection respiratoire, exposant potentiellement le porteur à des agents infectieux malgré la haute capacité de filtration des FFR N95. Assurer une bonne étanchéité faciale s'avère ainsi aussi crucial que l'efficacité du filtre pour réduire le risque de pathogènes aéroportés.

2.1.1 Évaluation critique des méthodes classiques d'ajustement des PFF

Les procédures de test ajustement (quantitatif ou qualitatif) et de contrôle d'ajustement pas l'utilisateur sont utilisées pour détecter les fuites de PFF, mais chacune présente des limites. Les *fit-check* qualitatifs sont de simples tests effectués par l'utilisateur, par exemple, test à pression positive ou test à pression négative(expiration douce avec la sortie obturée pour sentir un flux d'air sortant). Les utilisateurs peuvent également réaliser des test d'ajustement qualitatif à base d'aérosol, en s'exposant à un aérosol au goût amer ou sucré (Bitrex®, saccharine) et en vérifiant s'il pénètre à l'intérieur du masque. Bien que peu onéreuses et simples, ces méthodes sont intrinsèquement subjectives et sujettes

à l'erreur humaine [35, 30]. La capacité d'un porteur à percevoir une fuite (par le goût, l'odorat ou le ressenti) varie, et les fuites petites ou modérées peuvent passer inaperçues. Des études ont montré que se fier aux *fit-checks* auto-réalisés uniquement n'est pas fiable – jusqu'à 40 % des utilisateurs n'arrivent pas à déterminer avec précision si le masque est correctement ajusté [35]. Dans une étude multicentrique, 30 % des travailleurs de la santé qui pensaient que leur N95 était bien ajusté (après un fit check réussi) se sont révélés présenter un ajustement insatisfaisant lors de tests quantitatifs [8]. De tels cas de faux sentiment de sécurité illustrent les limites de détection des vérifications qualitatives. À l'inverse, les tests qualitatifs peuvent parfois être trop sensibles – une étude a noté que les *fit tests* au Bitrex ont déclenché des échecs injustifiés dans un nombre significatif de cas [30]. Globalement, la détection qualitative des fuites dépend fortement de l'utilisateur, avec des résultats affectés par la technique du porteur, son acuité sensorielle et même sa morphologie faciale.

En revanche, le *fit-test* quantitatif fournit une mesure objective des fuites du PFF. Des dispositifs comme le TSI PortaCount® utilisent des compteurs de particules pour comparer les concentrations d'aérosols à l'extérieur et à l'intérieur du masque, fournissant un *fit factor* [16]. Un *fit factor* d'au moins 100 (indiquant $\geq$ 99 % de réduction des aérosols) est requis pour réussir un *fit-test* des PFF N95 [42]. Le *fit-test* quantitatif est considéré comme le « *gold standard* » pour évaluer l'ajustement d'un PFF, car il peut détecter de très petites fuites que les porteurs ne remarqueraient pas [16, 40]. Contrairement à un contrôle qualitatif de type *pass/fail*, le PortaCount fournit un score numérique, permettant de comparer différents PFF et conditions. Cependant, des contraintes pratiques limitent l'utilisation des testeurs quantitatifs : les instruments sont spécialisés et coûteux, et les tests doivent être menés par du personnel formé dans des conditions contrôlées. En général, un *fit-test* formel n'est réalisé que lors de l'ajustement initial, puis annuellement, laissant aux utilisateurs des fit checks entre les

tests. De plus, les tests quantitatifs sont généralement effectués dans des conditions statiques – le porteur effectue une série d'exercices – ce qui peut ne pas capturer des fuites survenant lors d'une activité plus intense.

De manière cruciale, un *fit-test* standard ne permet pas de localiser la fuite, il ne fournit qu'une mesure global du facteur d'ajustement, sans visualisation possible des sites de fuite [9]. En résumé, bien que le TSI PortaCount et les appareils similaires soient très sensibles, leur coût, la nécessité d'étalonnage et la présence d'un aérosol ambiant, ainsi que l'incapacité à localiser la fuite, soulignent la nécessité d'approches de détection des fuites plus pratiques et informatives.

2.1.2 Analyse spatiale des fuites par thermographie infrarouge

Les panoplies de recherche ont exploré la thermographie infrarouge (IR) comme technique novatrice pour visualiser et localiser les fuites de PFF, surpassant les méthodes conventionnelles. Cette approche exploite la différence de température entre l'air chaud expiré et l'air ambiant plus frais. Lorsqu'un individu expire en portant un PFF N95, toute fuite génère un panache thermique détectable par caméra IR. Par exemple, un masque bien scellé force l'air chaud expiré à passer par le média filtrant, tandis qu'une fuite au niveau de l'arête du nez produit un point chaud visible sur image infrarouge.

Roberge et al. (2011) ont mené une étude pilote en utilisant la vidéo IR lors de fit-tests quantitatifs : sur 48 tests, la caméra détecta 49 fuites d'expiration réparties sur 39 tests, avec 71% des fuites localisées au niveau nasal ou malaire [31]. Tous les échecs au fit-test coïncidaient avec des fuites visibles en IR, et des fuites mineures étaient également observées dans plusieurs tests validés, suggérant une sensibilité plus élevée que celle des méthodes quantitatives [31, 39]. De plus, les *fit factors* étaient significativement plus élevés dans les tests sans fuite IR détectée ($p=0.01$), démontrant une corrélation fiable entre signal thermique et performances [31].

Les travaux de Harber et al. (2015) ont amélioré le dispositif expérimental en utilisant une caméra IR haute résolution et en stabilisant la tête du sujet pour réduire les mouvements [12]. Ils ont introduit un score de fuite IR (1 à 4) et établi une corrélation générale entre ce score et le fit factor mesuré par PortaCount. Toutefois, ils ont souligné que la thermographie IR ne permettait pas une quantification continue du débit de fuite équivalente au *fit factor*, notamment en raison de la variabilité des signatures thermiques liée à la sensibilité de la caméra, aux conditions ambiantes et à la dynamique du flux d'air [39].

Plus récemment, les progrès technologiques ont permis un renforcement de la sensibilité et de l'applicabilité de l'IR. Les caméras modernes offrent une meilleure résolution thermique, permettant de détecter de minuscules fuites. Des protocoles optimisés — comme l'utilisation d'un fond froid et le focalisation sur la surface du PFF plutôt que sur la peau — ont amélioré le contraste thermique. Chapman et al. (2023) ont par exemple montré qu'un changement de température mesuré sur le masque lui-même était plus fiable que sur la peau, qui ne se refroidit pas suffisamment pour les petites fuites [2]. Des techniques comme la soustraction d'images et le moyennage de frames ont rendu possibles l'identification de signaux de respiration ténus. Certaines études intègrent également la modélisation CFD pour valider que les points chauds thermiques correspondent à des trajectoires de fuite d'air.

Dans l'ensemble, la thermographie IR enrichit l'évaluation des fuites en offrant des informations à la fois visuelles et spatiales : elle détecte non seulement la présence de fuites, mais localise et suit leur évolution pendant la respiration, une capacité essentielle pour l'optimisation de la conception des PFF et la formation des utilisateurs [22, 11]. Néanmoins, son utilisation pratique reste limitée par le coût du matériel, la nécessité d'immobiliser le sujet, et l'expertise requise pour interpréter les images thermiques. Ces défis ont accéléré le développement d'approches automatisées, détaillées dans la section suivante.

2.1.3 Intelligence artificielle et thermographie : vers une détection optimisée des fuites

Pour exploiter pleinement l'imagerie infrarouge dans la détection des fuites de PFF, les chercheurs se tournent de plus en plus vers les techniques d'intelligence artificielle. Les algorithmes d'IA, en particulier sous la forme de l'apprentissage automatique et l'apprentissage profond, peuvent traiter les motifs thermiques complexes et automatiser l'identification des fuites ou d'un mauvais ajustement, améliorant à la fois la rapidité et la cohérence de l'analyse [34].

Des études récentes ont exploré un éventail d'approches, allant de modèles ML classiques à des réseaux neuronaux profonds de pointe, appliqués à des images ou vidéos thermiques de porteurs de masque.

Un axe de recherche utilise l'apprentissage supervisé pour classifier si l'ajustement d'un PFF donné est acceptable ou non («pass/fail») à partir d'images thermiques. Siah et al., par exemple, ont entraîné un réseau neuronal convolutif (CNN) [26] à reconnaître les motifs de fuite dans des images infrarouges de porteurs de masques N95 [34]. Dans leur étude, des images IR ont été collectées auprès de sujets qui avaient échoué aux fit tests qualitatifs, et un modèle CNN devait distinguer les cas présentant des fuites des cas bien étanches. En raison d'un ensemble de données limité, la précision du modèle était modeste, de l'ordre de 20–30% de détection (variant selon l'angle de la caméra), et les auteurs ont signalé le surapprentissage (*overfitting*) comme une préoccupation compte tenu du faible échantillon d'entraînement [34]. Cela a mis en évidence la nécessité de jeux de données plus vastes et de recourir à l'augmentation des données d'entraînement pour former les détecteurs de fuites thermiques.

Bari et al. (2022) ont proposé une approche utilisant Mask R-CNN pour localiser des zones de fuite dans des vidéos IR de PFF N95 [1]. Leur méthode a permis de détecter et segmenter automatiquement les fuites image par image.

Une autre avancée porte sur l'analyse en temps réel des vidéos thermographiques à l'aide du deep learning. Un système basé sur 3D-CNN a montré qu'un

fit-check automatisé est possible en temps réel, avec une AUC [15] élevée (0,986) pour différents types de mauvais ajustement [34].

Grâce à ces avancées, l'intégration de l'IA a considérablement amélioré l'automatisation et la rigueur de la détection thermographique des fuites. L'analyse guidée par l'apprentissage automatique élimine le biais d'observation dans l'interprétation des images thermiques, et permet de détecter des motifs de fuite trop subtils pour être visibles à l'œil nu. Néanmoins, d'importantes lacunes de recherche subsistent, motivant ainsi la présente étude. Premièrement, aucune solution existante n'offre encore un dispositif complet capable de localiser la gravité des fuites selon une métrique techniquement ou cliniquement pertinente (par exemple, le débit ou le volume de fuite) directement sur le terrain. Deuxièmement, la robustesse et la généralisabilité constituent des problématiques majeures. Les modèles entraînés sur des types spécifiques de PFF et sur de petits groupes de sujets peuvent présenter des performances limitées face à des formes de visage différentes, à divers modèles de PFF ou à des scénarios de mouvement variés. Enfin, la majorité des recherches actuelles restent encore au stade de prototype. Aucun outil n'a encore été déployé à grande échelle pour une vérification de routine de l'ajustement des PFF, et il manque des études à grande échelle démontrant l'efficacité de la thermographie par IA sur le terrain.

2.2 Bases de données

Pour traiter efficacement la problématique de la détection des fuites dans les PFF N95 par thermographie infrarouge, il est crucial de disposer des bases de données soigneusement organisées. Ces dernières, issues de travaux et d'expérimentations antérieurs, offrent un socle fiable pour concevoir et valider les algorithmes de repérage des fuites.

2.2.1 College of Medicine and Public Health, Flinders University [3]

Dans leur base de données, Chapman et al.[3] ont collecté des images thermiques auprès de 48 professionnels de santé dont 75 % de femmes , 25% d'hommes lors de cliniques de test d'étanchéité quantitatives, en capturant une seule image en fin d'inspiration par participant. Les images ont été acquises avec une caméra thermique FLIR One Gen 3 pour iOS (résolution de 160 × 120 px, sensibilité de 60 mK) montée sur un iPad et positionnée à 40–60 cm du visage du porteur, les fichiers JPG natifs ont été exportés au format TIFF et une zone d'intérêt de 60 × 138 px autour du contour du PFF a été extraite semi-automatiquement pour l'analyse . Le jeux de données n'est pas accessible en libre accès. Quelques exemples de données collectées et ainsi que le matériel utilisé sont illustrés à la figure 2.1.

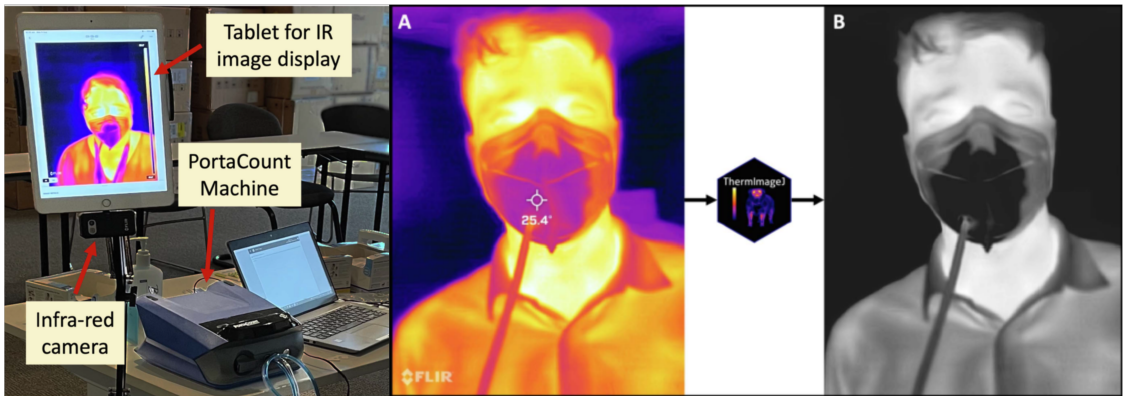

FIGURE 2.1 – Exemples de données et le matériel utilisé [3].

2.2.2 Department of Medical Sciences, College of Medicine, The Catholic University of Korea [19]

Kim et al. [19] ont enregistré des vidéos thermiques de 50 participants adultes en bonne santé (39 femmes, 11 hommes ; âgés de 19 à 65 ans) dans une pièce maintenue à 20 °C, en utilisant une caméra thermique FLIR ONE Pro (fréquence d'images de 8,7 Hz, résolution de 1440 × 1080) montée sur un iPhone Xs à une distance fixe de 35 cm du visage . Ils ont évalué cinq types de masque : masque

chirurgical standard, KF-Anti-Droplet (KF-AD), KF80, KF94 et KF99, approuvés par le ministère coréen de la Sécurité des aliments et des Médicaments . Pour chaque type de masque et quatre méthodes de port différentes, ils ont capturé des vidéos de cycle respiratoire de 4 secondes (inhalation/exhalation à intervalles de 2 s), répétées cinq fois, soit 100 vidéos par participant et 5 000 vidéos au total. La figure 2.2 montre plusieurs exemples . L'ensemble complet de vidéos est librement accessible [1].

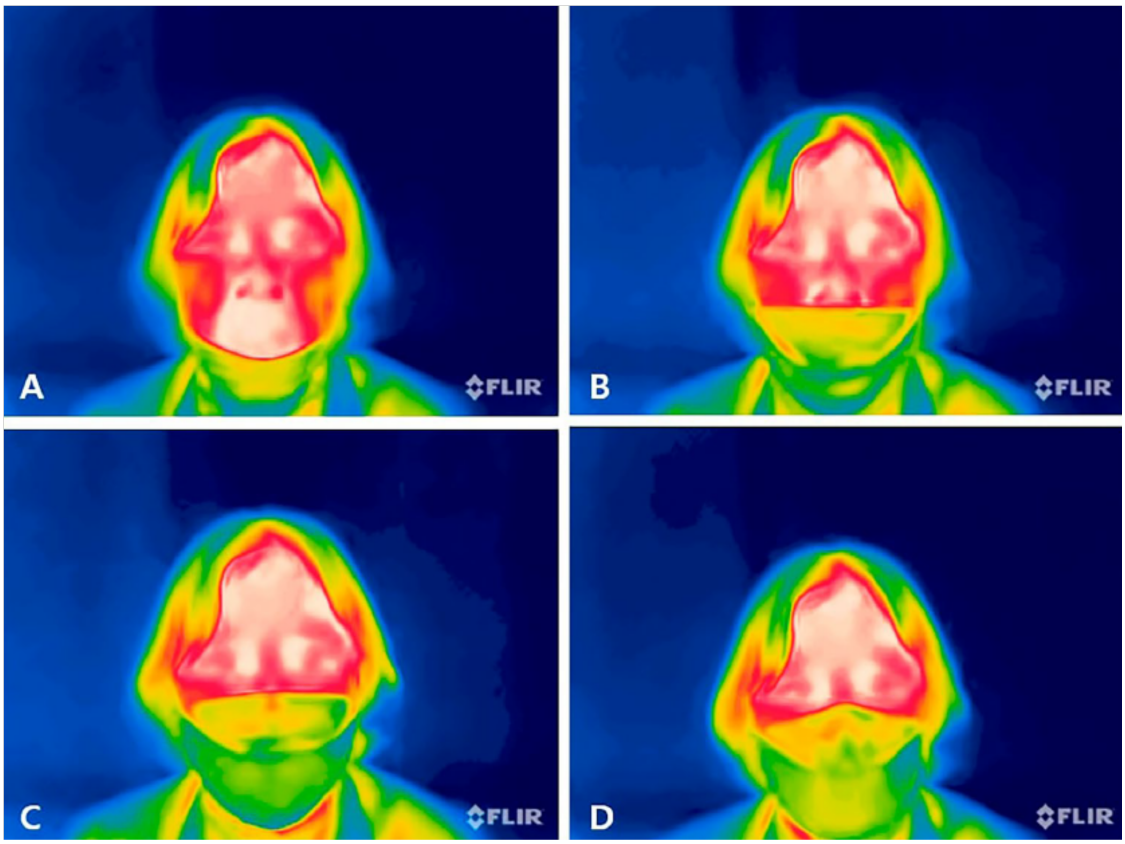

FIGURE 2.2 – Exemples de données Kim et al. [19].

2.2.3 Ruijin Hospital dataset [18]

Jiang et al. ont collecté des vidéos respiratoires en mode double (thermique + RGB) auprès de 73 patients hospitalisés et ambulatoires à l'hôpital Ruijin, en utilisant une caméra thermique FLIR One connectée à un smartphone Android

1. https://doi.org/10.5281/zenodo.10244188

. Pour chaque participant, ils ont enregistré deux séquences de 20 secondes à 10 Hz, puis les ont segmentées et suréchantillonnées en 4 217 séquences respiratoires de 100 images (10 s) chacune. Quelques exemples de données collectées sont illustrés à la figure 2.3 . Bien que les auteurs indiquent que le jeu de données sera publié pour un usage non commercial après acceptation de l'article et fournissent des vidéos de démonstration à l'adresse [2], l'ensemble complet de données n'est pas partagé en accès libre.

FIGURE 2.3 – Exemples de données hôpital Ruijin [18].

2.2.4 SafeRespirator dataset [24]

La base SafeRespirator propose un ensemble de données ouvert et calibré, comprenant 35 secondes d'images synchronisées IR et RGB pour chaque essai,

2. https://doi.org/10.6084/m9.figshare.12028032

capturées en quatre angles (face, dessus, gauche, droite) à 50 cm du visage figure. 2.4 , la caméra infrarouge enregistre en TIFF/ATS à une résolution de 1280×1024 px et 30 ips, et la caméra RGB en MP4 à un débit similaire. Au total, 62 participants (36 femmes, 26 hommes) ont porté quatre modèles différents de FFR N95 et réalisé deux tests quantitatifs de fit (PortaCount 8038) avant et après chaque enregistrement. La base contient 1054 vidéos IR, 1054 vidéos RGB et 496 résultats de QNFT (8 To de données brutes) organisés par participant et modele de PFF N95. Elle est accessible[3] (accès réservé aux institutions académiques sous condition d'approbation).

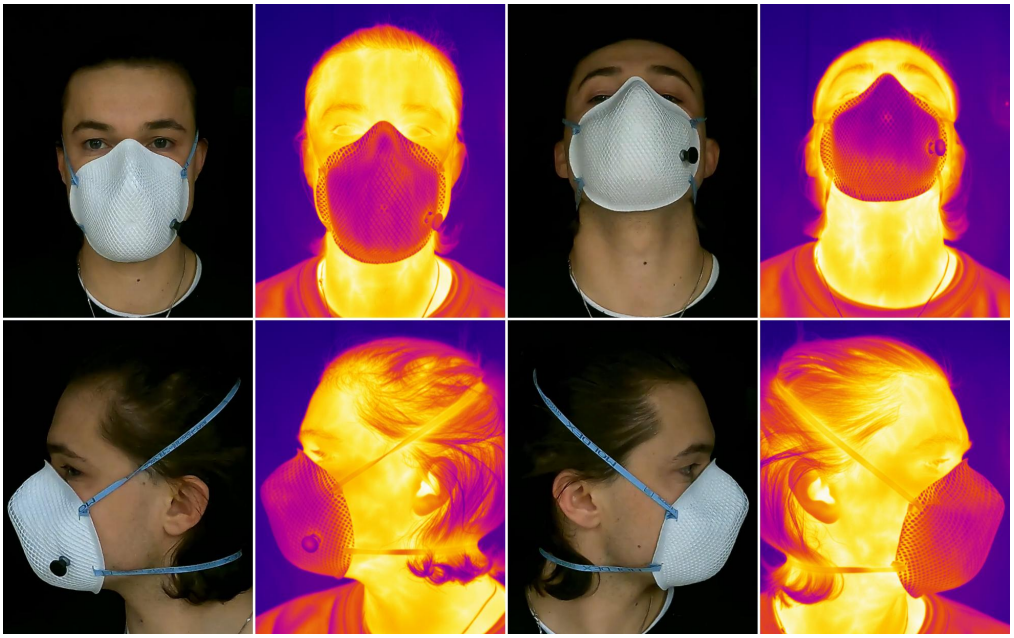

FIGURE 2.4 – Exemples de données SafeRespirator [24].

2.2.5 Banc d'essai dataset [23]

Marchais et al. ont mis au point un banc d'essai reproduisant fidèlement la respiration humaine à l'aide du simulateur ASL 5000® (15 cycles/min, volume courant = 0,66 L) et de deux dispositifs de test (un modèle plat et un masque fixe statique) équipés de fuites calibrées. L'impact thermique de chaque fuite a

3. https://saferespirator.uqar.ca

été capturé avec une caméra infrarouge FLIR X8501sc (FLIR Systems) sous forme de vidéos de 30 s enregistrées à 30 Hz selon quatre angles (face, droite, gauche, dessous), la figure 2.5. Les mesures de l'étanchéité ont été effectuées en parallèle avec un PortaCount® 8038 lors de tests quantitatifs d'étanchéité.

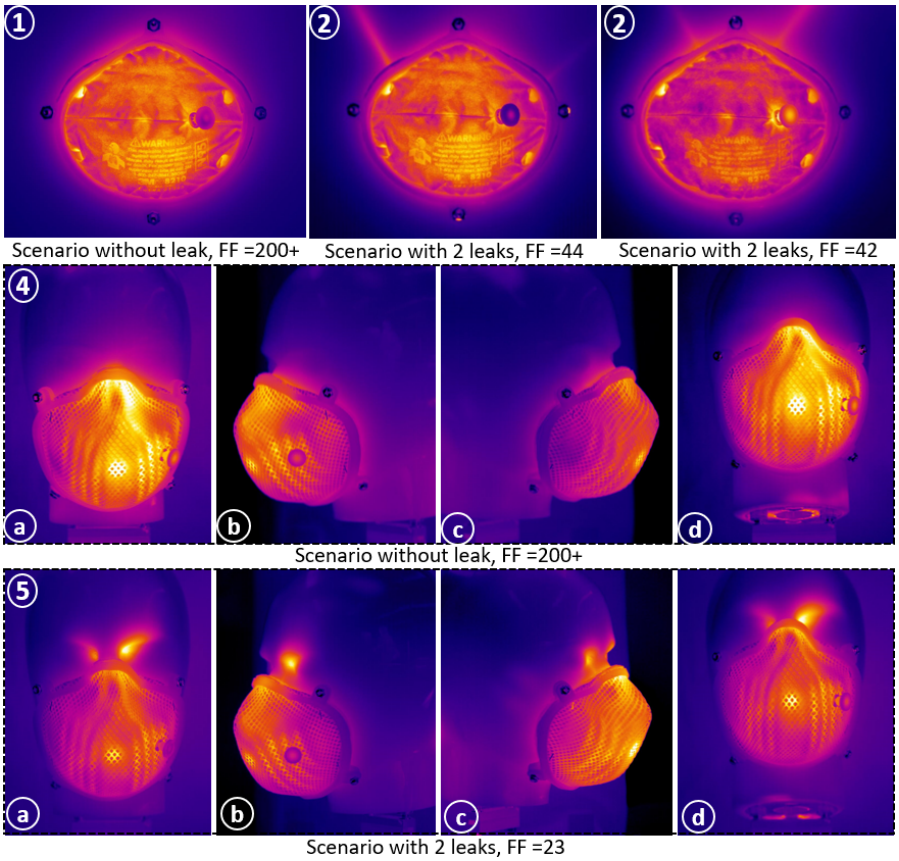

FIGURE 2.5 – Exemples de données banc d'essai [23].

2.2.6 Bases de données utilisées

Dans le cadre de nos recherches, la méthodologie s'articule en deux volets principaux dédiés à l'analyse et des fuites : le premier repose sur un banc d'essai en environnement contrôlé pour caractériser les fuites et en évaluer l'impact autour des masques N95, tandis que le second transpose les protocoles validés à des participants humains. Pour soutenir cette approche, nous avons utilisé deux bases de données (qui ont été développées par notre équipe) :

— base de données controlée (point 2.2.5) [23] : unique en son genre, il reproduit fidèlement la respiration humaine et fournit des séquences thermographiques avec des fuites rigoureusement calibrées.
— base de données « participants » (point 2.2.4) [24] : il associe des séquences haute résolution synchronisées en RGB et infrarouge, surpassant l'état de l'art existant (Tableau 2.1.).

TABLE 2.1 – Comparaison des bases de données utilisées.

Article	Type de caméra	Haute résolution ?	Modes (IR / RVB)	Nb. participants	Sujet humain ?
College of Medicine and Public Health [3]	FLIR One Gen 3 (160×120 px)	Non	IR uniquement	48	Oui
The Catholic University of Korea [19]	FLIR One Pro (1440×1080 px)	Oui	IR uniquement	50	Oui
Hôpital Ruijin database [18]	FLIR One (IR + RGB)	Non	IR + RGB	73	Oui
SafeRespirator dataset [24]	IR : 1280×1024 px (TIFF/ATS), RGB : MP4	Oui	IR + RGB	62	Oui
Banc d'essai dataset [23]	FLIR X8501sc	Oui	IR uniquement	N/A	Non

2.3 Méthodes et approches existantes

Dans cette section, nous passons en revue et analysons les avancées récentes des technologies thermographiques appliquées aux PFF N95, depuis la localisation et la détection automatisée des fuites jusqu'à la conception de nouveaux modèles de PFF. Pour chaque étude, nous décrivons la méthodologie principale, synthétisons les résultats clés et les améliorations démontrées, puis mettons en évidence à la fois les avantages obtenus et les limitations identifiées. En comparant ces travaux côte à côte, nous offrons une vision exhaustive de la manière dont l'imagerie infrarouge contribue à optimiser la sécurité et la performance des PFF N95.

Chapman et al.[3] ont exploré l'utilisation de l'imagerie infrarouge combinée à l'apprentissage automatique pour prédire si un N95 PFF passait ou échouait un test d'étanchéité quantitatif. Ils ont extrait des caractéristiques de matrices de cooccurrence (GLCM) sur des zones d'intérêt thermiques et entraîné 22 modèles (arbres de décision, SVM, k-NN, réseaux de neurones, etc.) à l'aide de MATLAB. Leur objectif était de fournir une alternative objective et automatisée

aux fit check de fuite. Sur une base de données de 96 images, les meilleurs algorithmes (SVM, k-NN, réseau de neurones bicouche, arbres agrégés) ont atteint 87.95 % d'exactitude sur la partie validation.

— Limites : 1/ la méthode n'a été validée que sur un seul modèle plat N95, certains modèles ont montré un surapprentissage marqué (RUSBoosted : 55,5 % d'exactitude sur données non vues, Fine Tree : 77,8 %) et l'absence de tests sur d'autres géométries de PFF limite la généralisation. 2/ la méthode ne permet pas de localiser les fuites

Kim et al.[19] Ils ont filmé en thermique 5 000 séquences de 50 adultes portant cinq types de masques (chirurgical, KF-AD, KF80, KF94, KF99) selon quatre méthodes de port et capturé chaque cycle respiratoire de 4 s à 8,7 Hz et 1440 × 1080 px avec une caméra FLIR One Pro. L'objectif était de développer un contrôle en temps réel de la bonne mise en place des masques. Un réseau 3D CNN a été entraîné pour classer ces méthodes avec une précision binaire atteignant 93,4 %, un AUROC de 0,986 et des F1-scores supérieurs à 0,87, la performance variant légèrement selon le type de PFF N95.

La méthode est limitée à la détection des fuites et ne peut donner l'état du masque dans le visage. Elle n'a pas été utilisée pour détecter et localiser les fuites.

Roberge et al.[32] ont mené une étude pilote auprès de huit sujets familiés avec les tests d'ajustement (cinq hommes, trois femmes) portant trois modèles de PFF N95. Lors d'un protocole abrégé composé de six exercices de dix secondes, une caméra infrarouge FLIR SC 5600-M, positionnée à un mètre du visage, enregistrait en continu des images thermiques à 60 ips afin d'évaluer la capacité de l'imagerie à révéler visuellement les fuites d'exhalation pendant le test. Les auteurs ont repéré un total de 49 fuites au cours de 39 tests, identifiant systématiquement toutes les fuites des tests échoués (13/13) et détectant 26 fuites lors de tests réussis (26/35). Les sites de fuite étaient majoritairement localisés dans

les régions nasale et malaire, et les tests sans fuite présentaient un facteur d'ajustement significativement plus élevé($p = 0{,}01$). Malgré ces résultats prometteurs, l'étude souffre d'un effectif très limité, d'une faible diversité des géométries de masque et d'une analyse entièrement manuelle, sans recours à l'automatisation ni à une localisation précise par traitement d'image. De plus, l'exclusion des exercices générant des mouvements de tête restreint la validité des observations en conditions réelles, et le protocole abrégé ne facilite pas la comparaison avec les standards OSHA.

Kowalski et Mierzejewski [21] ont présenté une méthode entièrement automatisée en deux étapes pour détecter les fuites par masques 3D à partir d'images thermiques. Dans un premier temps, un Faster R-CNN paramétré avec ResNet-50 [14] identifie et extrait automatiquement la région de la tête, puis un second réseau ResNet-50 procède à une classification binaire (authentique vs. fuite) sur ces régions d'intérêt. Entraîné sur une base de données d'environ 7 000 images thermiques (diviser 70 % d'entraînement, 10 % validation, 20 % test), le détecteur de tête atteint un taux de détection de 100 % sans fausse alarme, tandis que le classifieur réalise des APCER et BPCER nuls en validation croisée à dix volets et maintient en scénario d'attaque inconnue un APCER de 0,1 % pour les masques imprimés et 1 % pour les masques latex (avec un BPCER équivalent) . Malgré ces performances, la démarche reste limitée à une simple décision binaire sans aucune localisation précise des fuites, se restreint à deux types de masques 3D dans un environnement contrôlé et n'intègre pas les variations d'émissivité liées à la sueur, aux mouvements ou à des conditions réelles non maîtrisées.

Kowalczyk et al. [20] ont proposé une approche basée sur la segmentation automatique des PFF à partir d'images thermiques afin d'améliorer la qualité des signaux respiratoires extraits. Leur méthode implique initialement la segmentation précise des régions du masque facial en utilisant un modèle basé sur l'architecture YOLOv8 [37] dans sa version nano. Ensuite, les signaux respiratoires ont été extraits à partir des régions segmentées, et leur qualité a été

évaluée via le rapport signal-bruit (SNR). Ces signaux ont été comparés à des références provenant d'une ceinture respiratoire et à des signaux binaires indiquant les phases d'inhalation. Le modèle de segmentation a atteint une précision moyenne (mAP) de 99,2% pour la segmentation et une amélioration notable du SNR par rapport aux approches antérieures basées uniquement sur la détection des fuites avec des PFF. Malgré ces performances élevées, la méthode présente certaines limitations, notamment l'absence d'une analyse fine des fuites respiratoires (localisation précise et quantification), ainsi que la difficulté potentielle à gérer des variations réelles d'émissivité liées à la transpiration, aux mouvements ou à des environnements non contrôlés, étant donné que l'étude s'est déroulée principalement dans des conditions expérimentales contrôlées.

Chapitre 3

Titre :
Segmentation avancée d'un masque facial infrarouge à l'aide d'un modèle U-Net léger personnalisé

Résumé - *La segmentation des PFF N95 par imagerie infrarouge (IR) propose une solution innovante pour détecter précisément les PFF dans des images thermiques. Elle est particulièrement utile pour les secteurs de la santé, de la sécurité et des interactions homme-machine. Cette recherche présente une nouvelle variante légère de l'architecture d'apprentissage profond U-Net, spécialement optimisée pour la segmentation directe des masques médicaux dans l'imagerie IR, répondant à un manque significatif des méthodes traditionnelles principalement axées sur l'imagerie RGB. Le modèle U-Net personnalisé intègre des convolutions séparables en profondeur (SC) pour réduire la complexité computationnelle, garantissant ainsi une précision élevée, un entraînement efficace et une inférence rapide adaptée aux environnements aux ressources limitées.La recherche a impliqué la collecte d'images IR auprès de dix participants portant différents modèles de PFF N95, capturées sous divers angles. L'annotation des images a utilisé l'outil VGG Image Annotator (VIA) pour assurer un étiquetage précis des contours des masques. Les résultats expérimentaux montrent que le modèle proposé atteint des performances remarquables, égalant la précision du modèle U-Net (0,98) tout en améliorant significativement le temps d'entraînement (441 secondes) et en réduisant le nombre de paramètres de plus de 75 %. En outre, le modèle a démontré une précision supérieure en segmentation, en précision, rappel et scores F1 comparativement aux alternatives de pointe.*

Mots clés :
Segmentation des PFF, imagerie infrarouge, apprentissage profond, U-Net, images thermiques, détection de fuites, PFF N95 .

Contributions associées :
Arbane, Mohamed, et al. "Advanced Infrared Face Mask Segmentation Using a Custom Lightweight U-Net Model." 2024 IEEE International Multi-Conference on Smart Systems & Green Process (IMC-SSGP). IEEE, 2024. (Statut : Présenté)
Contributions des auteurs :

Conceptualisation : Mohamed Arbane , Geoffrey Marchais ; méthodologie : Mohamed Arbane ; logiciel :Mohamed Arbane ; validation : Yacine Yaddaden, Jean Brousseau, Clothilde Brochot ; ressources :Xavier Maldague , Clothilde Brochot ; rédaction — préparation de la version originale : Mohamed Arbane, Geoffrey Marchais ; rédaction — révision et édition : Mohamed Arbane, Barthelemy Topilko, Yacine Yaddaden, Jean Brousseau, Ali Bahloul ; supervision : Yacine Yaddaden , Jean Brousseau , Clothilde Brochot, Ali Bahloul, Xavier Maldague.

Advanced Infrared Face Mask Segmentation Using a Custom Lightweight U-Net Model

[1]Mohamed Arbane, [1]Geoffrey Marchais, [1]Barthelemy Topilko, [1]Yacine Yaddaden, [1]Jean Brousseau, [2]Clothilde Brochot, [2]Ali Bahloul & [3]Xavier Maldague

[1]Université du Québec à Rimouski, Rimouski, G5L-3A1 (QC, Canada)
[2]Université Laval, Québec, G1V 0A6 (QC, Canada)
[3]Institut de recherche Robert-Sauvé en santé et en Sécurité du travail, Montréal, H3A 3C2 (QC, Canada)
Email: Mohamed.Arbane@uqar.ca

***Abstract*—Face mask segmentation in the infrared domain represents an innovative technique aimed at improving the accuracy and efficiency of detecting and isolating face masks in thermal images. This approach holds significant relevance in various applications, such as enhancing public health by verifying mask usage in medical environments, improving security through more accurate facial recognition of individuals wearing masks, and advancing human-computer interaction by enabling hands-free device control in mask-mandatory settings, thereby promoting safety and hygiene. In this research, we propose a novel solution that employs deep learning algorithms with infrared imaging to overcome the limitations of conventional mask detection methods. The core of this solution is a custom-designed, optimized variant of the U-Net model. Furthermore, this study forms part of a larger project focused on developing stations for detecting and quantifying leaks in medical masks across various mask types using infrared technologies and artificial intelligence.**

***Index Terms*—Face Mask Segmentation, Infrared Imaging, Deep Learning, U-Net Model, Thermal Images, Leak Detection, Medical Mask Detection.**

I. Introduction

InfraRed-based (IR) face mask segmentation represents a groundbreaking approach to enhance the detection and delineation of face masks in thermal images with increased accuracy and efficiency [1]. This technique plays a pivotal role across various domains, particularly in reinforcing public health protocols by ensuring mask compliance in healthcare settings, enhancing security systems through precise identification of masked individuals, and advancing human-computer interaction by enabling touchless control in areas where masks are required. Consequently, it significantly elevates standards of safety and hygiene.

In thermal IR facial analysis, Convolutional Neural Networks (CNNs) [2], [3] have been effectively utilized for multiclass segmentation tasks. This technique is based on image-to-image translation methodologies, where the primary objective is to categorize each pixel within an image into distinct class labels [4]. Such an approach leverages the robust feature extraction capabilities of CNNs, enabling the precise identification and classification of various elements within thermal images. By applying these advanced neural networks, thermal imagery is effectively translated into segmented maps, with each segment corresponding to a different class based on the pixel characteristics. This method not only enhances the accuracy of facial analysis in thermal images but also expands the range of applications, from improved security measures to enhanced monitoring in healthcare settings.

Building on the foundation established by CNNs, the U-Net model [5] emerges as a specialized architecture explicitly designed for semantic segmentation [6]. U-Net's structure is particularly adept at handling the complexities of segmenting images into meaningful parts, making it ideal for image analysis tasks that require detailed pixel-level classification. Its architecture, characterized by a symmetric U-shaped design, enables efficient capture of contextual information and precise localization by combining low-level feature maps with high-level ones. While the U-Net model is powerful for semantic segmentation, it poses challenges in terms of training time and computational resources. Its complexity leads to prolonged training periods and significant storage requirements, which can hinder swift deployment and scalability in resource-constrained healthcare environments [7].

This paper introduces a semantic segmentation technique for identifying face masks in IR imagery, utilizing an enhanced version of the U-Net model that is designed to lower computational demands, improve efficiency, and reduce model complexity. The research specifically addresses the challenge of segmenting medical masks directly through IR imaging—a notable gap in the current research landscape, where most studies focus on utilizing artificial intelligence based detection systems for mask identification in RGB imagery. This shift to IR and emphasis on segmentation presents a novel approach, diverging from the prevalent RGB-based methodologies. The goal is to optimize the U-Net structure to enhance its performance in real-time environments, particularly within the healthcare sector, where rapid and accurate detection of face masks is crucial. The proposed modifications significantly reduce the time required for training and inference, as well as the storage space needed, making the model more suitable for environments with limited computational resources. This strategy ensures high accuracy in segmentation while facilitating easier implementation and effectiveness for widespread application, especially in critical sectors that demand swift and efficient operation.

979-8-3503-7838-2/24/$31.00

The rest of the paper is organized as follows: Section II presents the related works, reviewing existing literature on face mask detection and semantic segmentation. Section III provides a data description, outlining the dataset used, including details on the IR images and mask labeling criteria. In Section IV, we discuss the proposed approach, highlighting enhancements to the U-Net model for IR imagery and addressing computational efficiency. Section V presents the results and discussion, evaluating the model's performance with quantitative metrics and qualitative examples. Finally, Section VI concludes the paper with a summary of key findings and suggestions for future research.

II. Related Works

This section provides an overview of the most commonly used methods for mask and semantic segmentation, discussing their limitations and the challenges associated with existing approaches.

Müller et al. [8] proposed a precise technique for analyzing faces using thermal IR imaging combined with CNNs for semantic segmentation, allowing for meticulous inspection of specific facial zones. They achieved Intersection over Union (IoU) [9] results exceeding 0.8, reflecting a high rate of accurate detection. However, the effectiveness of the technique depends on creating a comprehensive, manually curated database and requires additional validation across varied practical environments to improve its utility and reliability. Furthermore, their approach employs a conditional Generative Adversarial Network (cGAN) framework, focusing on medical applications such as fever detection during the COVID-19 pandemic, demonstrating precision in segmenting facial regions, with a mean Intersection over Union (mIoU) of 0.95.

In contrast, Gyaourova et al. [10] introduced a method that uses an elliptical mask over the facial image. However, this technique is limited to effectiveness only when faces are directly facing the camera, centered, and captured from a consistent distance to ensure uniform sizing.

Similarly, Hou et al. [11] developed a Semantic Segmentation Generative Adversarial Network (SSGAN) that integrates IR and visible images, preserving the integrity of thermal and visual details. Their research utilized the TNO and INO datasets and underwent comprehensive qualitative and quantitative assessments, revealing enhanced capabilities to maintain informational content and improve image contrast compared to existing techniques.

Furthermore, Badrinarayanan et al. [12] introduced a deep learning architecture called SegNet for semantic segmentation, which shares a similar encoder/decoder structure with U-Net. To address the issue of losing spatial information during multiple pooling stages, SegNet employs a max pooling technique that selects the maximum pixel value while retaining its position on the feature map. During unpooling, it restores the max value to its original location based on recorded coordinates, applying zero padding to the remaining positions.

Valenzuela et al. [13] presented a novel DenseNet-10 model for effectively segmenting Near-IR (NIR) eye images, showcasing high accuracy with a minimalistic design. This model is notable for its simplicity and low parameter count, leveraging only ten layers and $202,084$ parameters, and it outperformed a Facebook challenge, underscoring the efficiency of lightweight models in precise eye segmentation tasks.

Lastly, Zhang et al. [14] introduced a Multi-step Iterative Segmentation Algorithm (MISA) for enhancing facial mask segmentation. This approach employs an improved Mask R-CNN for coarse segmentation and an R-Pairwise Differential Siamese Network (R-PDSN) for fine-tuning edge blocks, achieving a mean pixel accuracy of 0.94 on mask segmentation with an mIoU of 0.91.

III. Data description

The data collection for our study was meticulously conducted with the participation of 10 individuals. Before the experiment began, each participant signed a consent form allowing us to use their facial images for research purposes. We utilized four different models of **N95** masks for each participant: 2200, 8210, 8210V, and 9105.

To ensure a comprehensive analysis, we recorded images from four distinct facial regions: left, right, upward, and downward, capturing five images for each area. This resulted in a total of 80 images per participant.

Fig. 1 below illustrates a participant wearing the N95 2200 mask, highlighting the four areas selected for image capture. This rigorous process enabled a detailed examination of the masks' effectiveness from various angles.

Images were captured using a **FLIR X8501sc** IR camera, chosen for its precision in capturing detailed thermal images. This advanced equipment was instrumental in providing high-quality data, essential for the success of our research.

Fig. 1. Illustration of a participant with four distinct facial areas.

Given the supervised nature of our problem, the labeling of images was meticulously performed using the VGG Image Annotator (VIA), a web-based tool designed for image annotation. This process involved delineating the contours of the masks in each image to accurately extract the necessary points. These points were then saved as a JSON file and applied to the images. Through this method, we generated images where the masked areas are highlighted in white, while the unmasked portions are rendered in black pixels. This approach facilitated a precise analysis of mask coverage on the participants' faces. Fig. 2 illustrates several images alongside their corresponding labels, clearly representing the annotation process and the resulting mask contours.

IV. Proposed approach & Complexity analysis

The proposed model in this study introduces a novel variant of the U-Net architecture aimed at addressing some of the

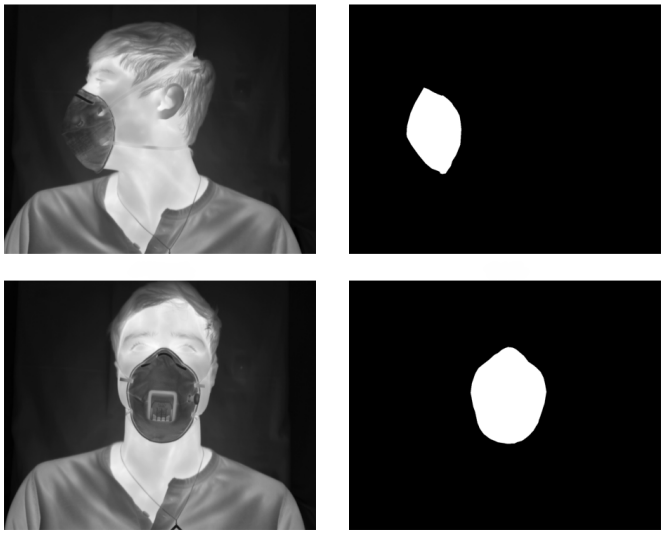

Fig. 2. Overview of a sample: the original (*left*) and the labeled image (*right*).

limitations found in the conventional U-Net framework and its advanced versions, thereby improving their effectiveness. This innovative approach incorporates depth-wise Separable Convolutions (SC) across various layers [15]. Depth-wise SC reduces the computational burden of standard convolution by applying a single convolutional filter per input channel, rather than multiple filters simultaneously. Unlike traditional convolution, where the image undergoes multiple transformations through a kernel—potentially increasing computational time and complexity—depth-wise SC first applies depth-wise convolution to process the image and then expands the resulting feature map across the necessary channels. This technique conserves computational resources by reducing the frequency of image transformations, thus decreasing the model's parameter count while improving its ability to detect relevant features. The SC function is described as a mathematical operation with the following definition (see Eq. 1):

$$y\left[a,b\right] = g\left[a,b\right] \times x\left[a,b\right] = \sum_{c=0}^{\infty}\sum_{e=0}^{\infty} h\left[e,c\right] \times x\left[a-e,b-c\right] \tag{1}$$

The concept involves breaking down an $a \times b$ filter into two smaller filters: one sized $a \times 1$ and the other $1 \times b$. Applying these smaller filters to an image does not alter the final result, as the original data is preserved. Nonetheless, this approach decreases the computational work needed since these smaller filters necessitate fewer operations. Termed spatial SC, this method enhances the efficiency of image processing while ensuring no significant information is lost. The function $h[a,b]$ is decomposed into two components, g_1 with dimensions $a \times 1$ and g_2 measured as $1 \times b$, as demonstrated in Eq. 2.

$$g\left[a,b\right] = g_1\left[a\right] \times g_2\left[b\right] \tag{2}$$

Thus, in the given Eq. 3 and Eq. 4, g is substituted with g_1 and g_2 respectively.

$$y\left[a,b\right] = g\left[a,b\right] \times x\left[a,b\right] = \sum_{c=0}^{\infty}\sum_{e=0}^{\infty} g_1\left[e\right] g_2\left[c\right] \times x\left[a-e,b-a\right] \tag{3}$$

$$y\left[a,b\right] = g\left[a,b\right] \times x\left[a,b\right] = \sum_{c=0}^{\infty} g_2\left[c\right] \left(\sum_{e=0}^{\infty} g_1\left[e\right] \times x\left[a-e,b-a\right]\right) \tag{4}$$

This suggests that an initial convolution is performed on the image using g_1, followed by a second convolution applied to the result of the first convolution using g_2, as illustrated below (see Eq. 5):

$$y\left[a,b\right] = \left(g_1\left[a\right] g_2\left[b\right]\right) \times x\left[a,b\right] = g_2\left[b\right]\left(g_1\left[a\right] \times x\left[a,b\right]\right) \tag{5}$$

The computational complexity for both standard and SCs is determined by the number of operations each requires. Standard convolution exhibits a complexity of $O(i^2 j^2)$, where i represents the input image's dimension and j the filter's size. This is due to the need to perform j^2 operations for each element across the i^2 elements of the image, resulting in a total of $i^2 \cdot j^2$ operations. Conversely, SC has a lower complexity of $O(2i \cdot j)$. This reduction is achieved by first applying a horizontal filter across each of the image's i rows, requiring j operations per row, followed by a vertical filter across the i columns, also requiring j operations per column. The total number of operations is $2i \cdot j$, simplifying to $O(i \cdot j)$. Therefore, SC is computationally more efficient than standard convolution, significantly reducing the computational load.

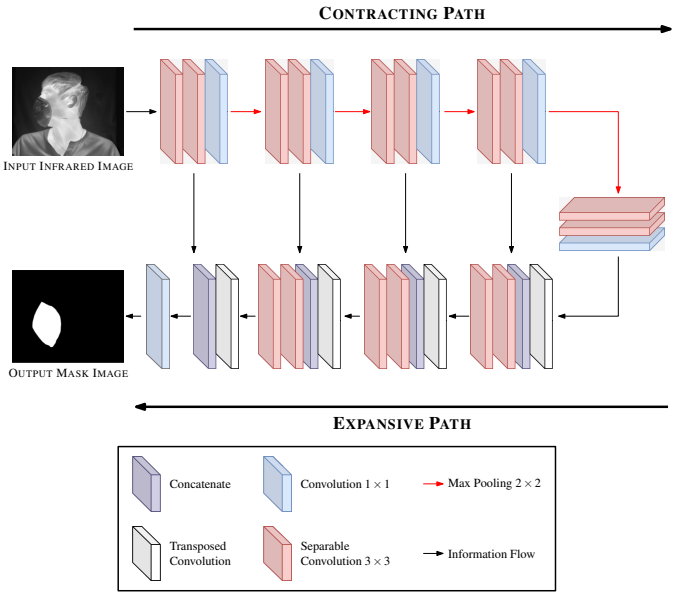

Fig. 3. Overview of the proposed Model.

The architecture presented in Fig. 3 outlines the proposed model, which is specifically designed for directly processing raw images. This architecture stands out due to its unique design, beginning with an input layer that accepts raw images. The model then follows a contracting path, which is composed of four distinct blocks. Each block features two depth-wise SCs, followed by a standard convolution. Max pooling is applied after each block to progressively reduce the image size while retaining important features. The Xavier initialization method [16] is used to initialize the weights, providing an optimal starting point for the model's learning process. The number of filters starts at 16 in the first block and increases to 32, 64, and 128 in subsequent blocks, allowing for a gradual extraction of more complex features as the model deepens.

The expansive path mirrors the complexity of the contracting path and is also comprised of four blocks. In the first two blocks, transpose convolutions and concatenation are used to upsample and merge feature maps, followed by two depth-wise SCs. This technique allows the model to reconstruct the image from its compressed feature representation. The final stage of the expansive path applies a 1×1 convolution combined with a sigmoid activation function [17], optimizing the model for precise pixel-wise binary classification, enhancing its ability to effectively segment each pixel.

V. Results & Discussion

In this section, the performance of the proposed model is evaluated and compared to top-performing *state-of-the-art* models. The datasets used for this analysis are described in Section III. The experiments were conducted on a computer with an i5-10300H CPU @ 2.50GHz and 32GB of RAM.

Training was performed for all networks until convergence, using ten epochs with batch sizes of 10. The Adam optimization algorithm [18] was employed, with a learning rate of 0.001. The dataset was split into three segments: 70% for training, and 15% each for testing and validation.

A. Evaluation metrics

The evaluation metrics for the model include computation time, accuracy, loss, IoU [9], recall, F1-score and precision on the test dataset. Computation time measures the training efficiency, while accuracy indicates the proportion of correctly classified pixels in the test dataset. Loss assesses the prediction errors, and IoU evaluates the segmentation accuracy by comparing the overlap between predicted and actual regions. Recall measures the model's ability to identify relevant pixels, precision evaluates the correctness of the identified positive pixels, and the F1-score balances precision and recall. Together, these metrics provide a comprehensive framework for evaluating the segmentation model's performance in terms of both accuracy and efficiency.

B. Results analysis

Table I and Fig. 4 present a comparative analysis of the proposed model against the *state-of-the-art* U-Net and U-Net++ models, highlighting its superior performance across several key metrics. While all three models exhibit high accuracy, the proposed model and U-Net both achieve an impressive accuracy of 0.98, demonstrating their ability to effectively classify pixels in the test set. In contrast, U-Net++ lags slightly behind with an accuracy of 0.94.

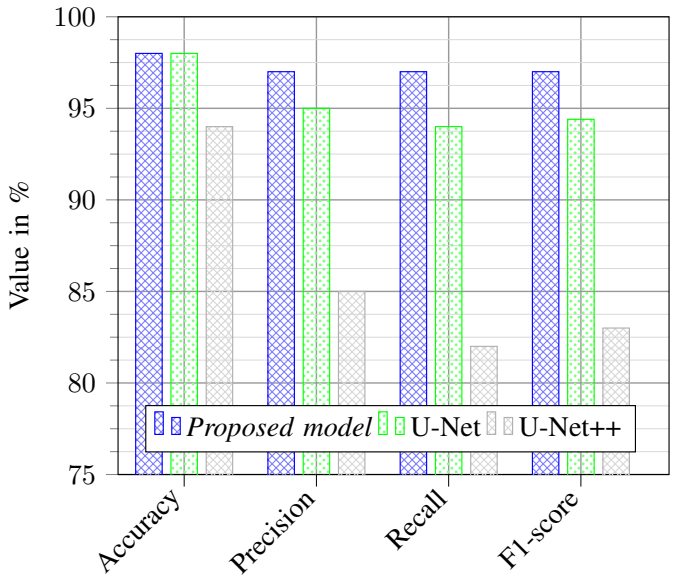

Fig. 4. Comparison of accuracy, precision, recall, and F1-score across models.

Despite the close accuracy results, the proposed model demonstrates significant advantages over U-Net, particularly in terms of computation time, parameter efficiency, and advanced recall and F1-scores. It completes training in just 441 seconds—substantially faster than U-Net's 660 seconds and U-Net++'s 500 seconds—underscoring its efficient learning capabilities. Additionally, the proposed model requires only $472,908$ parameters, a reduction of over 75% compared to the $1,941,105$ parameters in both U-Net and U-Net++, all while maintaining high performance. This reduction highlights the proposed model's optimized design, making it ideal for practical, resource-constrained environments.

The proposed model also surpasses its competitors in segmentation accuracy, achieving a mIoU of 0.96, outperforming U-Net's 0.95 and significantly exceeding U-Net++'s 0.78. This superior mIoU illustrates the model's advanced capability in precise image segmentation. In terms of precision, recall, and F1-scores, the proposed model consistently scores 0.97 across all three metrics, surpassing both U-Net and U-Net++. This reflects the proposed model's balanced performance, excelling in both precision and recall.

In comparison to RGB-based segmentation models like Mask R-CNN + ResNet and its Edge Segmentation (ES) variant, the proposed model further distinguishes itself with markedly higher accuracy and mIoU scores. These results emphasize its strength not only over IR-based models like U-Net and U-Net++ but also over popular RGB-based approaches, showcasing its versatility across different imaging modalities.

TABLE I
COMPARISON BETWEEN THE PROPOSED MODEL AND *state-of-the-art* U-NET MODELS.

Methods	Image	Accuracy	Precision	Recall	F1-SCORE	LOSS	TRAINING TIME	MIOU	PARAMETERS
R-CNN + ResNet [14]	RGB	0.90	–	–	–	–	–	0.89	–
R-CNN + ResNet + ES [14]	RGB	0.94	–	–	–	–	–	0.91	–
U-Net + GAN [8]	IR	–	–	–	–	–	–	0.95	–
U-Net	IR	0.98	0.95	0.94	0.94	0.02	660 s	0.95	1,941,105
U-Net++	IR	0.94	0.85	0.82	0.83	0.14	500 s	0.78	1,941,105
Proposed model	IR	0.98	0.97	0.97	0.97	0.03	441 s	0.96	472,908

Overall, the analysis confirms that the proposed model not only matches U-Net in accuracy but also excels in speed, efficiency, and segmentation quality. This positions it as a strong candidate for applications demanding both high precision and operational efficiency. Although U-Net++ shows lower performance metrics in this study, its inclusion underscores the importance of dataset size and model complexity in optimization; it may perform better with larger datasets that can fully exploit its sophisticated architecture. Finally, Fig. 5 illustrates the proposed model's consistent improvement across epochs, highlighting its ability to progressively refine feature extraction and overcome variance, solidifying its robustness and reliability in diverse operational scenarios.

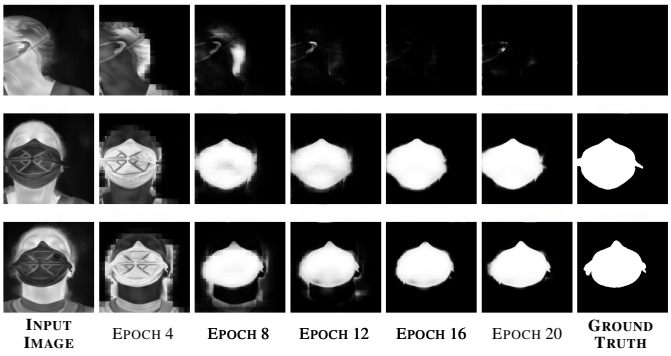

Fig. 5. The proposed model training on different EPOCHS.

Fig. 6 showcases the results of mask segmentation on an IR image of a participant, demonstrating the model's proficiency in accurately segmenting the mask. This performance highlights the model's effectiveness in identifying and delineating the mask region with precision.

VI. CONCLUDING REMARKS

The proposed variant of the U-Net model is explicitly optimized for direct application to IR images. By meticulously conducting real-world image collection, dataset compilation, and labeling processes, we have engineered a model that minimizes the number of parameters and computational time required while significantly surpassing the performance of the traditional U-Net architecture. A key factor in achieving this efficiency was the transition from conventional CNNs to separable CNNs, which were essential in reducing the model's parameter size without compromising information fidelity. This advancement demonstrates our model's potential

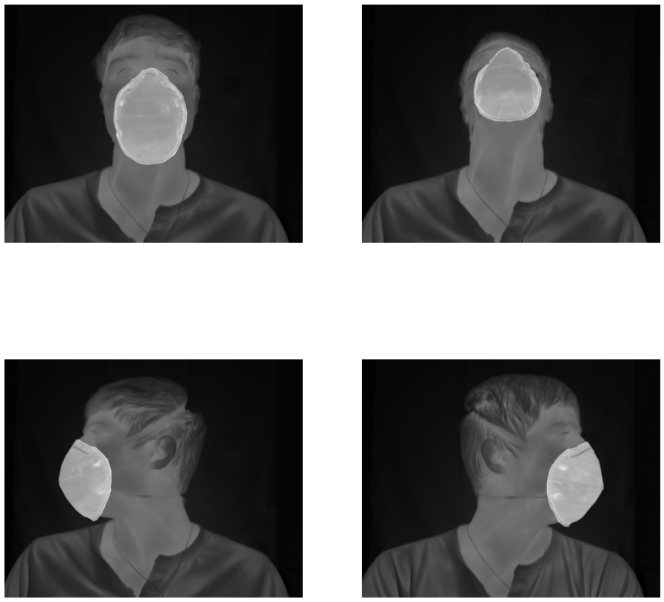

Fig. 6. Overview of the proposed model segmentation on IR images.

to redefine industry standards, offering a robust solution that balances accuracy with computational efficiency.

In our future work, we plan to enhance our model to detect and quantify leaks in N95 masks by analyzing temperature variations. This enhancement aims to provide deeper insights into mask efficacy and safety by identifying thermal anomalies that indicate improper fitting. Through this innovation, we seek to contribute to improved health protocols by ensuring that masks are worn correctly, thereby enhancing protection in critical environments.

VII. ACKNOWLEDGEMENT

This work is supported by the "Respiratory Protective Devices—Development of an Easy-to-Use Method to Detect Leaks and Assess Face Seal Tightness Using Infrared Imaging" project, which is funded by **IRSST** (Institut de recherche Robert-Sauvé en santé et en sécurité du travail) and **Mitacs Acceleration** under grant agreement No. IT37899.

REFERENCES

[1] E. Koroteeva and A. Shagiyanova, "Infrared-based visualization of exhalation flows while wearing protective face masks," *Physics of Fluids*, vol. 34, no. 1, 2022.

[2] K. O'Shea, "An introduction to convolutional neural networks," *arXiv preprint arXiv:1511.08458*, 2015.

[3] Y. Yaddaden, M. Adda, A. Bouzouane, S. Gaboury, and B. Bouchard, "User action and facial expression recognition for error detection system in an ambient assisted environment," *Expert Systems with Applications*, vol. 112, pp. 173–189, 2018.

[4] Z. Li, F. Liu, W. Yang, S. Peng, and J. Zhou, "A survey of convolutional neural networks: analysis, applications, and prospects," *IEEE transactions on neural networks and learning systems*, vol. 33, no. 12, pp. 6999–7019, 2021.

[5] O. Ronneberger, P. Fischer, and T. Brox, "U-net: Convolutional networks for biomedical image segmentation," in *Medical image computing and computer-assisted intervention–MICCAI 2015: 18th international conference, Munich, Germany, October 5-9, 2015, proceedings, part III 18*. Springer, 2015, pp. 234–241.

[6] Y. Guo, Y. Liu, T. Georgiou, and M. S. Lew, "A review of semantic segmentation using deep neural networks," *International journal of multimedia information retrieval*, vol. 7, pp. 87–93, 2018.

[7] M. Arbane, M. E. Khanouche, G. Khodabandelou, C. Abdelghani, and Y. Amirat, "Drsu-net: Depth-residual separable u-net model for semantic segmentation," in *2023 International Joint Conference on Neural Networks (IJCNN)*. IEEE, 2023, pp. 1–6.

[8] D. Müller, A. Ehlen, and B. Valeske, "Convolutional neural networks for semantic segmentation as a tool for multiclass face analysis in thermal infrared," *Journal of nondestructive evaluation*, vol. 40, no. 1, p. 9, 2021.

[9] H. Rezatofighi, N. Tsoi, J. Gwak, A. Sadeghian, I. Reid, and S. Savarese, "Generalized intersection over union: A metric and a loss for bounding box regression," in *Proceedings of the IEEE/CVF conference on computer vision and pattern recognition*, 2019, pp. 658–666.

[10] A. Gyaourova, G. Bebis, and I. Pavlidis, "Fusion of infrared and visible images for face recognition," in *Computer Vision-ECCV 2004: 8th European Conference on Computer Vision, Prague, Czech Republic, May 11-14, 2004. Proceedings, Part IV 8*. Springer, 2004, pp. 456–468.

[11] J. Hou, D. Zhang, W. Wu, J. Ma, and H. Zhou, "A generative adversarial network for infrared and visible image fusion based on semantic segmentation," *Entropy*, vol. 23, no. 3, p. 376, 2021.

[12] V. Badrinarayanan, A. Kendall, and R. Cipolla, "Segnet: A deep convolutional encoder-decoder architecture for image segmentation," *IEEE transactions on pattern analysis and machine intelligence*, vol. 39, no. 12, pp. 2481–2495, 2017.

[13] A. Valenzuela, C. Arellano, and J. E. Tapia, "Towards an efficient segmentation algorithm for near-infrared eyes images," *IEEE Access*, vol. 8, pp. 171 598–171 607, 2020.

[14] M. Zhang, K. Xie, Y.-H. Zhang, C. Wen, and J.-B. He, "Fine segmentation on faces with masks based on a multistep iterative segmentation algorithm," *IEEE Access*, vol. 10, pp. 75 742–75 753, 2022.

[15] F. Chollet, "Xception: Deep learning with depthwise separable convolutions," in *Proceedings of the IEEE conference on computer vision and pattern recognition*, 2017, pp. 1251–1258.

[16] S. K. Kumar, "On weight initialization in deep neural networks," *arXiv preprint arXiv:1704.08863*, 2017.

[17] J. Pennington, S. Schoenholz, and S. Ganguli, "Resurrecting the sigmoid in deep learning through dynamical isometry: theory and practice," *Advances in neural information processing systems*, vol. 30, 2017.

[18] D. P. Kingma, "Adam: A method for stochastic optimization," *arXiv preprint arXiv:1412.6980*, 2014.

Chapitre 4

Titre :
Localisation en temps réel des fuites dans les PFF N95 à l'aide de l'imagerie infrarouge et de l'apprentissage profond avec une corrélation optimale du signal ROI.

Résumé - *Un ajustement étanche des PFF N95 est essentiel pour prévenir les contaminants aéroportés, notamment dans des environnements médicaux et industriels à haut risque. Cependant, même des fuites mineures peuvent considérablement compromettre leur efficacité protectrice. Cet article présente une méthodologie intégrée innovante combinant l'imagerie infrarouge (IR) et des techniques avancées d'apprentissage profond pour la localisation non invasive et en temps réel des fuites. Un modèle personnalisé de type U-Net est développé pour extraire précisément la région du masque à partir d'images thermiques, tandis que le modèle Segment Anything 2 (SAM2) permet de suivre dynamiquement les variations du contour du masque sous des conditions variables telles que les mouvements naturels de la tête et les variations thermiques dues à la respiration. Les signaux thermiques capturés le long du périmètre du masque sont ensuite transformés dans le domaine fréquentiel via une transformée de Fourier rapide (FFT) et corrélés avec un signal respiratoire de référence extrait d'une région centrale optimale (ROI) pour identifier précisément les points de fuite. La méthode proposée inclut une procédure systématique pour déterminer la région centrale la plus représentative du cycle respiratoire, optimisant ainsi la robustesse de la détection par corrélation. La validation expérimentale réalisée par la méthode Pixel-wise Breathing Cycle Optical Flow Differential Imaging (PBC-OFDI) confirme l'efficacité de cette approche, permettant une visualisation claire et précise des zones de fuite. Les résultats expérimentaux démontrent une supériorité claire de cette approche par rapport aux méthodes traditionnelles de vérification d'étanchéité qui nécessitent un contact physique et sont sujettes à des risques de contamination croisée.*

Mots clés :
Imagerie infrarouge, apprentissage profond, localisation des fuites, analyse fréquentielle, U-Net, SAM2, optimisation ROI, PFF N95
Contributions associées :
Arbane, Mohamed, et al. "Real-Time Leak Localization in N95 Respirators Using Infrared Imaging and Deep Learning with Optimal ROI Signal Correlation."

2025 IEEE EEITE. (Statut : Présenté)
Contributions des auteurs :
Conceptualisation : Mohamed Arbane , Geoffrey Marchais ; méthodologie : Mohamed Arbane ; logiciel :Mohamed Arbane ; validation : Yacine Yaddaden, Jean Brousseau, Clothilde Brochot ; ressources :Xavier Maldague , Clothilde Brochot ; rédaction — préparation de la version originale : Mohamed Arbane ; rédaction — révision et édition : Mohamed Arbane, Yacine Yaddaden, Jean Brousseau, Ali Bahloul, Clothilde Brochot , Xavier Maldague ; supervision : Yacine Yaddaden , Jean Brousseau , Clothilde Brochot, Ali Bahloul, Xavier Maldague.

Real-Time Leak Localization in N95 Respirators Using Infrared Imaging and Deep Learning with Optimal ROI Signal Correlation

[1]Mohamed Arbane, [1]Yacine Yaddaden, [1]Jean Brousseau,
[2]Clothilde Brochot, [3]Geoffrey Marchais,[2]Ali Bahloul & [4]Xavier Maldague

[1]Université du Québec à Rimouski, Rimouski, G5L-3A1 (QC, Canada)
[2]Institut de Recherche Robert-Sauvé en Santé et en Sécurité du Travail, Montréal, H3A-3C2 (QC, Canada)
[3]École de Technologie Supérieure, Montréal, H3C-1K3 (QC, Canada)
[4]Université Laval, Québec, G1V-0A6 (QC, Canada)
Email: Mohamed.Arbane@uqar.ca

***Abstract*—A secure seal in N95 respirators is critical for preventing airborne contaminants, yet minor leaks significantly compromise protective efficiency. This paper presents an integrated framework leveraging infrared imaging and deep learning for real-time, non-contact leak localization. A custom U-Net model extracts the mask region from thermal images, while the Segment Anything Model 2 (SAM2) dynamically tracks contour variations under changing conditions. Thermal signals along the mask boundary are transformed into the frequency domain and correlated with a reference breathing signal to identify leak locations. The proposed method systematically evaluates optimal central region selection to enhance correlation-based leak detection. Experimental validation using pixel-wise Breathing Cycle Optical Flow Tracking demonstrates the effectiveness of this approach in accurately detecting and localizing leaks in real-world conditions, offering a robust alternative to conventional contact-based fit-testing methods.**

***Index Terms*—Infrared Imaging, Deep Learning, Leak Localization, Frequency-Domain Analysis, U-Net, SAM2, ROI Optimization, N95 Respirators.**

I. Introduction

N95 respirators are essential for protecting healthcare professionals and the general public against airborne pathogens and workers against harmful exposure to airborne contaminants. These masks are designed to filter at least 95% of particulate matter, making them a crucial part of Personal Protective Equipment (PPE) in hospitals, clinics, and other high-risk environments [1]. The proper functioning of these masks is vital for individual safety and for preventing the spread of infections during outbreaks of respiratory diseases [2], [3]. Maintaining a secure seal is paramount to ensuring their effectiveness [4].

The performance of an N95 mask largely depends on its ability to form a tight interface with the wearer's face. Even small leaks along the edges of the mask can have serious consequences, allowing unfiltered air to enter or exit the respiratory pathway. Such breaches compromise the intended protective barrier, increasing the risk of inhaling harmful airborne particles. In settings with high exposure to infectious agents, even a minor defect in the seal can significantly heighten the risk of infection, endangering both the individual and those nearby [5], [6].

Traditional methods for assessing the fit of N95 masks have been used for a long time to evaluate the fit of the mask, such as the PortaCount® quantitative fit test, have been used for a long time to measure the concentration of particles inside and outside the mask. These methods provide a numerical index that quantifies the degree of leakage or a qualitative evaluation by the wearer. However, conventional fit-testing procedures typically involve physical contact between the testing apparatus and the mask, requiring manual intervention for proper positioning, professional assistance, and are inherently time-consuming [7]. This contact-based approach raises concerns about cross-contamination and the risk of infection transmission, especially during times when minimizing physical interactions is critical. As a result, there is a growing need for non-contact, remote methodologies to assess mask integrity without compromising safety.

Infrared imaging presents a compelling alternative due to its ability to detect thermal signatures associated with exhaled breath. When an N95 mask does not form an ideal seal, warm air escapes through gaps, creating distinct thermal anomalies that can be detected with InfraRed (IR) cameras. By integrating infrared imaging with advanced signal processing techniques, it becomes feasible to monitor these temperature variations in real time [8], [9].

This paper presents a novel approach that combines IR domain analysis with Artificial Intelligence (AI)-based techniques for real-time leak localization in N95 respirators. The method leverages correlation analysis between selected regions of interest (ROIs) along the mask's perimeter and a reference region corresponding to the wearer's breathing signal. Real-time segmentation continuously tracks the N95 mask on the user's face, enabling dynamic boundary extraction and signal analysis. An initial step systematically determines the optimal reference region that most accurately captures the breathing

979-8-3315-4419-5/25/$31.00 ©2025 IEEE

cycle, ensuring robust correlation-based detection. In parallel, the system evaluates the correlation of perimeter ROIs to identify and confirm leak locations. This integrated framework offers a non-contact, real-time alternative to conventional fit-testing methods, providing a reliable and scalable solution for continuous monitoring of respirator integrity in dynamic conditions.

The remainder of the paper is organized as follows: Section II reviews related work on infrared imaging and deep learning techniques for mask leak detection. Section III describes the dataset and experimental setup used for acquiring thermal images and evaluating respirator integrity. Section IV details the proposed framework, including segmentation, ROI selection, and correlation analysis for real-time leak localization. Section V presents and discusses the experimental results. Finally, Section VI concludes the paper and outlines directions for future work.

II. Related Work

Traditional methods for evaluating the fit and integrity of N95 respirators rely on both qualitative and quantitative testing protocols. Qualitative techniques, such as saccharin and Bitrex tests, provide subjective assessments of mask fit based on the wearer's ability to detect sweet or bitter aerosolized substances. In contrast, quantitative methods, such as those using the PortaCount® device, are widely adopted for measuring particle concentration differentials inside and outside the mask, offering more objective metrics [10], [11]. While these approaches yield reliable results under controlled conditions, their contact-dependent nature introduces concerns regarding repeated exposure, potential cross-contamination, and limited applicability for continuous, real-time monitoring.

As a result, non-contact methodologies have gained increased attention in recent years. IR imaging has emerged as a promising alternative due to its capability to capture thermal signatures of exhaled breath. Prior studies have demonstrated that IR cameras can detect subtle temperature variations on the surface of the mask that correspond to potential leakage sites [12], [13]. By analyzing the thermal contrast between exhaled air and the ambient environment, IR imaging enables visualization and quantification of leaks without physical contact, reducing the risk of infection during the evaluation process.

In parallel, the integration of AI techniques with IR-based systems has significantly enhanced the automation and accuracy of leak detection. Convolutional Neural Networks (CNNs) [14] have been successfully employed to segment mask regions from thermal images, enabling the isolation of ROIs for detailed analysis [15]. Transfer learning has further improved performance in thermal domains with limited annotated data by adapting *pre-trained* CNNs to domain-specific features. Moreover, hybrid models combining deep feature extraction with classical machine learning classifiers, such as Support Vector Machines (SVMs), have proven effective in distinguishing between leak and no-leak conditions [16].

Beyond binary classification, precise spatial localization of leak regions is critical for comprehensive respirator assessment. Recent methodologies have leveraged frequency-domain analysis to correlate thermal signals from the mask perimeter with a reference breathing signal extracted from a central ROI. Systematic evaluations have been conducted to identify the optimal central region that most reliably reflects the user's respiratory pattern, thereby improving the robustness of correlation-based leak detection [17]. This approach enables accurate, real-time identification of leak sites, offering a valuable tool for continuous monitoring and timely intervention.

III. Data Collection

A human subject dataset was collected to evaluate the proposed leak detection framework under realistic conditions. Participants wore properly fitted N95 respirators while a high-resolution IR camera continuously recorded thermal video. Multiple models of N95 masks were used to capture inter-device variability and ensure broader applicability. The experimental setup was designed to capture the full contour of each mask during natural head movements and routine activities, allowing temperature variations indicative of leaks to be effectively recorded. Fig. 1 shows representative thermal frames from four participants. This dataset, as further described in [8] and [9], serves as a robust foundation for analyzing dynamic mask performance and validating the proposed leak localization approach.

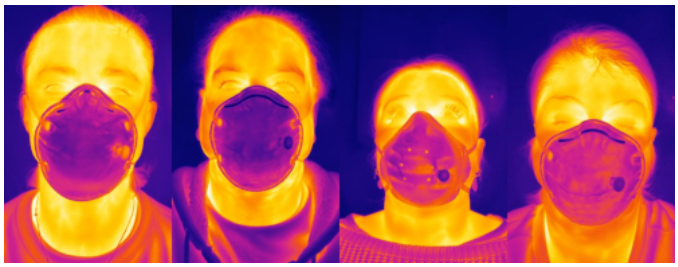

Fig. 1: Sample thermal frames from four participants.

IV. Proposed Framework & Methodology

To support automated leak localization, accurate segmentation of the N95 respirator region within IR thermal images is a critical pre-processing step. Segmentation ensures that only relevant thermal data along the mask boundary are analyzed, minimizing noise from unrelated facial or background regions. To this end, a hybrid workflow combining a modified U-Net architecture with the Segment Anything Model 2 (SAM2) was developed for robust, real-time mask extraction in dynamic settings.

As illustrated in Fig. 2, the workflow begins with thermal video input, followed by frame-wise processing using a lightweight U-Net variant specifically adapted to the thermal domain. This model provides an initial segmentation of the mask area. SAM2 is then employed to refine the mask contours, leveraging its ability to generalize across image conditions and maintain high spatial consistency under head movement and varying thermal patterns. The fusion of these two methods balances accuracy with computational efficiency,

enabling continuous segmentation even during natural activities such as speaking or breathing.

This segmentation pipeline provides the necessary spatial constraints for subsequent ROI selection and signal analysis along the mask perimeter. The improved localization of the mask boundaries directly enhances the precision of the leak detection algorithm, particularly when correlating dynamic thermal fluctuations with the central breathing reference signal.

A. Reducing Motion Impact via Segmentation

Before conducting correlation analysis and selecting the ROI, special emphasis is placed on minimizing the impact of facial movement. In dynamic, real-world settings, even slight shifts in head position or facial expressions can lead to misalignment in mask segmentation, which may distort the thermal signal extraction process. To address this issue, the proposed framework utilizes precise segmentation methods that continuously track both the mask and the underlying face.

This study employs a semantic segmentation variant of U-Net, developed specifically for N95 respirators as described in previous research [18], on the first frame of the thermal video. The *hyperparameters*, training parameters, and weights of the model were established in that earlier work and remain unchanged in this study, ensuring consistent segmentation performance without the need for additional training. The initial segmentation accurately captures the mask's contour and all relevant mask regions. Its output is then used as an input prompt (encoder mask) for the Segment Anything Model 2 (SAM2) [19]. SAM2, a *state-of-the-art* segmentation tool, dynamically refines these segmentation masks across successive frames, as illustrated in Fig. 2. By integrating these segmentation methods, the framework minimizes errors caused by facial movement, ensuring that the extracted breathing reference signal is both stable and representative—an essential requirement for reliable correlation-based leak localization.

B. Selection of Region of Interest

The proposed framework defines two types of regions of interest (ROIs) for leak localization. The first type consists of 100 equal-sized ROIs that are evenly distributed along the contour of the N95 mask, capturing local thermal signals from the entire mask boundary. The second type is the central ROI, extracted from the central area of the mask to represent the breathing signal. This central ROI is crucial to the analysis as it serves as the reference for correlation analysis with each of the 100 peripheral ROIs to determine which regions exhibit a similar breathing pattern—a similarity that indicates a potential leak. Given its pivotal role, choosing and comparing different central ROIs leads to better extraction of the breathing signal, further enhancing the reliability and accuracy of the leak detection process.

Before applying further processing on the extracted signals, a Fast Fourier Transform (FFT) is applied to convert the signals into the frequency domain. This transformation enhances the visualization of the breathing cycle and the associated frequency components, thereby facilitating a more effective correlation analysis.

Various candidate positions within the central mask region were evaluated, as illustrated in Fig. 3, and these candidates yielded slightly different signal characteristics. To mitigate this variability and ensure consistency, a normalization process is applied to scale the signals to a range between -1 and 1. The normalization is performed using the following equation:

$$x_{\text{norm}} = 2\left(\frac{x - x_{\min}}{x_{\max} - x_{\min}}\right) - 1 \tag{1}$$

Where x represents the original signal value, and $x_{\min}$ and $x_{\max}$ are the minimum and maximum values of the signal, respectively. This normalization minimizes noise and aligns the signal patterns across all candidate regions.

To automatically select the optimal central ROI, four specific points are chosen from the 100 peripheral ROIs. Two pairs of these points—namely, ROI 1 with ROI 51 and ROI 25 with ROI 76—are considered inverses. The intersection of the lines connecting these pairs is computed, yielding a central point. A circle with a radius of 20 pixels centered at this intersection defines the region of the central ROI. This procedure ensures that the selected central ROI reliably captures the representative breathing signal for accurate correlation-based leak localization.

C. Correlation Methods

A critical component of the proposed framework is the use of correlation analysis to compare the normalized frequency-domain signals extracted from the central ROI with those from the peripheral ROIs. Several correlation techniques are employed to ensure robustness in leak localization. Also, this component is based on the physical fact that a leak point allows exhaled warm air to escape, producing thermal fluctuations that are temporally synchronized mimics with the breathing cycle. The following correlation methods and their corresponding algorithms are utilized:

a) Pearson Correlation: Pearson correlation is applied to measure the linear relationship between two signals. Given two discrete signals, $X = \{x_1, x_2, \ldots, x_n\}$ and $Y = \{y_1, y_2, \ldots, y_n\}$, the Pearson correlation coefficient is calculated as:

$$\rho_{\text{Pearson}}(X, Y) = \frac{\sum_{i=1}^{n}(x_i - \bar{x})(y_i - \bar{y})}{\sqrt{\sum_{i=1}^{n}(x_i - \bar{x})^2}\sqrt{\sum_{i=1}^{n}(y_i - \bar{y})^2}} \tag{2}$$

where $\bar{x}$ and $\bar{y}$ denote the mean values of X and Y, respectively. This metric provides a value between -1 and 1, with values closer to 1 indicating a strong positive linear relationship.

b) Spearman Correlation: Spearman correlation assesses the monotonic relationship between two signals by converting the raw data into ranks. If $R(x_i)$ and $R(y_i)$ represent the ranks of x_i and y_i, the Spearman coefficient is computed as:

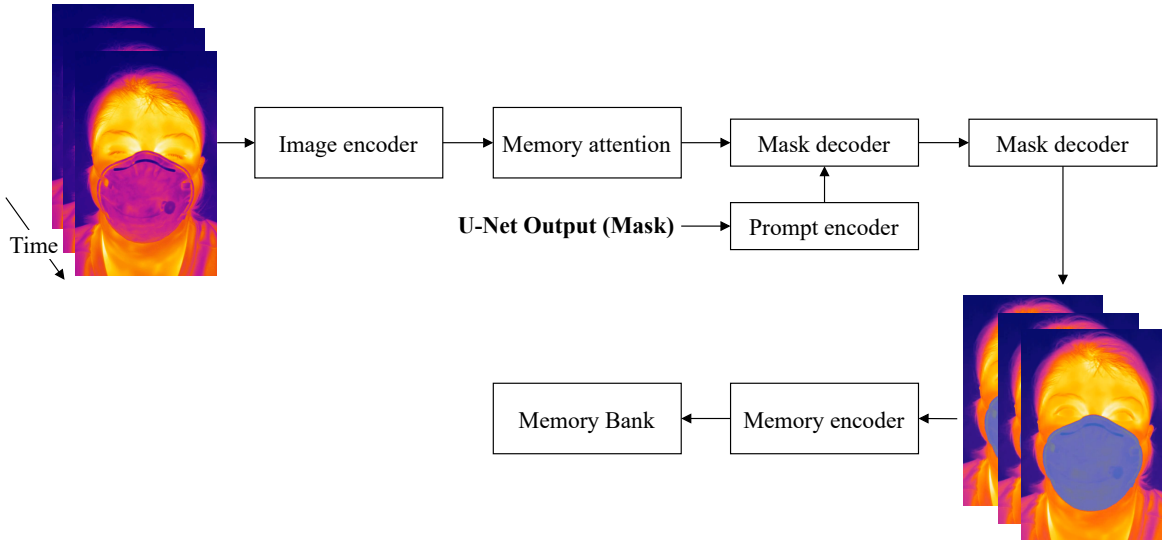

Fig. 2: Segmentation workflow for N95 masks in IR images using U-Net and SAM2.

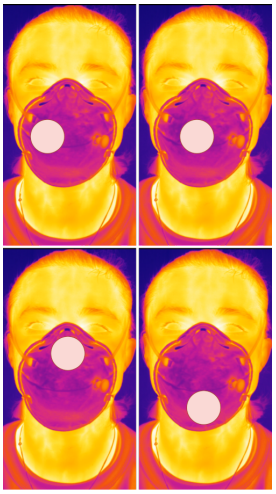

Fig. 3: Visualization of central ROI placement strategies.

$$\rho_{\text{Spearman}}(X,Y) = 1 - \frac{6\sum_{i=1}^{n}\left(R(x_i) - R(y_i)\right)^2}{n(n^2-1)} \tag{3}$$

This method is less sensitive to outliers and non-linear relationships.

c) Kendall's τ: Kendall's tau measures the correspondence between the rankings of the data by evaluating the number of concordant and discordant pairs. For two signals, Kendall's τ is given by:

$$\tau_{\text{Kendall}}(X,Y) = \frac{C-D}{\frac{1}{2}n(n-1)} \tag{4}$$

where C and D denote the numbers of concordant and discordant pairs, respectively. This non-parametric metric is robust to non-linear relationships.

d) Cross-Correlation: In addition to the rank-based measures, cross-correlation is utilized to evaluate the similarity between signals over various time lags. The raw cross-correlation function between X and Y is defined as:

$$R_{xy}(\tau) = \sum_{t=1}^{n} x_t\, y_{t+\tau} \tag{5}$$

where τ is the lag. To account for differences in signal scale and to ensure comparability, a normalized cross-correlation is computed as:

$$R_{xy}^{\text{norm}}(\tau) = \frac{\sum_{t=1}^{n}\left(x_t - \bar{x}\right)\left(y_{t+\tau} - \bar{y}\right)}{\sqrt{\sum_{t=1}^{n}\left(x_t - \bar{x}\right)^2}\sqrt{\sum_{t=1}^{n}\left(y_{t+\tau} - \bar{y}\right)^2}} \tag{6}$$

This normalized metric yields values within the interval $[-1, 1]$, facilitating the identification of ROIs whose frequency profiles closely match that of the central breathing signal.

e) Implementation: For each of the 100 peripheral ROIs, the corresponding frequency-domain signal (obtained via FFT) is compared with the normalized central ROI signal using the correlation methods described above. The peripheral ROI that exhibits the highest correlation with the central reference is flagged as a candidate leak region. By integrating multiple correlation measures, the framework enhances the robustness of leak localization, ensuring that subtle variations in the breathing signal are accurately detected.

D. Validation via Visualization of Leak Regions

The proposed method for visualizing mask leaks, termed *Pixel-wise Breathing Cycle Optical Flow Differential Imaging (PBC-OFDI)*, integrates ROI central selection with pixel-level tracking and differential thermal imaging to highlight leak regions on the human skin, thereby confirming leak localization along the mask contour. Initially. The central ROI is then tracked across successive frames using the Lucas-Kanade

optical flow algorithm, which is based on the brightness constancy assumption—stating that the intensity of a moving pixel remains approximately constant over a short time interval. Mathematically, for a pixel at position (x, y) in frame $I(x, y, t)$ that moves by (u, v) to $(x+u, y+v)$ in the subsequent frame, a first-order Taylor expansion provides:

$$I(x + u, y + v, t + 1) \approx I(x, y, t) + I_x\, u + I_y\, v + I_t \quad (7)$$

where I_x, I_y, and I_t represent the spatial and temporal intensity gradients. Enforcing brightness constancy leads to the constraint:

$$I_x\, u + I_y\, v + I_t = 0 \quad (8)$$

By collecting such equations for all n pixels within a local window W, the optical flow vector (u, v) is determined by minimizing:

$$\min_{u,v} \sum_{(x,y)\in W} \left(I_x(x, y)\, u + I_y(x, y)\, v + I_t(x, y)\right)^2 \quad (9)$$

This minimization is solved via the normal equations, expressed in matrix form as:

$$A^T A \begin{pmatrix} u \\ v \end{pmatrix} = -A^T b \quad (10)$$

with

$$A = \begin{bmatrix} I_x(x_1, y_1) & I_y(x_1, y_1) \\ \vdots & \vdots \\ I_x(x_n, y_n) & I_y(x_n, y_n) \end{bmatrix}, \quad b = \begin{bmatrix} I_t(x_1, y_1) \\ \vdots \\ I_t(x_n, y_n) \end{bmatrix} \quad (11)$$

This pixel-wise tracking ensures robust alignment of the ROI throughout the breathing cycle.

Subsequently, the mean pixel intensity within the tracked ROI is computed for each frame to generate a breathing signal that reflects thermal variations over time. Prominent peaks corresponding to exhalation and valleys corresponding to inhalation are then identified using peak detection techniques. For each breathing cycle, a pixel-wise differential temperature image is computed as:

$$D = I_{\text{exhalation}} - I_{\text{inhalation}} \quad (12)$$

and normalized to the range $[0, 1]$ using:

$$D_{\text{norm}} = \frac{D - \min(D)}{\max(D) - \min(D)} \quad (13)$$

A threshold is then applied to D_{norm} to isolate regions with significant thermal differences. To enhance visualization, the exhalation frame is converted to a RGB image and dimmed, while a FLIR-like colormap (e.g., JET) is applied to the thresholded difference image. Finally, contours that outline regions with significant temperature differences are extracted and overlaid on a dimmed background, effectively highlighting potential leak areas. In this process, the threshold for calculating the temperature difference (D) is set to be greater than 0, as pixels with no airflow have a D of 0. In contrast, pixels that show temperature variations between inspiration and expiration produce a nonzero D, indicating potential leaks.

This integrated approach—combining optical flow tracking, breathing cycle analysis, and differential thermal imaging—provides a detailed, pixel-wise visualization of mask leaks, thereby validating the accuracy of the leak localization achieved by the proposed framework.

V. Results and Discussion

This section presents the results of the experimental correlation analysis derived from thermal signal assessments. The subsequent tables (Tables I–V) summarize the correlation coefficients computed from the frequency-domain signals of the regions of interest (ROIs). The metrics utilized—namely, Pearson, Spearman, Kendall, cross-correlation and normalized cross-correlation values—serve to evaluate the similarity between the breathing reference signal from the central ROI and the signals obtained from 100 peripheral ROIs. A higher correlation suggests that a specific ROI demonstrates a thermal pattern that closely aligns with the breathing cycle, indicating a leak region.

This study evaluates mask performance based on the temperature difference (delta C) observed on human skin. This temperature differential, which mirrors the breathing pattern, has been validated in our previous section on visualization using the PBC-OFDI method. PBC-OFDI offers a detailed, pixel-wise representation of the temperature variations (delta C) and substantiates the localization of leaks along the mask perimeter.

The strategy for leak localization involves the automatic selection of the peripheral ROI exhibiting the highest correlation with the normalized central ROI. This ROI is then identified as a leak region. The comprehensive analysis conducted across multiple correlation measures confirms the robustness and reliability of the proposed framework for leak localization.

TABLE I: Correlation metrics for participant 29.

ID	Pearson	Spearman	Kendall	XCorrRaw	XCorrNorm
0	0.945	0.533	0.394	3.723e+06	0.909
1	0.942	0.573	0.466	3.377e+06	0.889
65	0.918	0.320	0.223	4.295e+06	0.818
2	0.905	0.455	0.348	8.998e+06	0.849
15	0.895	0.227	0.155	1.818e+06	0.753
12	0.869	0.037	0.019	3.082e+06	0.770
64	0.868	0.026	0.023	3.442e+06	0.740
13	0.857	0.172	0.114	2.287e+06	0.726

TABLE II: Correlation metrics for participant 11.

ID	Pearson	Spearman	Kendall	XCorrRaw	XCorrNorm
65	0.988	0.396	0.284	2.950e+06	0.959
56	0.983	0.309	0.227	5.520e+06	0.934
66	0.982	0.252	0.178	3.012e+06	0.954
68	0.981	0.226	0.152	2.662e+06	0.940
62	0.980	0.001	-0.034	2.828e+06	0.931
67	0.975	0.048	0.023	2.001e+06	0.922
74	0.974	0.316	0.239	5.041e+06	0.932
69	0.973	0.100	0.045	1.927e+06	0.909
63	0.971	-0.043	-0.045	2.096e+06	0.909

The correlation results demonstrate that higher correlation values between the peripheral ROIs and the central breathing signal—validated via the PBC-OFDI visualization of temperature differences (delta C)—indicate a stronger similarity in thermal patterns. This similarity is used to flag potential leak

TABLE III: Correlation metrics for participant 02.

ID	PEARSON	SPEARMAN	KENDALL	XCORRRAW	XCORRNORM
75	0.898	0.230	0.144	4.471e+05	0.814
72	0.864	0.455	0.371	9.922e+05	0.758
64	0.860	0.414	0.307	2.051e+06	0.749
76	0.858	0.151	0.114	3.942e+05	0.769
33	0.853	0.502	0.379	2.766e+05	0.730
18	0.847	0.253	0.167	2.049e+06	0.712
79	0.845	0.020	0.004	4.890e+05	0.726
78	0.837	-0.041	-0.034	4.954e+05	0.752

TABLE IV: Correlation metrics for participant 22.

ID	PEARSON	SPEARMAN	KENDALL	XCORRRAW	XCORRNORM
0	0.961	0.460	0.352	6.820e+06	0.835
32	0.893	0.476	0.356	9.965e+06	0.819
9	0.823	0.305	0.220	2.303e+06	0.678
1	0.820	0.432	0.314	3.277e+06	0.717
7	0.790	0.295	0.212	3.485e+06	0.648
65	0.772	0.556	0.417	3.959e+06	0.612
11	0.766	0.288	0.201	3.945e+06	0.683
3	0.766	0.549	0.420	3.420e+06	0.627
10	0.744	0.507	0.371	3.150e+06	0.651

regions. The automated decision process relies on identifying the peripheral ROI with the highest correlation with the normalized central ROI, thereby confirming the robustness and reliability of the proposed leak localization framework.

Fig. 4 and Fig. 5 illustrate the PBC-OFDI results for two representative participants, 02 and 22. In Fig. 4, the yellow regions clearly highlight areas with high delta T across the mask for Participant 22, particularly in the upper left region near the eyes. These visually identified leak areas correspond closely with the leakage locations indicated in Table IV, confirming that the correlation method accurately localizes the leaks. Similarly, Fig. 5 displays the PBC-OFDI output for Participant 02, where prominent yellow areas are observed in the right portion of the mask, specifically around ROIs 75, 72, 64, and 76. The consistency between these visualization results and the quantitative data demonstrates that the proposed correlation approach effectively identifies the precise leak regions.

VI. CONCLUSION & FUTURE WORK

The experimental results indicate that the correlation methods, particularly Pearson and cross- correlation when combined with normalization , yields robust and reliable leak localization by effectively capturing the breathing pattern. In contrast, Spearman and Kendall correlation measures did not correlate well with the periodicity of the breathing signal, likely due to their sensitivity to rank-based differences rather than absolute signal amplitude variations. This outcome reinforces the decision to rely on Pearson and normalized cross-correlation metrics for our framework.

The validation method based on PBC-OFDI, while useful for visualizing thermal differentials, presents limitations. Specifically, its accuracy depends heavily on the subject's movement; insufficient or excessive head motion can result in improper delta T calculation, leading to erroneous leak visualization. These constraints underscore the superiority of the proposed method, which maintains high performance even under natural head movements.

TABLE V: Correlation metrics for participant 33.

ID	PEARSON	SPEARMAN	KENDALL	XCORRRAW	XCORRNORM
0	0.945	0.533	0.394	3.723e+06	0.909
1	0.942	0.573	0.466	3.377e+06	0.889
65	0.918	0.320	0.223	4.295e+06	0.818
2	0.905	0.455	0.348	8.998e+06	0.849
15	0.895	0.227	0.155	1.818e+06	0.753
12	0.869	0.037	0.019	3.082e+06	0.770
64	0.868	0.026	0.023	3.442e+06	0.740
13	0.857	0.172	0.114	2.287e+06	0.726
14	0.850	0.210	0.155	1.756e+06	0.701

Future work will focus on further enhancing the system's adaptability by extending leak detection to additional regions of the mask, such as the upper eye area. Moreover, efforts will be directed towards improving head tracking algorithms to extract reliable thermal information from these regions, thereby broadening the scope of the framework and ensuring its efficacy under more diverse real-world conditions. Additionally , the proposed U-Net segmentation model has been optimized beyond conventional *state-of-the-art* U-Net variants to achieve an optimal balance of inference speed and segmentation accuracy. Future work also will focus on streamlining the interaction between this optimized U-Net and the SAM2 contour refinement stage through joint architecture design and lightweight fusion modules to enable high-speed, end-to-end leak detection suitable for real-time deployment.

REFERENCES

[1] S. Lam, J. Lee, S. Yau, and C. Charm, "Sensitivity and specificity of the user-seal-check in determining the fit of n95 respirators," *Journal of Hospital Infection*, vol. 77, no. 3, pp. 252–256, 2011.

[2] T. Greenhalgh, C. R. MacIntyre, M. G. Baker, S. Bhattacharjee, A. A. Chughtai, D. Fisman, M. Kunasekaran, A. Kvalsvig, D. Lupton, M. Oliver *et al.*, "Masks and respirators for prevention of respiratory infections: a state of the science review," *Clinical microbiology reviews*, vol. 37, no. 2, pp. e00 124–23, 2024.

[3] L. Boulos, J. A. Curran, A. Gallant, H. Wong, C. Johnson, A. Delahunty-Pike, L. Saxinger, D. Chu, J. Comeau, T. Flynn *et al.*, "Effectiveness of face masks for reducing transmission of sars-cov-2: a rapid systematic review," *Philosophical Transactions of the Royal Society A*, vol. 381, no. 2257, p. 20230133, 2023.

[4] D. J. Viscusi, M. S. Bergman, Z. Zhuang, and R. E. Shaffer, "Evaluation of the benefit of the user seal check on n95 filtering facepiece respirator fit," *Journal of occupational and environmental hygiene*, vol. 9, no. 6, pp. 408–416, 2012.

[5] C. E. Rodriguez-Martinez, M. P. Sossa-Briceño, and J. A. Cortés, "Decontamination and reuse of n95 filtering facemask respirators: a systematic review of the literature," *American journal of infection control*, vol. 48, no. 12, pp. 1520–1532, 2020.

[6] B. Topilko, G. Marchais, M. Arbane, J. Brousseau, A. Bahloul, X. Maldague, C. Brochot, and Y. Yaddaden, "Development of multi-physics models for the study of airflow and thermal effects during the use of filtering facepiece respirators," in *2024 9th International Conference on Computer Science and Engineering (UBMK)*. IEEE, 2024, pp. 1–7.

[7] S. N. Mohammed and F. S. Alkinani, "Biometrics systems challenges in a post-covid-19 pandemic world: A review," *Al-Mansour Journal*, vol. 39, no. 1, pp. 1–27, 2023.

[8] G. Marchais, B. Topilko, M. Arbane, J. Brousseau, C. Brochot, Y. Yaddaden, A. Bahloul, and X. Maldague, "A test bench for replicating human breathing: Evaluating thermal effects of n95 filtering facepiece respirator leaks – preliminary findings," in *2024 9th International Conference on Computer Science and Engineering (UBMK)*, 2024, pp. 695–700.

[9] G. Marchais, M. Arbane, B. Topilko, J. Brousseau, C. Brochot, Y. Yaddaden, A. Bahloul, and X. Maldague, "Saferespirator: Comprehensive database for n95 filtering facepiece respirator leak detection including infrared, rgb videos, and quantitative fit testing," *IEEE Access*, 2024.

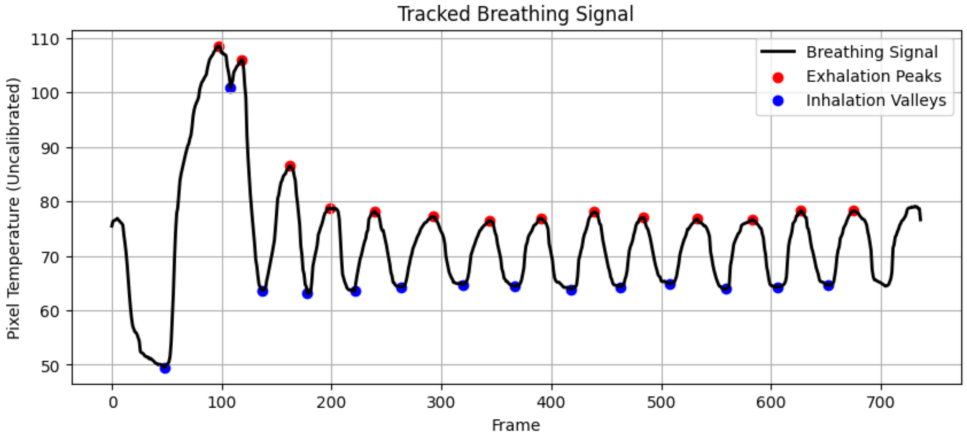

Fig. 4: PBC-OFDI visualization for participant 22.

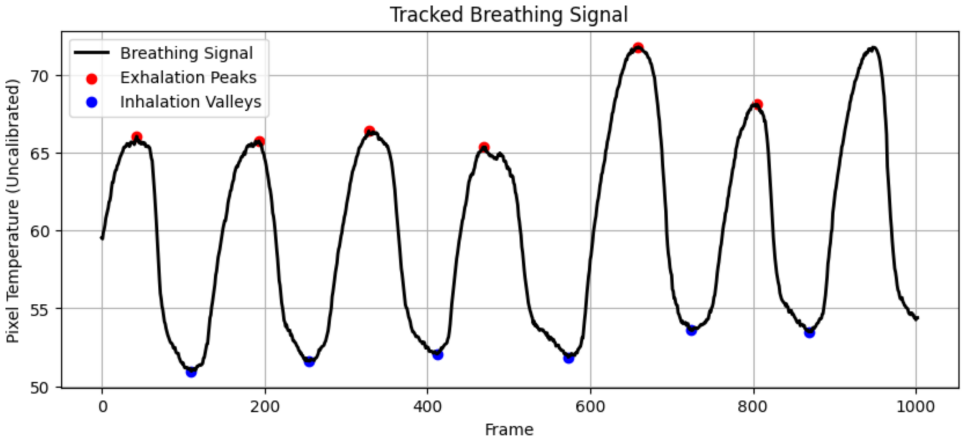

Fig. 5: PBC-OFDI visualization for participant 02.

[10] M. Ippolito, F. Vitale, G. Accurso, P. Iozzo, C. Gregoretti, A. Giarratano, and A. Cortegiani, "Medical masks and respirators for the protection of healthcare workers from sars-cov-2 and other viruses," *Pulmonology*, vol. 26, no. 4, pp. 204–212, 2020.

[11] A. Regli, A. Sommerfield, and B. von Ungern-Sternberg, "The role of fit testing n95/ffp2/ffp3 masks: a narrative review," *Anaesthesia*, vol. 76, no. 1, pp. 91–100, 2021.

[12] H. Kim, T. M. Kim, S. W. Choi, and T. Ko, "Thermal imaging and deep learning-based fit-checking for respiratory protection," *Scientific Reports*, vol. 14, no. 1, p. 24407, 2024.

[13] P. Harber, J. Su, A. D. Badilla, R. Rahimian, and K. R. Lansey, "Potential role of infrared imaging for detecting facial seal leaks in filtering facepiece respirator users," *Journal of occupational and environmental hygiene*, vol. 12, no. 6, pp. 369–375, 2015.

[14] Y. Yaddaden, M. Adda, A. Bouzouane, S. Gaboury, and B. Bouchard, "User action and facial expression recognition for error detection system in an ambient assisted environment," *Expert Systems with Applications*, vol. 112, pp. 173–189, 2018.

[15] D. Müller, A. Ehlen, and B. Valeske, "Convolutional neural networks for semantic segmentation as a tool for multiclass face analysis in thermal infrared," *Journal of nondestructive evaluation*, vol. 40, no. 1, p. 9, 2021.

[16] D. Chapman, C. Strong, K. D. Tiver, D. Dharmaprani, E. Jenkins, and A. N. Ganesan, "Infra-red imaging to detect respirator leak in healthcare workers during fit-testing clinic," *IEEE Open Journal of Engineering in Medicine and Biology*, vol. 5, pp. 198–204, 2023.

[17] G. Kaur, R. Sinha, P. K. Tiwari, S. K. Yadav, P. Pandey, R. Raj, A. Vashisth, and M. Rakhra, "Face mask recognition system using cnn model," *Neuroscience Informatics*, vol. 2, no. 3, p. 100035, 2022.

[18] M. Arbane, G. Marchais, B. Topilko, Y. Yaddaden, J. Brousseau, C. Brochot, A. Bahloul, and X. Maldague, "Enhanced face mask segmentation on infrared images using lightweight u-net techniques," in *IEEE International Multi-Conference on Smart Systems & Green Process*. IEEE, 2024, pp. 1–6.

[19] N. Ravi, V. Gabeur, Y.-T. Hu, R. Hu, C. Ryali, T. Ma, H. Khedr, R. Rädle, C. Rolland, L. Gustafson *et al.*, "Sam 2: Segment anything in images and videos," *arXiv preprint arXiv:2408.00714*, 2024.

Chapitre 5

Titre :
L'imagerie infrarouge et l'apprentissage profond pour améliorer la détection et la localisation des fuites de PFF N95

Résumé - *Assurer l'étanchéité des respirateurs N95 est crucial pour une protection respiratoire efficace, cependant, même des fuites minimes peuvent compromettre leur efficacité. Les méthodes traditionnelles de test d'ajustement, qualitatives (saccharine ou Bitrex) ou quantitatives (PortaCount®), nécessitent du personnel spécialisé et beaucoup de temps, limitant leur capacité à effectuer une surveillance continue en temps réel. Cet article propose une méthodologie innovante combinant l'imagerie infrarouge et l'apprentissage profond pour détecter et localiser précisément les fuites des PFF en temps réel. La technique développée utilise une extraction de caractéristiques basée sur le réseau ResNet50 et une classification par vecteurs de support (SVM) afin de distinguer efficacement les conditions avec et sans fuite. En complément, une méthode de localisation basée sur la corrélation identifie précisément les emplacements des fuites en analysant la correspondance entre la signature thermique respiratoire centrale et les signaux des régions segmentées sur le contour du PFF. Des tests rigoureux menés sur des surfaces planes, des mannequins et des participants humains montrent que cette approche atteint une précision supérieure à 95 % en conditions contrôlées et valide sa robustesse dans des scénarios dynamiques réels. Cette approche novatrice permet une surveillance rapide, continue et non invasive des PFF N95, renforçant significativement la sécurité dans les environnements médicaux et industriels à risque. Les futures recherches viseront à perfectionner l'intégration de cette technologie dans des systèmes de surveillance en temps réel plus larges.*

Mots clés :
PFF N95, Thermographie infrarouge, Apprentissage profond, Détection de fuites, Test d'ajustement respiratoire, Localisation par corrélation, Équipement de protection individuelle (EPI)

Contributions associées :
Arbane, Mohamed, et al. "Infrared Imaging and Deep Learning for Enhanced Detection and Localization of Mask Leaks." 2025 Elsevier Infrared Physics & Technology. (Statut : soumis)

Contributions des auteurs :
Conceptualisation : Mohamed Arbane , Geoffrey Marchais ; méthodologie : Mohamed Arbane ; logiciel :Mohamed Arbane ; validation : Yacine Yaddaden, Jean Brousseau, Clothilde Brochot ; ressources :Xavier Maldague , Clothilde Brochot ; rédaction — préparation de la version originale : Mohamed Arbane ; rédaction — révision et édition : Mohamed Arbane, Yacine Yaddaden, Jean Brousseau, Ali Bahloul, Clothilde Brochot , Xavier Maldague ; supervision : Yacine Yaddaden , Jean Brousseau , Clothilde Brochot, Ali Bahloul, Xavier Maldague.

Infrared Physics and Technology

Infrared Imaging and Deep Learning for Enhanced Detection and Localization of Mask Leaks

--Manuscript Draft--

Manuscript Number:	INFPHY-D-25-01088
Article Type:	Research Paper
Keywords:	N95 respirator; Infrared thermography; Deep learning; Leak detection; Respiratory fit test; Correlationbased localization; Personal protective equipment (PPE)
Corresponding Author:	Mohamed Arbane, M.S student University of Quebec at Rimouski CANADA
First Author:	Mohamed Arbane, student
Order of Authors:	Mohamed Arbane, student
	Yacine Yaddaden
	Jean Brousseau
	Geoffrey Marchais, Ph.d Student
	Clothilde Brochot
	Ali Bahloul
	Xavier Maldague
Manuscript Region of Origin:	North America
Abstract:	Highlights Ensuring a tight seal in N95 respirators is crucial for effective respiratory protection; however, even minor leaks can significantly reduce filtration efficiency. Conventional mask fit testing methods, such as qualitative (saccharin or Bitrex) and quantitative (PortaCount® fit tester) approaches, require dedicated personnel and considerable time, thus lacking real-time monitoring capabilities. To address these limitations, this paper proposes a novel infrared imaging and deep learning framework for real-time detection and localization of mask leaks. The proposed method achieves over 95% accuracy in controlled validation tests conducted on both a flat panel and mannequin faces, with precisely induced leak sizes quantitatively benchmarked using a PortaCount® fit tester. The methodology utilizes ResNet50-based feature extraction combined with a Support Vector Machine (SVM) classifier to robustly differentiate between leak and noleak conditions. Additionally, a correlation-based localization technique accurately identifies leak locations by matching the mask's central respiratory thermal signature with signals from segmented regions along the mask contour. Evaluations conducted on human participants further demonstrate the method's reliability and its potential for rapid, non-invasive, and continuous monitoring, thus significantly enhancing safety in healthcare and industrial environments where N95 masks are critical.
Opposed Reviewers:	

Highlights

Infrared Imaging and Deep Learning for Enhanced Detection and Localization of Mask Leaks

Mohamed Arbane,Yacine Yaddaden,Jean Brousseau,Geoffrey Marchais ,Clothilde Brochot,Ali Bahloul,Xavier Maldague

- Developed an infrared imaging protocol for pinpointing leaks, benchmarked by PortaCount® measurements.
- Combined ResNet50 feature extraction with SVM to robustly classify leak vs. no-leak conditions.
- Introduced a contour-based correlation method to precisely locate leaks in real time.

Infrared Imaging and Deep Learning for Enhanced Detection and Localization of Mask Leaks[⋆,⋆⋆]

Mohamed Arbane[a], Yacine Yaddaden[a], Jean Brousseau[a], Geoffrey Marchais [a], Clothilde Brochot[b], Ali Bahloul[b] and Xavier Maldague[c]

[a]Department of Mathematics, Computer Science, and Engineering,University of Quebec at Rimouski, Rimouski, G5L 3A1, Canada
[b]Institut de Recherche Robert-Sauvé en Santé et en Sécurité du Travail (IRSST), Montreal, H3A 3C2, Canada
[c]Department of Electrical and Computer Engineering, Laval University, Quebec City, G1V 0A6, Canada

ARTICLE INFO

Keywords:
N95 respirator; Infrared thermography; Deep learning; Leak detection; Respiratory fit test; Correlation-based localization; Personal protective equipment (PPE)

ABSTRACT

Ensuring a tight seal in N95 respirators is crucial for effective respiratory protection; however, even minor leaks can significantly reduce filtration efficiency. Conventional mask fit testing methods, such as qualitative (saccharin or Bitrex) and quantitative (PortaCount® fit tester) approaches, require dedicated personnel and considerable time, thus lacking real-time monitoring capabilities. To address these limitations, this paper proposes a novel infrared imaging and deep learning framework for real-time detection and localization of mask leaks. The proposed method achieves over 95% accuracy in controlled validation tests conducted on both a flat panel and mannequin faces, with precisely induced leak sizes quantitatively benchmarked using a PortaCount® fit tester. The methodology utilizes ResNet50-based feature extraction combined with a Support Vector Machine (SVM) classifier to robustly differentiate between leak and no-leak conditions. Additionally, a correlation-based localization technique accurately identifies leak locations by matching the mask's central respiratory thermal signature with signals from segmented regions along the mask contour. Evaluations conducted on human participants further demonstrate the method's reliability and its potential for rapid, non-invasive, and continuous monitoring, thus significantly enhancing safety in healthcare and industrial environments where N95 masks are critical.

1. Introduction

N95 filtering facepiece respirators (FFRs) are vital in healthcare, but their effectiveness is critically undermined by face seal leaks. Even minor gaps between the mask and face can lead to significant inward leakage of unfiltered air, sharply increasing the risk of airborne disease transmissionSchmitt and Wang (2022).Modeling studies show that a poorly fitted N95 may allow 30–95% of aerosols to bypass the filter, whereas a properly fit-tested respirator keeps leakage to minimal levels (infections 12% vs. 42–80% without fit) Hariharan, Sharma, Guha, Banerjee, D'Souza and Myers (2021). These findings underscore that mask fit and seal integrity are as important as the filter media in preventing contagion.

Conventional fit-testing methods are used to check N95 fit before use. Qualitative fit tests (e.g. saccharin or Bitrex aerosols) introduce a sweet or bitter aerosol around the hood of a masked subject; if the wearer can taste the agent, the mask is leaking. Quantitative fit tests use instruments like the TSI PortaCount® to measure particle concentrations inside vs. outside the mask and compute a numerical fit factor Lam, Odetayo, Yu, So, Cheung, Lee and Suen (2023). While effective for initial screening, these tests have notable limitations. They are time-intensive, require trained personnel and specialized equipment, and are typically performed infrequently (e.g. annually) rather than during routine mask use. Moreover, standard fit tests involve a set of scripted exercises and may not capture seal failures during more active or prolonged tasks. The studies have observed that even respirators which pass a fit test can exhibit substantial real-time leakage when healthcare workers move or exert themselves in clinical procedures. This gap highlights the need for continuous, real-time monitoring of mask fit.

Infrared (IR) thermography has emerged as a promising non-contact approach to detect mask leaks. Warm exhaled breath escaping through imperfect seals creates thermal plumes that are visible to IR cameras Koroteeva and

*Corresponding author
**Principal corresponding author
mohamed.arbane@uqar.ca (M. Arbane)
ORCID(s):

Shagiyanova (2022). By imaging the temperature variations around the mask, IR thermography can directly visualize where hot breath is leaking out Marchais, Arbane, Topilko, Brousseau, Brochot, Yaddaden, Bahloul and Maldague (2024a). Researchers have demonstrated that IR imaging clearly reveals air leakage at the mask edges and through materials; for example, thermal camera studies showed pronounced airflow escape around the periphery of surgical and cloth masks, whereas a well-fitted N95 showed virtually no such thermal leakage signature. IR leak detection is completely noninvasive and can be performed on healthcare workers in real time without affecting their breathing, offering a practical route to assess respirator sealing continuously.

Integrating artificial intelligence (AI) with IR thermography further enhances leak detection capabilities. Automated computer vision algorithms can analyze IR video frames to rapidly identify leak locations and assess seal quality, improving both speed and objectivity of detection. Advanced AI models have been explored for this task. In this paper, we present a novel IR-AI framework for N95 fit evaluation that addresses the above challenges. The proposed system combines infrared thermography with machine learning to automatically detect and localize face seal leaks. We validate the framework on both mannequin headforms and human participants wearing N95 FFRs under various breathing conditions. Our approach employs a two-stage CNN–SVM pipeline: a convolutional neural network first processes the IR video to recognize breathing events and potential leak signatures, and its outputs are fed into a support vector machine classifier to robustly distinguish between properly sealed and leaking masks. In addition to classification, a correlation-based analysis of thermal patterns is used to pinpoint the exact locations of any leaks on the mask perimeter. This integrated IR and AI methodology enables fast, noninvasive identification of respirator leaks in real time, providing a foundation for improved respiratory protection monitoring in healthcare and occupational safety contexts.

The main contributions of this study include:

- Validated Infrared-Based Leak Detection Protocol leveraging a controlled mannequin setup and PortaCount® verification for precise ground truth.
- CNN-SVM Classification Pipeline that extracts deep features via transfer learning for robust leak vs. no-leak discrimination.
- Segmentation and Correlation-Based Localization Algorithm allowing real-time leak mapping along the mask contour, adapted to both static and dynamic wearing conditions.

Collectively, these advances lay the groundwork for continuous, user-friendly monitoring of N95 masks, potentially enhancing safety in critical healthcare and industrial settings.

2. Related Work

Proper respirator and face mask fit is crucial for effective protection, as even small face-seal leaks can significantly degrade filtration performance Roberge, Monaghan, Palmiero, Shaffer and Bergman (2011); Harber, Su, Badilla, Rahimian and Lansey (2015). Studies have shown that faceseal leakage often contributes more to wearers' exposure than filter media penetration Viscusi, Bergman, Zhuang and Shaffer (2012); Lee, Grinshpun and Reponen (2008). Simple user seal checks (fit checks) are notoriously unreliable in detecting leaks, with low sensitivity and poor predictive value Derrick, Chan, Gomersall and Lui (2005); O'Kelly, Arora, Pirog, Ward and Clarkson (2021). Early investigations found that routine self-checks by wearers fail to detect many leaks and cannot substitute formal fit testing Viscusi et al. (2012). Quantitative fit testing remains the gold standard but requires specialized equipment and can be time-consuming, motivating research into imaging-based leak detection methods that offer rapid, noninvasive fit assessment.

Infrared (IR) thermography visualizes temperature differences caused by exhaled air leaking from masks, revealing warm airflow escaping through leaks against cooler backgrounds Roberge et al. (2011); Harber et al. (2015). Roberge et al. pioneered this technique using an IR camera during N95 respirator fit tests, detecting leaks especially around the nose and cheeks, correlating with lower fit factors Roberge et al. (2011). Similarly, Harber et al. used IR video to confirm significant leaks at the nasal bridge and cheeks, correlating thermal leak imagery with quantitative fit factors Harber et al. (2015). However, IR imaging alone was not sufficient to fully replace standard fit tests due to limited sensitivity for fine leaks Siah, Lau, Tng and Chua (2022).

Recent advancements integrating IR imaging with machine learning have enhanced leak detection effectiveness. Siah et al. combined infrared thermography with deep learning, using convolutional neural networks to distinguish

between good and poor mask fits automatically Siah et al. (2022). Chapman et al. integrated IR cameras into P2/N95 respirators, applying machine learning to real-time temperature gradients to predict quantitative fit outcomes accurately Chapman, Strong, Tiver, Dharmaprani, Jenkins and Ganesan (2024). Kim et al. captured thermal videos and employed 3D convolutional neural networks, achieving high accuracy in distinguishing correct and incorrect mask usage across multiple mask types Kim, Kim, Choi and Ko (2024).

In addition to infrared, other imaging modalities like schlieren optical imaging highlight refractive index gradients in air, qualitatively visualizing mask airflow leakage Tanışalı, Sozak, Bulut, Sander, Özlem Doğan, Çağdaş Dağ, Gönen, Can, DeMirci and Önder Ergonul (2021); Staymates (2020). Tanışalı et al. used schlieren to demonstrate that well-fitted respirators significantly minimize leakage compared to loosely fitted masks Tanışalı et al. (2021). Staymates visualized airflow with and without exhalation valves, illustrating substantial differences in respiratory droplet containment effectiveness Staymates (2020). Similarly, Verma et al. highlighted leakage paths using laser light scattering and schlieren, demonstrating the ineffectiveness of masks with exhalation valves or face shields in controlling respiratory emissions Verma, Dhanak and Frankenfield (2020b,a).

Beyond visualization, analytical and simulation-based approaches have also been pursued. Oestenstad and Bartolucci identified reproducible leak locations and shapes on respirators through analytical modeling Oestenstad and Bartolucci (2010). Wang et al. used 3D morphable face models to correlate facial features with mask leakage tendencies, predicting poor-fitting facial geometries Wang, Solano and Shoele (2022). Lei et al. validated computational fluid dynamics (CFD) models of mask leaks using IR observations, accurately predicting primary leak sites like the nasal region and quantifying leak effects Lei, Yang, Zhuang and Roberge (2013).

Overall, the literature underscores the importance of mask fit in determining respirator effectiveness, with imaging-based techniques addressing limitations of subjective methods. Early aerosol tracer studies highlighted significant exposure from small leaks Liu, Lee, Mullins and Danisch (1993); Hinds and Bellin (1987). Modern infrared thermography visualizes leaks in real-time, already applied successfully in healthcare and industrial settings Roberge et al. (2011); Kerl, Wenzel and Köhler. Combining IR imaging with advanced machine learning techniques is bridging the gap in sensitivity and enabling rapid, automatic fit evaluation, crucial in high-risk environments to ensure effective respiratory protection Kim et al. (2024); Chapman et al. (2024).

3. Methodology

3.1. Experimental Setup

To validate the proposed framework for detecting and localizing mask leaks, a thorough experimental setup was established featuring three distinct configurations: a flat panel surface, a life-sized mannequin head, and actual human faces. Each configuration is tailored to replicate various N95 mask-wearing conditions, ensuring that the system undergoes rigorous evaluation in both controlled and, importantly, realistic scenarios.

3.1.1. Flat Panel and Mannequin Head Configurations

The flat panel provides a stable, planar surface that facilitates precise and reproducible leak induction, while the mannequin head offers a controlled yet realistic simulation of human facial features Marchais, Topilko, Arbane, Brousseau, Brochot, Yaddaden, Bahloul and Maldague (2024b). In both configurations, N95 masks were securely fitted, and controlled leaks were artificially induced at predefined locations along the mask contour using standardized plugs and needles, as illustrated in subfigures (c) and (d) of Figure 1. Figure 2 details the modeling aspects of both the mannequin head and flat panel surfaces, and Figure 3 demonstrates the complete installation setup, including the integration of a mechanical ventilator. This ventilator simulates consistent respiratory cycles by delivering warm, humid air, closely mimicking natural exhalation.

The mannequin employed was a life-sized head model with realistic facial features to mimic human mask-wearing scenarios. N95 masks used in these experiments were procured from certified suppliers, ensuring compliance with filtration and fit standards. The mask was meticulously placed on the mannequin, and infrared cameras captured thermal images during simulated respiratory cycles. The attached mechanical ventilator provided a consistent flow of warm, humid air akin to human breathing, enabling reproducible data collection. This setup allowed for precise analysis of potential mask leaks within a controlled environment, establishing a strong baseline prior to extending the methodology to human participants.

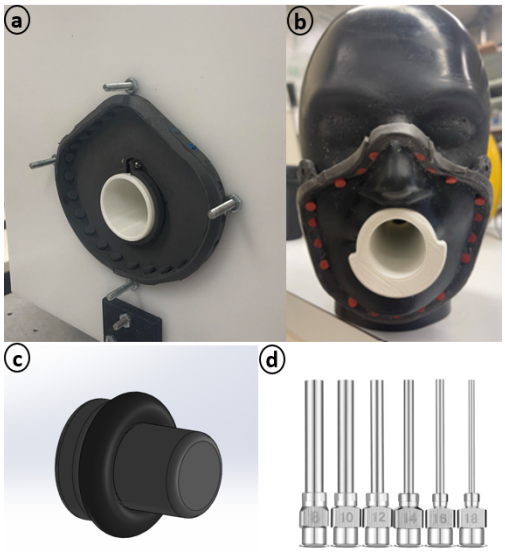

Figure 1: Controlled Testing Setup and Leak Introduction.Marchais et al. (2024b)

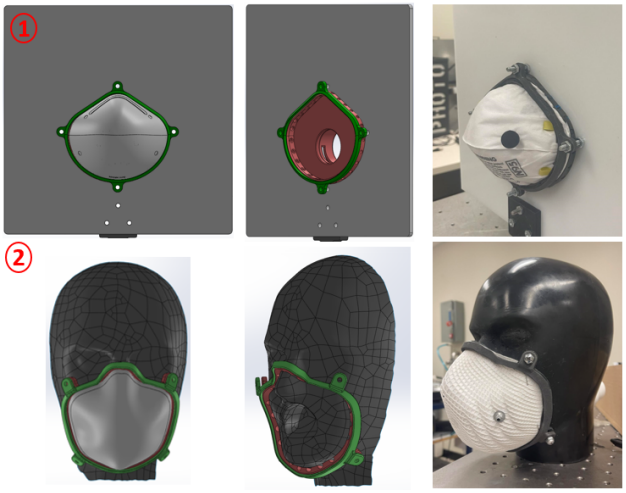

Figure 2: Modeling of the Mannequin and Plate Surfaces.Marchais et al. (2024b)

3.1.2. Human Subject Testing

The experiments were involving real human subjects to validate the model under realistic conditions.As shown in Figure 4, participants faced the infrared camera, and the complete data collection protocol is detailed in Marchais et al. (2024b). Participants were asked to wear N95 masks, ensuring proper placement and fit. Infrared cameras were positioned to capture the mask's contour and detect any thermal anomalies that could indicate a leak. All participants provided informed consent, and the testing followed institutional guidelines for safety and privacy. The movement of the subjects, including head turns and routine activities, was recorded to evaluate the model's robustness in real-life scenarios. This dynamic testing helped assess the influence of facial movements, breathing variability, and mask adjustments on leak detection accuracy.

3.1.3. Infrared Imaging System

A high-resolution infrared camera (FLIR X8501sc Infrared Camera, Fli) was used to capture thermal emissions from the mask's surface. The camera was positioned fixed to ensure consistent imaging for all experiments. The infrared camera's thermal sensitivity allowed us to detect even minor temperature variations, which is crucial for identifying

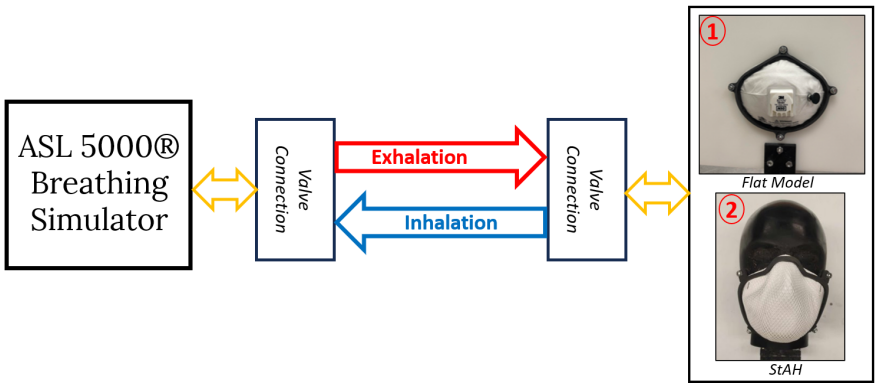

Figure 3: Installation Setup with Simulated Breathing Cycles. Marchais et al. (2024b)

Figure 4: Human Participant Testing Setup. Marchais et al. (2024b)

small leaks. The imaging system was calibrated to capture thermal contrast between the ambient environment and the exhaled breath, highlighting potential leakage areas.

3.1.4. Data Collection and Preprocessing

The data collection process involved capturing infrared thermal images of the N95 masks during static (Flat and Mannequin head) and dynamic (human subject) conditions.

Each row in Table 1 corresponds to a specific leak test scenario, where the *Leaks info* column encodes three elements: the first number denotes the general region of the mask (e.g., upper-left, upper-right, lower-left, or lower-right), the second number is an internal reference for the leak site within that region, and the third component specifies the leak size. The suffix "G" (e.g., 8G, 10G, 12G, etc.) maps to approximate millimeter values, such as 8G $\approx$ 3.5 mm, 10G $\approx$ 3.0 mm, 12G $\approx$ 2.3 mm, 14G $\approx$ 1.6 mm, 15G $\approx$ 1.32 mm, 16G $\approx$ 1.2 mm, 17G $\approx$ 1.12 mm, and 18G $\approx$ 0.84 mm. The *FF_Means* column represents the mean Fit Factor (FF) obtained after three repeated tests, while the *No. of leaks* column indicates how many distinct leaks were present in that test configuration. This structured information helps in systematically correlating leak locations and sizes with fit-test outcomes.

Table 1
Summary of Leak Information and Measurements

Numéro Test	Leaks info	FF_Means	No. of leaks
1	[4,5;8G]	42,6	1
2	[2,1;8G]	47,8	1
3	[2,4;8G]	42,2	1
4	[4,1;12G]	127,8	1
5	[2,2;14G]	120	1
6	[4,4;12G]	99,6	1
50	[3,3;8G]	55,6	1
51	[4,2;12G]	91	1
52	[2,3;15G]	176,8	1
53	[3,4;14G]	200,8	1
54	[4,2;10G]	80,8	1
57	[2,5;16G]	200	1
70	[1,4;10G] + [4,4;10G]	41,6	2
71	[2,2;12G] + [3,3;8G]	26,8	2
72	[3,4;12G] + [4,2;14G]	90,2	2
73	[2,1;14G] + [3,5;16G]	138,4	2
75	[2,4;16G] + [3,3;12G]	106,6	2
88	[2,2;8G]+[3,3;10G]+[4,4;12G]	27,4	3
89	[1,1;8G]+[4,3;8G]+[3,4;8G]	18,2	3

4. Leaks localisation Methodology & Proposed Approach

4.1. Mannequin Head: Controlled Leak Localization Methodology

The controlled leak localization methodology is demonstrated using both a flat panel and a stationary mannequin head, which together provide a stable baseline by minimizing variations unrelated to respiratory activity. These controlled configurations facilitate precise leak induction and reliable analysis.

Contour Definition and Signal Extraction: A contour is delineated along the perimeter of the N95 mask in both the flat panel and mannequin head setups to define regions where leaks are most likely to occur. Infrared thermal signals are extracted at uniformly spaced points along this contour, capturing temperature fluctuations during each breathing cycle.

Spectrogram Generation and Classification: The Fast Fourier Transform (FFT) is uniformly applied to these extracted temperature signals to generate spectrograms that reveal the frequency components of the thermal variations Safdar, Nowak and Pałka (2022). These spectrograms serve as inputs to a classification model that leverages a pre-trained ResNet architecture Koonce and Koonce (2021) for feature extraction followed by a Support Vector Machine (SVM) classifier to distinguish between leak and no-leak conditions, as illustrated in Figure 5.

ROI Partitioning and Correlation Analysis Upon leak detection, the task advances to exact localization. The mask contour is partitioned into 100 uniformly sized Regions of Interest (ROIs), each identified by a distinct index. The FFT analysis is performed on these individual contour segments to generate a spectrogram for every ROI.

A control spectrogram is extracted from the mask's central area, assumed to exhibit normal exhalation characteristics. Employing a correlation-based comparison between the respiratory frequency in each ROI's spectrogram and that of the central region allows identification of the ROI(s) corresponding to the leak frequency. Figure 6 depicts the ROI layout along the contour in relation to the central spectral profile, while Figure 7 highlights sample ROI indices (5, 10, 20, 40, 60, 80, and 88) for enhanced clarity.

4.1.1. Proposed Classification Model

The leak detection framework for the static heads utilizes a two-phase classification pipeline to determine whether a segment of the mask contour is in a leak or no-leak condition (i.e., pass or fail) as shown in Figure 5 . The pipeline is structured as follows:

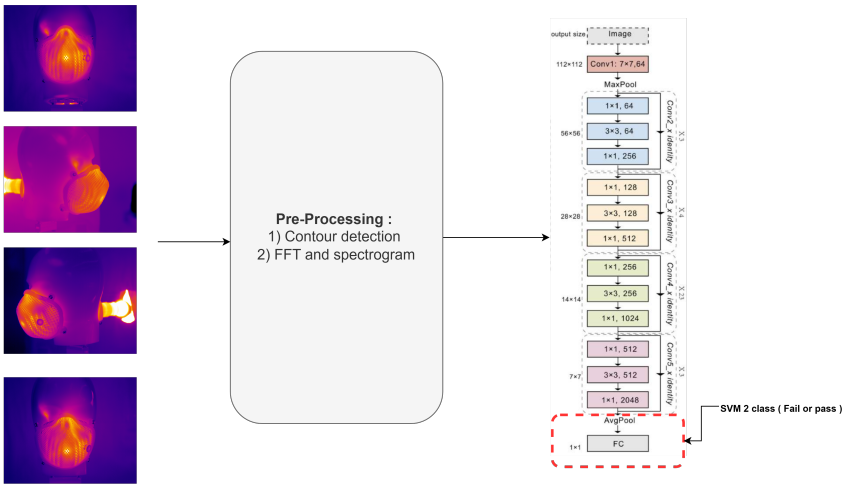

Figure 5: Proposed Method for Leaks Detection.

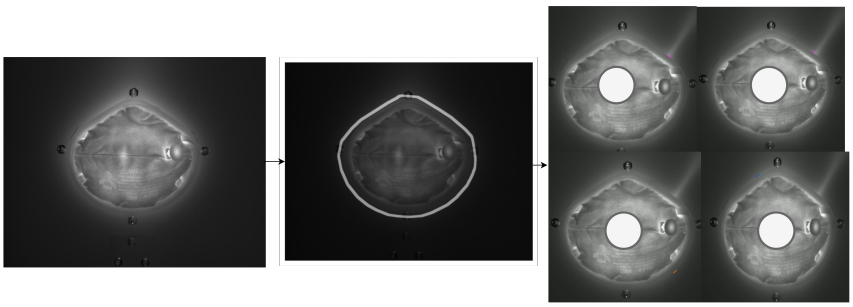

Figure 6: Contour Subdivision and Correlation-Based Leak Localization

Phase 1: Transfer Learning (ResNet50) First, by converting the temporal temperature signals captured along the mask's contour into spectrograms using the Fast Fourier Transform (FFT). These spectrograms depict the frequency distribution of the thermal variations and form the input to our transfer learning model. Specifically, the employment of ResNet50 architecture that has been pre-trained on large-scale image datasets. By re-purposing the network's convolutional layers, the leverage powerful feature extraction capabilities even with a relatively small number of training samples.

In practice, each spectrogram is resized or padded as needed to match the input dimensions of ResNet50. The final convolutional layers of the network provide high-level features that represent the temporal and frequency patterns associated with the respiratory signals of the mask. This feature extraction stage is critical for capturing subtle leak signatures, which often manifest as unique frequency-domain anomalies of the leaks.

Phase 2: SVM Classification Once the ResNet50-based feature vectors are extracted, these representations are fed into a binary Support Vector Machine (SVM) classifier. The SVM is trained to distinguish between two classes: *Leak* (fail) and *No-Leak* (pass).

This two-phase approach balances the strengths of deep learning and classical machine learning methods. The ResNet50 network encodes the complex spectro-temporal information into a compact, discriminative feature set, while the SVM robustly handles the final decision boundary.

4.1.2. Correlation Method

Once the classification model flags a potential leak, the next step is localization by subdividing the mask contour into multiple Regions of Interest (ROIs). Each ROI corresponds to a segment of the mask boundary where a leak may

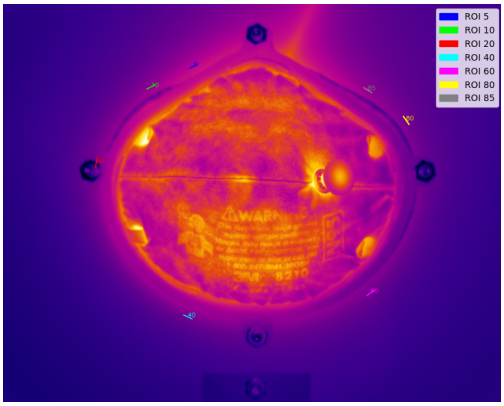

Figure 7: Representative ROI indices along the mask contour.

occur. From each ROI, the extraction of the thermal signal over time—often post-processed into the frequency domain via the Fast Fourier Transform (FFT)—and compare it with a reference respiratory signal obtained from the mask's center (see Figure 6). This comparison uses statistical correlation measures to identify which ROI's signal most closely matches the breathing pattern, thereby indicating a likely leak site.

Below, the outline the principal correlation measures considered in the analysis part. Let

$$X = \{x_1, x_2, \dots, x_n\} \quad \text{and} \quad Y = \{y_1, y_2, \dots, y_n\}$$

be two discrete signals (ROI signal and the center reference).

1) Pearson Correlation A common measure of linear dependence is the *Pearson correlation coefficient*, ρ_{Pearson}, defined as:

$$\rho_{\text{Pearson}}(X,Y) = \frac{\sum_{i=1}^{n}\left(x_i - \bar{x}\right)\left(y_i - \bar{y}\right)}{\sqrt{\sum_{i=1}^{n}(x_i - \bar{x})^2}\sqrt{\sum_{i=1}^{n}(y_i - \bar{y})^2}}, \tag{1}$$

where $\bar{x}$ and $\bar{y}$ are the mean values of X and Y, respectively. A value close to $+1$ indicates strong positive correlation, while 0 means no linear correlation.

2) Spearman Correlation The *Spearman correlation coefficient*, ρ_{Spearman}, measures *monotonic* relationships by ranking the values of each sample instead of using raw data. Each x_i and y_i is replaced by its rank R_{x_i} and R_{y_i}. Then,

$$\rho_{\text{Spearman}}(X,Y) = 1 - \frac{6\sum_{i=1}^{n}\left(R_{x_i} - R_{y_i}\right)^2}{n\left(n^2 - 1\right)} \tag{2}$$

This approach is more robust to outliers or nonlinearities than Pearson correlation.

3) Kendall's Tau Another rank-based method is *Kendall's tau*, τ_{Kendall}, which focuses on the count of *concordant* versus *discordant* pairs among the data points. It is defined as:

$$\tau_{\text{Kendall}}(X,Y) = \frac{(\#\text{ of concordant pairs}) - (\#of discordant pairs)}{\frac{1}{2}n\left(n-1\right)} \tag{3}$$

Like Spearman, Kendall's tau is nonparametric and can handle nonlinear relationships gracefully.

4) Cross-Correlation (Raw) For time-series data, the *cross-correlation function* $R_{xy}(\tau)$ measures how similar X and Y are when shifted by a lag τ. In discrete form, the raw cross-correlation can be expressed as:

$$R_{xy}(\tau) = \sum_{t=1}^{n} x_t\, y_{t+\tau} \tag{4}$$

where τ can vary in a range $[-T, +T]$. This is useful when phase shifts or delays exist between signals.

5) Normalized Cross-Correlation Since raw cross-correlation depends on signal magnitudes and lengths, a *normalized cross-correlation* (NCC) is often preferred. One common form is:

$$R_{xy}^{(\text{norm})}(\tau) = \frac{\sum_{t=1}^{n}(x_t - \bar{x})(y_{t+\tau} - \bar{y})}{\sqrt{\sum_{t=1}^{n}(x_t - \bar{x})^2}\sqrt{\sum_{t=1}^{n}(y_{t+\tau} - \bar{y})^2}}, \tag{5}$$

which yields values in $[-1, 1]$, with $+1$ indicating a perfect match.

As Steps:

- Compute the chosen correlation measure for each ROI vs. the center signal.
- Identify the ROI(s) with the highest correlation value(s) (e.g., Pearson $\rho > 0.85$ or an XCrossNorm close to $+1$).
- Mark the top-correlated ROI(s) as potential leak zones.

Multiple correlation metrics are employed to guarantee detection of subtle leaks that may be obscured by nonlinear effects. This correlation-driven methodology exploits the periodic nature of respiration, enabling precise localization by matching each ROI's signal to the reference respiratory pattern extracted from the mask's central region.

4.2. Human Participants (Validation Protocol)

After validating of the detection and localization approaches with static heads experiments under controlled conditions, the study extended to the methodology to actual human participants to assess its robustness in more realistic scenarios; Figure 8 shows an example of the dataset collected. Human subjects naturally introduce additional variability due to head movements, differing facial structures, and individual breathing patterns.

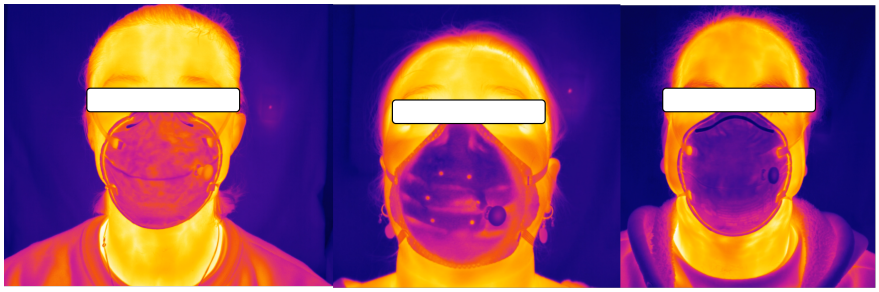

Figure 8: Human Participants dataset example

Mask Segmentation and Contour Extraction: To handle the dynamic conditions presented by human participants, we adopted a dual segmentation strategy that integrates variant custom U-Net model, developed in by our Team Mohamed Arbane and Maldague (2024), with the Segment Anything Model 2 (SAM2). This approach ensures accurate and reliable mask contour tracking even as participants move naturally during the experiments.

Initial Segmentation with Custom U-Net: The first frame of each video sequence is segmented using a U-Net variant tailored for N95 mask detection in infrared (IR) images, incorporating architectural enhancements that optimize performance in thermal imaging contexts Mohamed Arbane and Maldague (2024). This model isolates the N95 mask from the background, yielding a precise contour for the initial frame. The mask's center point is then computed from this contour and provided as the critical input for subsequent SAM2 segmentation.

Dynamic Segmentation with SAM2: Using the center point derived from the initial U-Net segmentation, the prompt SAM2 to perform segmentation on each subsequent frame. SAM2 is a state-of-the-art image segmentation model renowned for its ability to handle a variety of segmentation tasks with minimal user input. It employs a robust transformer-based architecture that efficiently generates high-quality segmentation masks, even in complex and

variable image environments. By providing SAM2 with the center point as a prompt, the model can dynamically track and segment the mask contour in real-time, adapting to any movements or adjustments made by the participant.

As illustrated in Figure 9 and Figure 10, the segmentation process involves the following steps:

1. **Initial Segmentation:** The custom U-Net segments the first frame to isolate the mask and calculate its center point.
2. **Prompt Generation:** The center point is used as a prompt for SAM2 to guide the segmentation in subsequent frames.
3. **Dynamic Tracking:** SAM2 processes each new frame, leveraging the prompt to maintain accurate segmentation of the mask contour despite head movements.

This dual-model strategy ensures that the mask contour remains consistently defined across all frames, providing a stable foundation for subsequent leak detection and localization.

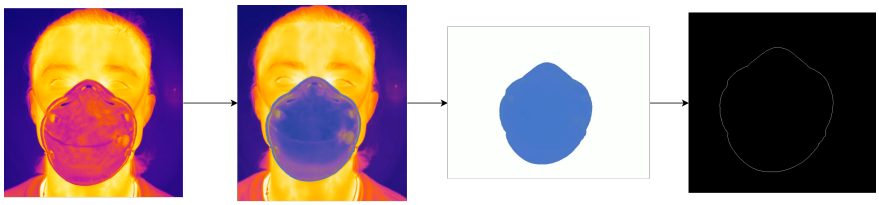

Figure 9: Segmentation Process using SAM2 and U-Net

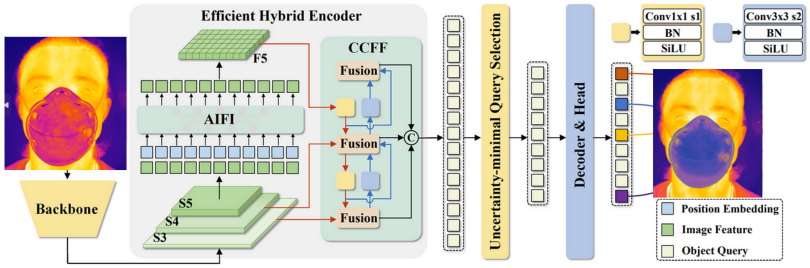

Figure 10: SAM2 Segmentation Architecture

Contour ROIs and Frequency Analysis: After extracting the mask contour, it is subdivided into 100 equal-sized Regions of Interest (ROIs) in each frame, following the protocol established in the mannequin experiments. Temperature signals for each ROI are recorded over time and transformed into the frequency domain using the Fast Fourier Transform (FFT). The resulting spectrogram reveals thermal fluctuations corresponding to the subject's breathing cycle.

Correlation-Based Leak Localization: Extending the methodology from the previous subsection, each ROI's frequency signal is correlated with that of the mask's centre. The centre region provides the reference for the wearer's normal respiratory pattern. ROIs demonstrating strong correlation to this reference frequency are marked as potential leak sites. Employing the correlation procedure detailed in Section 4.1.2 enables precise localization of leaks along the contour, even when the participant's head moves.

5. Experiments and Results

5.1. Overview of Metrics and Evaluation Protocol

5.1.1. Experimental Metrics

This subsection defines the quantitative metrics and evaluation procedures for assessing both leak classification performance and correlation-based localization accuracy.

Leak Classification Metrics For the binary classification task (*leak* vs. *no leak*), precision, recall, and the F1 score were employed:

- **Precision** (P): The ratio of correctly identified leaks (true positives) to all predicted leaks (true positives + false positives).

$$P = \frac{TP}{TP + FP}$$

- **Recall** (R): The ratio of correctly identified leaks to all actual leaks (true positives + false negatives).

$$R = \frac{TP}{TP + FN}$$

- **F1 Score**: The harmonic mean of precision and recall, providing a balanced metric when both false positives and false negatives are critical.

$$F1 = 2 \times \frac{P \times R}{P + R}$$

These metrics capture how effectively the proposed ResNet-SVM pipeline distinguishes between leak and no-leak conditions for the controlled mannequin tests.

Correlation Thresholds for Localization : Once a segment is classified as *leak*, the correlation-based methodology localizes the exact leak site by comparing each ROI's frequency-domain signal to the reference breathing signal from the mask's center. In the *controlled (mannequin) environment*, we apply a stricter threshold of 95% for all correlations (e.g., Pearson's $\rho > 0.95$) to label an ROI as a *true leak*. By contrast, in *human participant trials*, where movement and facial variability introduce additional noise, the acceptable threshold is set lower: for Pearson correlation, a coefficient above 0.85 indicates a likely leak, and for normalized cross-correlation (XCorrNorm), a value exceeding 0.77 suggests a valid leak. These empirically chosen cutoffs balance the need to minimize false alarms with the goal of reliably identifying subtle but significant leaks.

Evaluation Protocol : A transfer learning approach was employed using ResNet50, originally pre-trained on the ImageNet dataset of over two million images. The network's final two layers were replaced with a binary Support Vector Machine (SVM) classification block. Specifically, ResNet50's convolutional body functioned as a high-level feature extractor, and the resulting feature vectors were passed to the SVM to perform leak versus no-leak classification.

A default binary configuration was employed for the SVM, incorporating a Radial Basis Function (RBF) kernel, a penalty parameter $C = 1.0$, and gamma set to `scale`. These hyperparameters balance model complexity and generalization, enabling effective separation of leak and no-leak feature distributions. The controlled-environment dataset comprised 98 test scenarios, with 70% allocated for training and the remaining 30% reserved for testing and validation. Cross-validation on the mannequin datasets was performed during training to fine-tune the decision boundary. The integration of ResNet50's deep feature extraction with SVM classification demonstrated robustness despite limited training samples and variations in thermal signatures.

5.2. Mannequin (Controlled Environment) Results:

In the controlled environment experiments, the comparison of the proposed classification approach against a state-of-the-art method presented by Darius et al. Chapman, Strong, Tiver, Dharmaprani, Jenkins and Ganesan (2023). To ensure a fair comparison, we re-implemented Darius et al.'s methodology from scratch using the same IR dataset collected in our mannequin setup. Both techniques were evaluated on the identical training and testing splits, allowing us to assess their relative performance under consistent conditions.

Table 3 summarizes the classification results—precision, recall, and F1-score—for both our ResNet50+SVM pipeline and the model described by Chaplan et al. in Chapman et al. (2023), highlighting key differences and advantages. Unlike the reference approach, which relies on manual ROI selection and single-image inputs processed using normalization and Gray-Level Co-occurrence Matrix (GLCM) features, our framework fully automates ROI generation and processes temporal sequences of thermal frames. By leveraging thermal data across multiple time

Test Number	Leak Info	FF_Average	Number of Leaks	Classification Model (Leaks/Non-leaks)	Leak ROIS	Correlation ROIS > 95%
1	[4,5,8G]	42.6	1	Leak	5	5-6-7-4-3
2	[2,1,8G]	47.8	1	Leak	11	71-70-72-69
3	[2,4,8G]	42.2	1	Leak	59	59-58-60-57
4	[4,1,12G]	127.8	1	Leak	19	
5	[2,2,12G]	120	1	Leak	67	67-68-65-66
6	[4,4,12G]	99.6	1	Leak	8	8-7-3-5-4
50	[3,3,8G]	55.6	1	Leak	36	35-36-34
51	[4,2,12G]	91	1	Leak	11	11-10-12
52	[3,2,15G]	176.8	1	Leak	64	64-62-61
53	[3,4,14G]	130.8	1	Leak	31	32-31-33
54	[4,2,10G]	80.8	1	Leak	15	15-16-14-13
57	[2,5,16G]	200	1	Leak	55	
70	[1,4,10G] + [4,4,10G]	41.6	2	Leak	84(1,4)-8(4,4)	84-83-85-8-9
71	[2,2,12G] + [3,3,8G]	26.8	2	Leak	35(3,3),68(2,2)	35-36-68
72	[3,4,12G] + [4,2,14G]	90.2	2	Leak	14(4,2)-32(3,4)	14-13-32-33
73	[2,1,14G] + [3,5,16G]	138.4	2	Leak	27(3,5)-71(2,1)	71-72-68
75	[2,4,16G] + [3,1,12G]	106.6	2	Leak	43(2,4)-59(3,1)	43-42-44-59
76	[1,3,10G] + [3,2,12G]	69.6	2	Leak	87-36	87-88-90-91
77	[1,2,12G] + [1,4,12G] + [3,4,14G]	52.8	3	Leak	9(1,2)-14(1,4)-31(3,4)	8-9-87-91
88	[2,2,8G]+[3,3,10G]+[4,4,12G]	27.4	3	Leak	8(4,4)-35(3,3)-68(2,2)	68-65-36-85
89	[1,1,8G]+[4,3,8G]+[3,4,8G]	18.2	3	Leak	11(4,3)-31(3,4)-94(1,1)	31-94-93-11-32-92-10

Table 2
Mannequin controlled environment Tests Results with Leak Classification and correlation methods

Table 3
Comparison between state-art-model and proposed method.

Metric	Chapman et al. (2023) Method	Our Method
Region of Interest (ROI)	manual	automatic
Input Type	1 image	sequence
Input Category	image	signal
Preprocessing	Normalization + GLCM	ResNet 50
Classification Method	SVM	SVM
Precision	0.92	0.98
Recall	0.95	0.96
F1 Score	0.93	0.97

steps and a deep transfer-learning pipeline based on ResNet50 to distill complex spatiotemporal patterns into high-level feature representations, our method more comprehensively captures breathing-cycle dynamics. Although both approaches employ SVM classifiers, the shift from manual to automatic ROI selection and from single-frame to sequence-based inputs yields superior robustness against minor variations in leak size and contour segmentation, resulting in higher accuracy, recall, and F1-score. This evaluation not only validates the effectiveness of our proposed methodology but also provides a direct comparison against an established benchmark in N95 mask leak detection.

5.3. Human Participants Results

This subsection presents the performance of the proposed leak detection and localization methodology on data collected from human participants. Figures 9 and 10 illustrate the dynamic isolation of the N95 mask contour in each frame using SAM2 in conjunction with a custom U-Net model, effectively accommodating natural head movements and facial variability. Following segmentation, the correlation-based localization algorithm—previously validated in controlled mannequin experiments—was applied to identify leak sources by matching local infrared signal patterns to the respiratory frequency. Table 4 reports IR imaging results for two participants exhibiting markedly different Fit Factors (FF). The FF is defined as the ratio of ambient particle concentration to that inside the respirator during a quantitative fit test. An FF of 200 indicates that interior particle concentration is just 1/200th of the exterior—equivalent to an essentially airtight seal far above the OSHA minimum of 100 for half-face respirators. By contrast, an FF of 3.5 corresponds to approximately 29 % leakage, signifying a very poor seal. In Table 4, the left column lists the top

Table 4
Correlated ROIs by Pearson Correlation for Two Participants with Different Fit Factors

Participant N35 (FF=3.5)

ROI Index	Correlation
13	0.9980
3	0.9979
11	0.9977
0	0.9976
10	0.9974
12	0.9969
4	0.9946
96	0.9912
2	0.9896
15	0.9860

Participant N25 (FF=200)

ROI Index	Correlation
0	0.9744
2	0.9079
40	0.8176
19	0.7651
49	0.7466
59	0.7204
46	0.7080
98	0.6915
5	0.6814
4	0.6739

correlated regions of interest (ROIs) for the FF = 3.5 subject—revealing multiple leak points scattered along the mask contour—while the right column presents the FF = 200 subject's ROIs, which show fewer and lower correlation values.

Tables.5 to 11 provide a detailed analysis of the correlation coefficients and cross-correlation metrics for various ROI Index across multiple participants wearing N95 masks. These tables highlight the differences in leak localization accuracy by comparing Pearson, Spearman, and Kendall correlation metrics, as well as raw and normalized cross-correlation values. Participants with higher Fit Factors (e.g., FF=200) demonstrate fewer and weaker correlations in ROIs, indicative of minimal leakage, while those with lower Fit Factors (e.g., FF=3.5) exhibit multiple high-correlation ROIs, confirming significant leaks. This data underscores the robustness of the proposed methodology in distinguishing varying levels of mask leakage across different individuals, further validating its applicability under real-world conditions.

6. Comparative Analysis and Results Discussion

The results presented in the preceding sections highlight both the effectiveness and versatility of our proposed N95 mask leak detection and localization framework. By comparing our method with existing state-of-the-art approaches and examining its performance across a range of test conditions—spanning controlled mannequin experiments to real human participants—we can draw several meaningful conclusions.

6.1. Comparative Analysis

In controlled environments, our ResNet50+SVM classification pipeline outperforms previously established methods, such as the approach described by Darius et al. Chapman et al. (2023), in terms of precision, recall, and F1 score. As shown in Table 3, our method achieves a precision of 0.98 and an F1 score of 0.97, substantially improving upon the 0.92 precision and 0.936 F1 score reported by the state-of-the-art baseline. This improvement can be attributed to our use of deep feature extraction via ResNet50 and the adoption of sequence-based signal inputs rather than single static images. By analyzing multiple frames, our system captures temporal variations in thermal signatures associated with breathing, enabling more robust detection of subtle leaks that might be overlooked by methods relying on single-frame analysis.

Another key advantage of our approach lies in the automatic ROI selection. While Chapman et al. (2023) and other conventional methods often rely on manual ROI definition or simple image-based analysis, our method leverages dynamic segmentation and correlation-based localization to pinpoint leaks without human intervention. This transition from manual to automatic ROI identification, combined with our sequence-based, signal-level analysis, ensures a richer and more context-aware representation of the thermal data. Consequently, we achieve better generalization and adaptability to variations in mask fit conditions and environmental factors.

Also, Pearson and cross-correlation methods demonstrated superior performance on human participants results accurately localizing mask leaks compared to other approaches in. These methods provided robust correlation metrics,

effectively identifying regions of interest (ROIs) with significant leakage, as highlighted in the results tables. Pearson correlation, with its sensitivity to linear relationships, and cross-correlation, with its ability to analyze temporal shifts, offered precise alignment of respiratory frequency patterns between the mask's center and its contour. This advantage arises from their ability to capture subtle periodic variations in thermal signals, which are often missed by less sensitive metrics such as Spearman or Kendall correlations. These findings underscore the reliability of Pearson and cross-correlation as tools for dynamic, real-time leak localization.

6.2. Results Discussion

The results presented in this study demonstrate the effectiveness and robustness of the proposed framework for N95 mask leak detection and localization under both controlled and real-world scenarios. The comparative performance analysis between our method and existing state-of-the-art approaches highlights several key findings.

6.2.1. Controlled Environment Performance:

The ResNet50+SVM classification pipeline achieved superior precision, recall, and F1 scores compared to existing methods. By leveraging temporal patterns in thermal data and employing dynamic segmentation, the proposed approach addressed limitations of single-frame, static analysis techniques. The use of FFT-generated spectrograms for feature extraction played a critical role in improving classification accuracy, particularly in detecting subtle leaks missed by traditional methods.

6.2.2. Real-World Validation with Human Participants:

The performance of the framework on human participant trials underscores its adaptability and robustness in dynamic, real-world settings. As detailed in Tables 5 to 11, Pearson and cross-correlation coefficients consistently identified ROIs associated with leakage, even under variable conditions such as facial movements and mask adjustments. For instance, participants with low Fit Factors (e.g., Participant N35 FF=3.5 in Table 4) exhibited multiple high-correlation ROIs, indicative of significant leakage. Conversely, participants with higher Fit Factors (e.g., Participant N25 FF=200 in Table 4) demonstrated minimal high-correlation ROIs, confirming secure mask fit. These results validate the system's ability to distinguish between varying leakage levels effectively.

6.2.3. Superiority of Correlation Methods:

The superior performance of Pearson and cross-correlation methods for leak localization, as evidenced by Tables 5 to 11, can be attributed to their sensitivity to both linear relationships and temporal alignment of respiratory signals. Pearson correlation excels in capturing the strength of linear associations between thermal signals at the mask's center and contour, while cross-correlation accounts for any temporal shifts, providing robust localization even in dynamic scenarios. Compared to alternative metrics like Spearman or Kendall correlations, these methods yielded consistently higher localization accuracy across all test cases.

6.2.4. Challenges and Future Directions:

While the results are promising, certain challenges remain. Variability in thermal signatures due to environmental factors, such as room temperature or humidity, could affect accuracy. Additionally, the need for high-resolution infrared cameras may limit deployment in low-resource settings. Future research should explore integrating adaptive thresholding techniques and optimizing the pipeline for edge-device compatibility. Incorporating privacy-preserving methodologies, such as federated learning, will also enhance the system's utility in sensitive healthcare environments.

6.2.5. Conclusion:

In conclusion, the results highlight the transformative potential of combining infrared imaging with advanced AI techniques for dynamic, real-time N95 mask leak detection and localization. The proposed framework not only outperforms existing approaches but also demonstrates scalability, robustness, and adaptability, paving the way for safer and more efficient use of respiratory protection devices.

References

, . FLIR X8501sc Infrared Camera. FLIR Systems, Inc. Wilsonville, Oregon, USA. URL: https://doc.bcbingenieria.com/DOCS/Anexos_web/FLIR/A4/Individuales/X8xxx/29422-201-en-US_A4_X8501sc.pdf. datasheet.

Chapman, D., Strong, C., Tiver, K.D., Dharmaprani, D., Jenkins, E., Ganesan, A.N., 2023. Infra-red imaging to detect respirator leak in healthcare workers during fit-testing clinic. IEEE Open Journal of Engineering in Medicine and Biology .

Participant N29 (FF=15)(Mask type =NBW95)

ROI Index	Pearson	Spearman	Kendall	XCorrRaw	XCorrNorm
0	0.945111	0.532754	0.393939	3.722976e+06	0.909183
1	0.941581	0.573195	0.465909	3.377113e+06	0.888773
65	0.918343	0.319853	0.223485	4.294721e+06	0.817713
2	0.905084	0.454545	0.348485	8.998165e+06	0.848883
15	0.894748	0.227273	0.155303	1.818099e+06	0.753135
12	0.868592	0.037099	0.018939	3.081628e+06	0.770416
64	0.867995	0.026070	0.022727	3.442209e+06	0.740022
13	0.857293	0.172126	0.113636	2.287423e+06	0.725963

Table 5
Correlation coefficients and cross-correlation metrics for participant N29 with a Fit Factor (FF) of 15, highlighting significant leak-prone regions.

Participant N11 (FF=104)(Mask type =8210)

ROI Index	Pearson	Spearman	Kendall	XCorrRaw	XCorrNorm
65	0.987955	0.396390	0.284091	2.949508e+06	0.958878
56	0.983454	0.309158	0.227273	5.519881e+06	0.933662
66	0.981587	0.252340	0.178030	3.012380e+06	0.954436
68	0.981295	0.225936	0.151515	2.662433e+06	0.940199
62	0.979555	0.000668	-0.034091	2.827786e+06	0.931047
67	0.975056	0.048128	0.022727	2.001427e+06	0.921787
74	0.974163	0.315842	0.238636	5.040858e+06	0.931695
69	0.972939	0.099933	0.045455	1.927258e+06	0.908513
63	0.970596	-0.043115	-0.045455	2.095600e+06	0.909488

Table 6
Correlation coefficients and cross-correlation metrics for participant N11 with a Fit Factor (FF) of 104, demonstrating moderate leak localization results.

Chapman, D., Strong, C., Tiver, K.D., Dharmaprani, D., Jenkins, E., Ganesan, A.N., 2024. Infra-red imaging to detect respirator leak in healthcare workers during fit-testing clinic. IEEE Open J. Eng. Med. Biol. 5, 198–204. doi:10.1109/OJEMB.2023.3330292.

Derrick, J.L., Chan, Y.F., Gomersall, C.D., Lui, S.F., 2005. Predictive value of the user seal check in determining half-face respirator fit. J. Hosp. Infect. 59, 152–155. doi:10.1016/j.jhin.2004.09.012.

Harber, P., Su, J., Badilla, A.D., Rahimian, R., Lansey, K.R., 2015. Potential role of infrared imaging for detecting facial seal leaks in filtering facepiece respirator users. J. Occup. Environ. Hyg. 12, 369–375. doi:10.1080/15459624.2015.1006636.

Hariharan, P., Sharma, N., Guha, S., Banerjee, R.K., D'Souza, G., Myers, M.R., 2021. A computational model for predicting changes in infection dynamics due to leakage through n95 respirators. Scientific reports 11, 10690.

Hinds, W.C., Bellin, P.P., 1987. Performance of dust respirators with facial seal leaks: II. Predictive model. Am. Ind. Hyg. Assoc. J. 48, 842–847. doi:10.1080/15298668791385688.

Kerl, J., Wenzel, M., Köhler, D., . Thermal imaging of mask leakage during pressure-controlled ventilation (BIPAP therapy), journal = Somnologie, volume = 8, number = 3, pages = 83–86, year = 2004, doi = 10.1111/j.1439-054X.2004.04021.x .

Kim, H., Kim, T.M., Choi, S.W., Ko, T., 2024. Thermal imaging and deep learning-based fit-checking for respiratory protection. Scientific Reports 14, 24407. doi:10.1038/s41598-024-52999-0.

Koonce, B., Koonce, B., 2021. Resnet 50. Convolutional neural networks with swift for tensorflow: image recognition and dataset categorization , 63–72.

Koroteeva, E., Shagiyanova, A., 2022. Infrared-based visualization of exhalation flows while wearing protective face masks. Physics of Fluids 34.

Lam, S.C., Odetayo, A., Yu, I.T.S., So, S.N.Y., Cheung, K., Lee, P.H., Suen, L.K.P., 2023. Evaluation of n95 respirators on fit rate, real-time leakage, and usability among chinese healthcare workers: study protocol of a randomized crossover trial. Frontiers in public health 11, 1266607.

Lee, S., Grinshpun, S.A., Reponen, T., 2008. Respiratory performance offered by N95 respirators and surgical masks: human subject evaluation with NaCl aerosol under the condition of speech and movement. Ann. Occup. Hyg. 52, 385–396. doi:10.1093/annhyg/men005.

Participant N02 (FF=46)(Mask type =2200)

ROI Index	Pearson	Spearman	Kendall	XCorrRaw	XCorrNorm
75	0.898376	0.229947	0.143939	4.470559e+05	0.813694
72	0.863811	0.454880	0.371212	9.922068e+05	0.758059
64	0.860069	0.413770	0.306818	2.051064e+06	0.748534
76	0.857835	0.151070	0.113636	3.941923e+05	0.769121
33	0.853291	0.501671	0.378788	2.766135e+05	0.730224
18	0.847312	0.253342	0.166667	2.048876e+06	0.712474
79	0.845305	0.020388	0.003788	4.889984e+05	0.726428
78	0.837361	-0.040775	-0.034091	4.953883e+05	0.751935

Table 7
Correlation coefficients and cross-correlation metrics for participant N02 with a Fit Factor (FF) of 46, showing moderate leakage patterns.

Participant N02 (FF=166.5)(Mask type =8210)

ROI Index	Pearson	Spearman	Kendall	XCorrRaw	XCorrNorm
2	0.965909	0.362968	0.280303	1.295872e+07	0.919178
46	0.955911	0.190508	0.147727	7.795891e+06	0.867172
23	0.948865	0.245989	0.185606	1.471515e+07	0.847284
20	0.947193	0.027741	0.011364	3.514076e+06	0.829293
99	0.939387	0.466578	0.348485	8.493765e+06	0.859286
21	0.936898	0.356618	0.242424	5.079302e+06	0.849819
0	0.931921	0.565174	0.428030	1.853046e+07	0.884924
1	0.919542	0.427139	0.303030	2.350199e+07	0.902349
24	0.915613	0.358957	0.272727	1.456185e+07	0.821336

Table 8
Correlation coefficients and cross-correlation metrics for participant N02 with a Fit Factor (FF) of 166.5, indicating minimal mask leakage.

Lei, Z., Yang, J., Zhuang, Z., Roberge, R.R., 2013. Simulation and evaluation of respirator faceseal leaks using computational fluid dynamics and infrared imaging. Ann. Occup. Hyg. 57, 493–506. doi:10.1093/annhyg/mes085.

Liu, B.Y.H., Lee, J.K., Mullins, H., Danisch, S.G., 1993. Respirator leak detection by ultrafine aerosols: a predictive model and experimental study. Aerosol Sci. Technol. 19, 15–26. doi:10.1080/02786829308959611.

Marchais, G., Arbane, M., Topilko, B., Brousseau, J., Brochot, C., Yaddaden, Y., Bahloul, A., Maldague, X., 2024a. Saferespirator: Comprehensive database for n95 filtering facepiece respirator leak detection including infrared, rgb videos, and quantitative fit testing. IEEE Access .

Marchais, G., Topilko, B., Arbane, M., Brousseau, J., Brochot, C., Yaddaden, Y., Bahloul, A., Maldague, X., 2024b. A test bench for replicating human breathing: Evaluating thermal effects of n95 filtering facepiece respirator leaks – preliminary findings, in: 2024 9th International Conference on Computer Science and Engineering (UBMK), pp. 695–700. doi:10.1109/UBMK63289.2024.10773589.

Mohamed Arbane, Geoffrey Marchais, B.T.Y.Y.J.B.C.B.A.B., Maldague, X., 2024. Advanced infrared face mask segmentation using a custom lightweight u-net model. IEEE International Multi-Conference on Smart Systems and Green Process .

Oestenstad, R.K., Bartolucci, A.A., 2010. Factors affecting the location and shape of face seal leak sites on half-mask respirators. J. Occup. Environ. Hyg. 7, 332–341. doi:10.1080/15459621003729909.

O'Kelly, E., Arora, A., Pirog, S., Ward, J., Clarkson, P.J., 2021. Comparing the fit of N95, KN95, surgical, and cloth face masks and assessing the accuracy of fit checking. PLoS One 16, e0245688. doi:10.1371/journal.pone.0245688.

Roberge, R.J., Monaghan, W.D., Palmiero, A.J., Shaffer, R.E., Bergman, M.S., 2011. Infrared imaging for leak detection of N95 filtering facepiece respirators: a pilot study. Am. J. Ind. Med. 54, 628–636. doi:10.1002/ajim.20970.

Safdar, M.F., Nowak, R.M., Pałka, P., 2022. A denoising and fourier transformation-based spectrograms in ecg classification using convolutional neural network. Sensors 22, 9576.

Schmitt, J., Wang, J., 2022. A critical review on the role of leakages in the facemask protection against sars-cov-2 infection with consideration of vaccination and virus variants. Indoor air 32, e13127.

Participant N22 (FF=59)(Mask type =2200)

ROI Index	Pearson	Spearman	Kendall	XCorrRaw	XCorrNorm
0	0.960858	0.459559	0.352273	6.820461e+06	0.835353
32	0.893373	0.475602	0.356061	9.964524e+06	0.819186
9	0.822569	0.304813	0.219697	2.303108e+06	0.677668
1	0.820364	0.432487	0.314394	3.277450e+06	0.717071
7	0.789656	0.295120	0.212121	3.484852e+06	0.647844
65	0.772441	0.556484	0.416667	3.958739e+06	0.611516
11	0.766470	0.288436	0.200758	3.945222e+06	0.683421
3	0.766022	0.548797	0.420455	3.420067e+06	0.627430
10	0.744012	0.507019	0.371212	3.149983e+06	0.651270

Table 9
Correlation coefficients and cross-correlation metrics for participant N22 with a Fit Factor (FF) of 59, illustrating regions with varying leakage levels.

Participant N29 (FF=15)(Mask type =NBW95)

ROI Index	Pearson	Spearman	Kendall	XCorrRaw	XCorrNorm
0	0.945111	0.532754	0.393939	3.722976e+06	0.909183
1	0.941581	0.573195	0.465909	3.377113e+06	0.888773
65	0.918343	0.319853	0.223485	4.294721e+06	0.817713
2	0.905084	0.454545	0.348485	8.998165e+06	0.848883
15	0.894748	0.227273	0.155303	1.818099e+06	0.753135
12	0.868592	0.037099	0.018939	3.081628e+06	0.770416
64	0.867995	0.026070	0.022727	3.442209e+06	0.740022
13	0.857293	0.172126	0.113636	2.287423e+06	0.725963
14	0.850041	0.209559	0.155303	1.756089e+06	0.700833

Table 10
Correlation coefficients and cross-correlation metrics for participant N29 with a Fit Factor (FF) of 15, highlighting multiple leak-prone regions.

Siah, C.J.R., Lau, S.T., Tng, S.S., Chua, C.H.M., 2022. Using infrared imaging and deep learning in fit-checking of respiratory protective devices among healthcare professionals. J. Nurs. Scholarsh. 54, 345–354. doi:10.1111/jnu.12736.

Staymates, M., 2020. Flow visualization of an N95 respirator with and without an exhalation valve using schlieren imaging and light scattering. Phys. Fluids 32, 111703. doi:10.1063/5.0031996.

Tanışalı, G., Sozak, A., Bulut, A.S., Sander, T.Z., Özlem Doğan, Çağdaş Dağ, Gönen, M., Can, F., DeMirci, H., Önder Ergonul, 2021. Effectiveness of different types of mask in aerosol dispersion in SARS-CoV-2 infection. Int. J. Infect. Dis. 109, 310–314. doi:10.1016/j.ijid.2021.06.029.

Verma, S., Dhanak, M., Frankenfield, J., 2020a. Visualizing droplet dispersal for face shields and masks with exhalation valves. Phys. Fluids 32, 091701. doi:10.1063/5.0024291.

Verma, S., Dhanak, M., Frankenfield, J., 2020b. Visualizing the effectiveness of face masks in obstructing respiratory jets. Phys. Fluids 32, 061708. doi:10.1063/5.0016018.

Viscusi, D.J., Bergman, M.S., Zhuang, Z., Shaffer, R.E., 2012. Evaluation of the benefit of the user seal check on N95 filtering facepiece respirator fit. J. Occup. Environ. Hyg. 9, 408–416. doi:10.1080/15459624.2012.686227.

Wang, T., Solano, T., Shoele, K., 2022. Bridge the gap: correlate face mask leakage and facial features with 3D morphable face models. J. Expo. Sci. Environ. Epidemiol. 32, 735–743. doi:10.1038/s41370-021-00399-1.

Participant N33 (FF=200)(Mask type =8210)

ROI Index	Pearson	Spearman	Kendall	XCorrRaw	XCorrNorm
0	0.945111	0.532754	0.393939	3.722976e+06	0.909183
1	0.941581	0.573195	0.465909	3.377113e+06	0.888773
65	0.918343	0.319853	0.223485	4.294721e+06	0.817713
2	0.905084	0.454545	0.348485	8.998165e+06	0.848883
15	0.894748	0.227273	0.155303	1.818099e+06	0.753135
12	0.868592	0.037099	0.018939	3.081628e+06	0.770416
64	0.867995	0.026070	0.022727	3.442209e+06	0.740022
13	0.857293	0.172126	0.113636	2.287423e+06	0.725963
14	0.850041	0.209559	0.155303	1.756089e+06	0.700833

Table 11
Correlation coefficients and cross-correlation metrics for participant N33 with a Fit Factor (FF) of 200, confirming secure mask fit with minimal leakage.

Chapitre 6

Conclusion générale

Cette recherche visait à développer une méthodologie innovante pour la détection et la localisation en temps réel des fuites dans les PFF N95, combinant efficacement l'imagerie infrarouge (IR) avec des approches avancées d'apprentissage profond. Ce projet a permis d'atteindre les objectifs fixés en proposant un cadre robuste capable de surmonter les limites des méthodes conventionnelles actuelles, souvent coûteux, invasifs et incapables de fournir une surveillance continue.

La solution proposée repose sur plusieurs contributions méthodologiques importantes. Premièrement, une segmentation dynamique précise du contour du PFF a été réalisée à l'aide d'un modèle U-Net optimisé combiné au Segment Anything Model 2 (SAM2), permettant un suivi efficace et fiable malgré les mouvements naturels et les fluctuations thermiques. Deuxièmement, une méthode de classification hybride basée sur l'architecture ResNet50 et un classifieur à vecteurs de support (SVM) a été développée pour identifier clairement les états de fuite et de non-fuite avec une précision remarquable. Troisièmement, une approche de localisation basée sur l'analyse de la corrélation spectrale entre la signature thermique respiratoire centrale et les signaux thermiques périphériques segmentés a été mise au point, permettant une localisation rapide et précise des

points de fuite.

Les performances du système ont été rigoureusement validées sur plusieurs plateformes : surfaces planes, mannequins respiratoires instrumentés et tests sur des participants humains dans des conditions réelles d'utilisation (variations de mouvements et d'environnement). Cette validation extensive a confirmé la robustesse, la précision et la rapidité du système, démontrant un taux de détection des fuites supérieur de recherches précédentes et un temps de localisation inférieur à une seconde.

6.1 Objectifs accomplis

Ce mémoire examine la détection et la localisation des fuites des PFF N95 en s'appuyant sur l'analyse de plusieurs études, chacune mettant l'accent sur un aspect particulier :

- ✓ article Conférence IEEE qui a été introduction d'une méthode de segmentation qui isole le contour du PFF dans chaque image d'une séquence de thermographie infrarouge afin d'éliminer les biais et de permettre une analyse précise des zones de fuite.
- ✓ le deuxième article de la conférence de l'IEEE qui a été l'amélioration de la chaîne de segmentation par l'intégration de SAM2 pour une approche plus rapide et dynamiquement adaptative, capable de segmenter le PFF sur l'ensemble de la séquence, de définir une région d'intérêt personnalisée autour du contour, et d'appliquer des analyses de corrélation pour identifier les signaux imitant les schémas respiratoires selon diverses méthodes analytiques.

- ✓ Le troisième article a été soumis à la revue Infrared Physics & Technology. qui présente une application du modèle de l'article 2 pour extraire la région d'intérêt, utilisation de plusieurs méthodes de corrélation (y compris la comparaison avec Pourtacont) pour une validation rigoureuse des résultats, et mise en place d'un cadre de classification pour détecter automatiquement la présence ou l'absence de fuites.
- ✓ **Annexe A :** Développement du protocole de constitution de base de données : notre équipe a défini les procédures de capture de séquences synchronisées en RGB-visuel et en thermographie infrarouge , ma contribution a consisté à calibrer la caméra RGB avec la caméra thermographique, synchroniser leurs enregistrements pour permettre des analyses intermodales des régions au-delà du contour du PFF et analyse de la région autour du visage à l'aide de points de repère autour du visage.
- ✓ **Annexe B :** Création d'une base de données en environnement contrôlé pour caractériser la nature des fuites et leur impact sur les zones adjacentes au PFF, mon rôle a consisté à participer à la conception du protocole expérimental et à analyser les données pour localiser précisément les fuites.

6.2 Limitations connues

Malgré les performances prometteuses obtenues, cette étude présente certaines limites importantes qui méritent d'être soulignées :

- × **Quantification des fuites :** le système développé permet actuellement de localiser précisément les fuites mais n'intègre pas de méthode quantifiée pour mesurer précisément le débit ou l'intensité des fuites, ce qui serait

essentiel pour des applications nécessitant des mesures quantitatives rigoureuses.

× **Variabilité environnementale :** la robustesse face aux variations rapides des conditions environnementales, comme les changements brusques de température ou d'humidité, demeure un défi.

× **Généralisation :** bien que le modèle ait été testé sur plusieurs types de PFF et participants, il serait bénéfique d'étendre les tests à une gamme encore plus large de modèles de PFF et d'environnements opérationnels variés pour assurer une généralisation complète du système.

6.3 Perspectives et travaux futurs

— Pour surmonter ces limites, plusieurs pistes d'amélioration et de travaux futurs sont envisagées.

— Premièrement, l'intégration d'algorithmes avancés pour la quantification précise des débits de fuite est essentielle et constituera une priorité pour les prochaines recherches.

— Deuxièmement, l'implémentation de réseaux neuronaux spatio-temporels compacts et efficaces pourrait permettre une meilleure gestion des dynamiques temporelles des fuites.

— Par ailleurs, il serait intéressant d'explorer des approches d'apprentissage automatique semi-supervisé et non supervisé pour améliorer la capacité du système à s'adapter aux nouvelles situations.

— Enfin, des essais cliniques étendus et diversifiés devraient être réalisés pour garantir l'efficacité et la fiabilité du système dans différents contextes opérationnels et promouvoir ainsi son adoption généralisée.

6.4 Retour d'expérience

Durant mon parcours de maîtrise à l'Université du Québec à Rimouski (UQAR), j'ai eu l'opportunité d'approfondir significativement mes connaissances dans les domaines de la thermographie et de la vision par ordinateur appliquée à l'imagerie thermique. Cette expérience académique m'a permis d'acquérir et de développer des compétences approfondies en apprentissage profond (deep learning), ainsi qu'en intelligence artificielle appliquée au traitement d'images.

Par ailleurs, j'ai eu le privilège de contribuer activement à plusieurs événements scientifiques reconnus. En effet, mes travaux ont été présentés dans plus de trois conférences internationales organisées par l'IEEE, ainsi que dans deux articles publiés dans des revues scientifiques renommées. Ces réalisations m'ont permis non seulement d'approfondir mes compétences techniques et scientifiques, mais également d'échanger avec une communauté internationale d'experts dans mon domaine.

Il est essentiel de souligner que ces contributions et cet apprentissage approfondi ont été largement facilités par le soutien constant de mes superviseurs, ainsi que par les échanges fructueux avec nos partenaires de recherche. Leur expertise et leur accompagnement ont joué un rôle déterminant tout au long de mon cheminement académique.

Enfin, les infrastructures et les installations mises à ma disposition par l'UQAR ont constitué un atout considérable, m'offrant les ressources nécessaires pour mener à bien mes recherches et atteindre les objectifs fixés. Cette expérience enrichissante restera un jalon essentiel dans mon parcours professionnel et personnel.

Concernant mes objectifs futurs, je compte poursuivre ma collaboration actuelle avec mon équipe de recherche en entamant un doctorat. Je suis impatient de relever les nouveaux défis que cette prochaine étape représente.

Annexe A

Titre :
SafeRespirator : Comprehensive Database for N95 Filtering Facepiece Respirator Leakage Detection Including Infrared, RGB Videos, and Quantitative Fit Testing

---

Résumé - *SafeRespirator est la première base de données à grande échelle combinant des vidéos infrarouges (640*512, 30 Hz) et RGB 4K synchronisées aux facteurs d'ajustement quantitatifs mesurés par PortaCount. 62 participants (36 femmes, 26 hommes) ont porté quatre modèles de N95 dans quatre orientations, produisant 1054 séquences IR, 1054 séquences RGB et 496 tests QNFT. Le dispositif caméras à 50 cm du visage, calibration thermo-optique au damier, synchronisation pulsée Arduino — enregistre 35s de respiration normale entre deux QNFT, dont 92,8% se révèlent fiables (FF1-FF2). Les premiers traitements appliquent le suivi facial MediaPipe (transféré du flux RGB vers IR), segmentent automatiquement le masque via un U-Net léger, puis recourent à une corrélation croisée normalisée entre la signature thermique centrale et les régions périphériques, atteignant des coefficients plus que 0,9 dans les zones fuyardes. Ces résultats valident la localisation et la quantification des fuites N95 en temps réel, ouvrant la voie à des systèmes de surveillance automatisés.*

Mots clés :
Base de données, Respirateur N95, Thermographie infrarouge, Vidéo RGB, Test d'ajustement quantitatif, Détection de fuites, Apprentissage profond, Santé et sécurité au travail

IEEE Access
Multidisciplinary ⋮ Rapid Review ⋮ Open Access Journal

Received 22 November 2024, accepted 17 December 2024, date of publication 25 December 2024, date of current version 9 January 2025.

Digital Object Identifier 10.1109/ACCESS.2024.3522562

RESEARCH ARTICLE

SafeRespirator: Comprehensive Database for N95 Filtering Facepiece Respirator Leakage Detection Including Infrared, RGB Videos, and Quantitative Fit Testing

GEOFFREY MARCHAIS[1], MOHAMED ARBANE[1], (Graduate Student Member, IEEE), BARTHELEMY TOPILKO[1], JEAN BROUSSEAU[1], CLOTHILDE BROCHOT[1,2], YACINE YADDADEN[1], ALI BAHLOUL[1,2], AND XAVIER MALDAGUE[3], (Life Senior Member, IEEE)

[1]Department of Mathematics, Computer Science, and Engineering, University of Quebec at Rimouski, Rimouski, QC G5L 3A1, Canada
[2]Institut de Recherche Robert-Sauvé en Santé et en Sécurité du Travail (IRSST), Montreal, QC H3A 3C2, Canada
[3]Department of Electrical and Computer Engineering, Laval University, Quebec City, QC G1V 0A6, Canada

Corresponding author: Geoffrey Marchais (geoffrey.marchais@uqar.ca)

This work was supported in part by the "Filtering Facepiece Respirator (FFR) Protective Devices—Development of an Easy-to-Use Method to Detect Leak and Assess Face Seal Tightness Using Infrared (IR) Imaging" Project which Institut de Recherche Robert-Sauvé en Santé et en Sécurité du Travail (IRSST) and Mitacs Fund under Grant IRSST 2022-0008, and in part by Mitacs under Grant IT37899.

This work involved human subjects or animals in its research. Approval of all ethical and experimental procedures and protocols was granted by the University of Quebec at Rimouski (UQAR) and Laval University Research Ethics Committees under Approval No. 2024-276. Date of Award: September 26, 2023.

ABSTRACT The COVID-19 pandemic underscored the challenges of performing mandatory Quantitative Fit Tests (QNFT) for healthcare professionals and the limitations of self-administered fit checks. To address this, it is crucial to develop faster and more efficient methods for detecting, locating, and quantifying Filtering Facepiece Respirators (FFRs) leakage, providing wearers with immediate feedback on their safety. Infrared (IR) technology, which relies on temperature variation analysis around the face seal, has proven effective for locating leakage but has not yet achieved automated quantification. This paper introduces a validated protocol for creating a comprehensive database to advance automatic leakage detection. The database includes synchronized and calibrated IR and RGB video data, along with QNFT results, collected from 62 participants wearing four different N95 FFR models in four distinct positions. High-performance IR and RGB cameras were used to precisely capture temperature variations, while a PortaCount® instrument served as the reference for fit quantification. Preliminary results using the MediaPipe approach with synchronized and calibrated RGB and IR videos demonstrate that precise tracking of the human face is achievable even with an FFR. The normalized cross-correlation methods further highlight the capability of IR imaging to accurately monitor and detect leakage. This breakthrough paves the way for real-time, automated detection of N95 FFR leakage, potentially deployable at operator workstations. This large, high-quality, open-access database is available to the scientific community to drive innovation in respiratory protection research and beyond.

INDEX TERMS Database, infrared imaging, N95 FFR leakage, occupational health and safety, quantitative fit testing, BigData.

The associate editor coordinating the review of this manuscript and approving it for publication was Nuno M. Garcia.

I. INTRODUCTION

A N95 Filtering Facepiece Respirator (N95 FFR) is a device that protect the wearer from inhaling harmful aerosols.

However, only N95 FFR devices correctly adapted to the wearer's face can offer adequate protection. For N95 FFR, which are the most frequently used in healthcare [1], the biggest contributory factor to the loss of protection is a leakage through the face seal [2], [3]. This implies that the protection offered by an FFR is significantly affected by the impaired fit between the FFR and the face [4]. FFR fit can be determined by qualitative or quantitative methods [5]: Quantitative Fit Test (QNFT) or Qualitative Fit Test (QLFT). These methods enable to choose the N95 FFR best suited to the wearer's facial morphology. Once the N95 FFR has been selected, the wearer must perform a self-test named fit check or user-seal-check each time it is used. This test checks the tightness of the N95 FFR through positive and negative pressure tests.

Concerning QNFT and QLFT, these methods enable the choice of the best-suited N95 FFR to the wearer's facial morphology. The distinction between QLFT and QNFT lies in both the method and the Pass/Fail criteria. In QLFT, the tester must verify the subject's ability to detect the challenge agent (sensitivity test) during breathing exercises. The subject must indicate if he detects the challenge agent during the QLFT; it is deemed ''Pass'' when the challenge agent is not detected. Conversely, QNFT employs a particle counter to calculate a fit factor. To obtain a test labeled ''Pass'', it requires a minimum fit factor of 100 for half facepieces [5]. However, these different methods have shown some limits. Indeed, they do not enable the precise leakage localizations, which are detected solely through irritation or a low fit factor. Additionally, they offer neither a visual representation of leakage nor an accurate measurement of their severity. Furthermore, these tests are not automated, requiring supervision by a specially trained professional. Taken together, fit testing is both resource-intensive and expensive in terms of time and cost [6].

Concerning the fit check, before COVID-19, Huh et al. [7] have already studied the accuracy of this fit check and have shown that almost 50% of N95 wearers don't perform an adequate verification. Lam et al. [8] and Regli et al. [6] have both concluded that the user-seal-check has low sensitivity, accuracy, and predictive value in determining the fit of N95 FFR. It is unreliable in detecting a proper fit or identifying leakage. Furthermore, many healthcare workers have been extensively exposed to COVID-19, and a significant proportion of them have contracted the virus [9], [10]. Furthermore, both this fit check and the QLFT rely on the judgment of each participant [6], meaning their results from these tests depend on the judgment of each participant.

All things considered, it seems important to find alternative methods to conventional fit testing and fit checking. These methods should enable the detection of N95 FFR leakage, specifically by locating and quantifying leakage automatically, to reduce costs and save time. Infrared (IR) technology has already demonstrated its capacity to detect leakage. Indeed, studying temperature variations at the face seal can help identify FFR leakage. These temperature changes arise from the contrast between the ambient air (the inhaled air) and the warm exhaled air [11].

Some studies have investigated leakage detection on N95 FFR using IR imaging [4], [12]. These studies have shown that IR imaging can assess whether an FFR is properly worn and can have a complementary role in QNFT. Harber et al. [13] have also shown that there is a correlation between FF and IR Imaging, but it was insufficiently strong to substitute for QNFT.

Other studies have focused on the integration of deep learning models for N95 FFR leakage detection using IR imaging [14], [15], [16]. All these studies have shown the potential of artificial intelligence in detecting air leakage for FFR wearers. Characteristics of the database used for their study and their model's training are given in the comparison Table. 1. Each study has collected IR images of human subjects wearing N95 FFR and has also conducted a fit test (QNFT or QLFT) [14], [15], [16].

Several limitations of their databases are mentioned in their respective studies. Indeed, Chapman et al. [14] have used only one type of P2 FFR, the flat-fold FFR, and have observed temperature changes solely in the nose area when studying the temperature gradient on the FFR.

Bari et al. [16] have identified immobilization of the participant as the biggest challenge in IR image recording. They have concluded that human movements influence image processing and results.

Similarly, Siah et al. [15] have faced several limitations, including a small sample size, an imbalance between male and female participants, and the use of only one type of N95 FFR, just like Chapman et al. [14]. Additionally, the study by Siah et al. [15] has lacked a FF for each test, as all participants have failed the QLFT, and there are no IR images of participants wearing an FFR after a 'Pass' QLFT test.

In summary, these databases appear to be insufficient for training deep learning models designed to automatically detect and quantify leakage around the face seal of a moving participant. Several critical gaps persist within these datasets: the absence of four different viewpoints recorded, the lack of FF measurements for each test, a limited and imbalanced number of participants, a large volume of data primarily consisting of IR videos, the use of different FFR N95 and finally the absence of methods to account for participant motion [14], [15], [16].

Considering the context and the various limitations highlighted in previous studies, the objective of the present study is to develop a comprehensive and robust database that adheres to several key criteria:

- → Collect data on a large and balanced number of participants;
- → Include participants with diverse facial morphologies wearing different types of N95 FFR;
- → Record high-definition IR and RGB videos from multiple angles of participants wearing N95 FFR;

→ Conduct two QNFT for each N95 worn by a participant, one at the beginning and one at the end of the test;
→ Make the database accessible to the scientific community.

The addition of RGB video recording enables the tracking of various points on the face of a moving person wearing an N95. For instance, Jiang et al. [17] have used RGB and IR sensors to detect respiratory infections by first identifying face and N95 FFR regions in the RGB frames, then mapping these regions to the thermal frames, and finally capturing the regions of interest (ROIs) in the thermal frames. Some computer codes such as MediaPipe [18] enable human face tracking on RGB videos, which will eliminate the problem of movements, as quoted by Bari et al. [16]. The version of MediaPipe that can create landmarks on the face can't work on IR images due to the nature of IR videos and because the MediaPipe face mesh was trained on RGB visual datasets. The MediaPipe Face Mesh is based on deep learning, utilizing a convolutional neural network (CNN) to detect and track facial landmarks accurately in real-time. This is primarily because IR technology captures thermal radiation, which significantly differs from the visual light spectrum in RGB images. In addition, IR and RGB data can be merged for face tracking in IR videos. Numerous studies have explored this fusion using RGB and IR cameras [19], [20], as well as methods to calibrate these cameras with a checkerboard [21], [22].

II. METHODOLOGY

A. MATERIAL

1) IMAGING SYSTEM CONFIGURATION

The study aims to investigate temperature variations of a human face wearing an N95 FFR during normal breathing, considering human movement. For that, a complete imaging system was developed to study these variations, including four different elements: an RGB camera, an IR camera, a synchronization system and a Stereo camera calibration system [23]. The two cameras used, are detailed in Table. 2. They were chosen for their high-resolution level and frame rate similarity. A 50 mm lens was chosen to operate with the IR camera because this lens enables a display similar to that of the RGB camera.

The imaging system was developed on the CAO software, SolidWorks 2022 (Dassault Systems, Waltham, MA) and was printed with the Ultimaker S5 3D Printer (Ultimaker B.V., Utrecht, Netherlands) as shown in black in the Fig. 1.

A RGB camera deep adjustment was added to this system for a better alignment between the two lenses. The main requirement of this imaging system was the necessity to create a system where the lenses of the cameras were as close as possible to minimize the distance between these lenses [21]. Indeed, it enables the recording of similar videos and facilitates calibration between these two cameras. Another requirement was that each camera should not move relative to the other during all data collection to avoid a remaking of calibration.

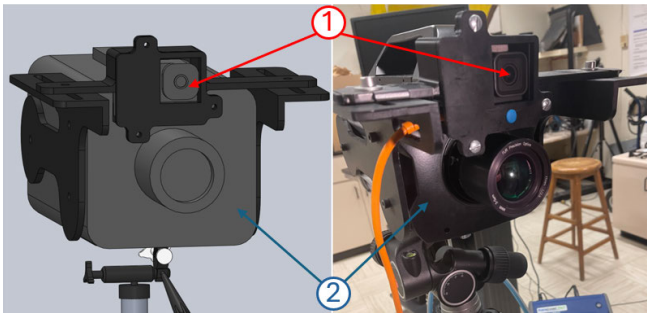

FIGURE 1. Modeling and design of the imaging system, 1) RGB camera, 2) IR camera.

2) IMAGING SYSTEM CALIBRATION

Once the cameras were installed, immobile and ready for use, they needed to be calibrated. Stereo camera system calibration involves aligning two cameras to capture the same scene accurately and reconstructing it in 3D, using a known pattern like an 8×8 checkerboard to determine intrinsic and extrinsic parameters. The calibration used an aluminum checkerboard, made by sticking adhesive vinyl on an aluminum sheet, with the checkerboard pattern cut into the vinyl. Aluminum's low emissivity ($\approx$0.02 at 20°C [24]) contrasts with vinyl's high emissivity ($\approx$0.95 at 20°C [25]), allowing an IR camera to capture the difference when a lamp heats the checkerboard. The process starts by capturing multiple images of the checkerboard from different angles to calculate intrinsic parameters like focal length and optical center and then estimating extrinsic parameters such as relative position and orientation. Using about 10 pairs of IR and RGB images of the checkerboard in different positions enhances accuracy (Fig. 2). Regular recalibration is recommended to account for changes in camera positions, lens focus, and ambient conditions, ensuring optimal 2D correspondences and precise 3D reconstruction for high-precision 3D imaging [26]. Ten pairs of images were captured daily for calibration during each day of data collection.

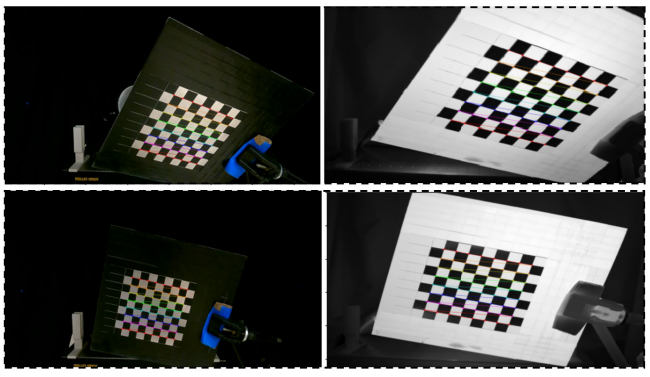

FIGURE 2. Two IR and RGB image pairs of the aluminum checkerboard in 2 different positions for calibration.

TABLE 1. Information about database used to develop their deep learning models.

Studies	Chapman et al. [14]	Bari et al. [16]	Siah et al. [15]
Participants (Female/Male)	48 (36/12)	8 (2/6)	17 (15/2)
Fit Test Type	QNFT	QNFT	QLFT
Fit Test Device	TSI Portacount Model 8048	TSI Portacount Model 8038	N/A
IR Camera Model	FLIR One Gen3 - iOS	Jenoptik VarioCam®	FLIR T365
IR Camera Resolution	160*120 pixels	640*480 pixels	320*240 pixels
Points of View recorded	(1) front	(5) top, left, bottom, front, right	(5) top, left, bottom, front, right
IR data used	48 images	462 images	N/A

TABLE 2. Characteristics of two cameras used to collect data.

Cameras	RGB	IR
Manufacturer	GoPro Inc.	FLIR Systems
Model	Hero 9	X8501sc
Resolution	1920*1080 pixels	1280*1024 pixels
Sensitivity	∅	<20 mK
Frame Rate	30 Hz	(25 to 30)[a] Hz
Software used	OBS Studio	ResearchIR Max

[a]Frame rate for the IR camera was no constant, varying from 25 Hz to 30 Hz. However, the duration of each IR video was constant in this study (35 seconds).

3) IMAGING SYSTEM SYNCHRONIZATION

Once IR and RGB cameras were fixed and calibrated, it was important to synchronize the recordings from each camera to avoid a time difference between IR and RGB videos. The two cameras work with different software, each with a different time delay at the start of recording, making automatic synchronization complicated. A synchronization system was developed to solve this issue, controlled by Bluetooth and composed of a halogen lamp, an electromagnet, an Arduino Uno and 3D printing pieces. This system was placed just behind the participant on a wood panel. For each video recording start, a 10-second delay allowed the lamp to heat up. At the end of this period, a pulse of heat and light was visible to the two cameras, as shown in Fig. 3. Furthermore, a computer code was developed to recognize this pulse and synchronize the IR and RGB videos.

FIGURE 3. Two IR and RGB image pairs with and without pulse of heat and light (encircled in red) for synchronization.

4) QUANTITATIVE FIT TESTING

To detect an N95 FFR leakage with IR technology, it was essential to rely on a technology that is already used daily by professionals and has already proven its efficiency. The reference instrument that was used in this study is the PortaCount® Instrument, Model 8038 (TSI Incorporated, Shoreview, Minnesota, USA). It enables the performance of a QNFT by counting particles inside and outside the N95 FFR during 8 breathing exercises, as described by OSHA. The Fit Factor (FF) is then calculated by dividing the number of particles outside the N95 FFR by the number of particles inside. The PortaCount® Model 8038 measures FF from 0 to 200. For an N95 FFR, the success criterion to pass a QNFT is an FF higher than 100 [5]. The instrument must be used in a controlled environment with enough particles in the ambient air. For that, a particle generator, the 24 Jet Collision Nebulizer (BGI, Inc) was used. It operates with different pressures and solutions, but in the context of the present data collection, a pressure of 30 PSI and a salt solution (c = 0,05 g/mL) were chosen. These parameters enabled constant particle generation around 10000 particles/cm^3 in ambient air and were safe for participants' health. The average diameter of the generated particles was less than 100 nanometers.

5) OVERALL INSTALLATION

The installation integrated the various instruments and allowed one participant to sit in front of the cameras. As shown in Fig. 4, it consisted of a dark tent, a swivel chair and the imaging system. The dark tent served two purposes. It minimized reflectivity and prevented external disturbances during data collection and calibration on the checkerboard, as done by Roberge et al. [4]. The dark tent also created a smooth bottom on videos, making the synchronization easier. The swivel chair allowed participants to rotate with the chair instead of turning their heads, thus limiting their head movements. Indeed, head movements can change N95 FFR fit and by the same way affect correlation between FF and IR evaluation. The tripod of the imaging system and the swivel

chair were fixed to the ground. This helped to maintain a constant distance of 50 centimeters between the participant's face and the camera lenses. Keeping this distance constant helped reduce the need for frequent adjustments of the IR camera lens and, consequently, minimized the number of camera calibrations required.

This setup was implemented in a laboratory with controlled temperature and relative humidity, maintained using a thermostat set to 21°C. During data collection, the temperature ranged from 20°C to 22.5°C, while the relative humidity fluctuated between 17% and 23%.

FIGURE 4. Final installation including the imaging system, the PortaCount®, the dark tent and the swivel chair.

B. METHODS

1) PARTICIPANTS

The ethical approvals to conduct the data collection on participants were obtained by the University of Quebec at Rimouski (UQAR) and Laval University Research Ethics Committees (approval number 2024-276) in the fall of 2023. Participant recruitment was done in the student community of Laval University. To be recruited, the participant had to meet the following eligibility criteria, similar to those for a QNFT [5]: Not show flu-like symptoms, not have skin irritation or inflammation on the face, not have eaten, drunk, or smoked 1 hour before the event, for men, be clean-shaven at least 24 hours beforehand. 62 participants participated, 36 women (58%) and 26 men (42%). Before starting data collection, each one signed two consent papers, one to participate in the data collection and another to give agreement for image sharing in publications or reports. Refusing to share their data did not result in the cancellation of data collection.

TABLE 3. N95 FFR characteristics tested during data collection.

Manufacturer	N95 Type	Valve	Size	Test Count
3M	8210	No	Standard	62
3M	8210V	Yes	Standard	12
3M	VFlex 9105	No	Standard	27
Moldex	2200	No	M/L	62
Moldex	2300	Yes	M/L	12
Honeywell	DC300	No	One Fit	61
Honeywell	DC300V	Yes	One Fit	12

Each N95 FFR are Molded Cup shaped, except 3M VFlex 9105, which is a V-shaped pleat. Total tests conducted = 248

2) PROTOCOL

After the consent papers were signed and following an explanation of the protocol for data collection, the data collection process began. Each participant tested 4 different N95 FFR out of 7 available options (Table. 3).

The N95 FFRs from various manufacturers were selected for their distinct geometries, designed to create diverse leakage scenarios. Indeed, one of the objectives of this study is to examine different leakage scenarios occurring at various locations around the face seal. One can reach this objective by multiplying N95 FFR geometries and participant facial morphologies. It is important to notice that the data collection was not performed to test the N95 FFR's performance to fit. The participants did not receive instructions about wearing an N95 FFR. Therefore, the participants unintentionally created leakage.

As illustrated in Fig. 5, participants followed a test sequence that involved setting up an N95 FFR, undergoing an initial QNFT, breathing in front of the imaging system, and finally, completing a second QNFT. This protocol was developed following a preliminary study on a Static Advanced Headform wearing an N95 FFR. This study helped establish the number of fit tests conducted and the number of views recorded.

Data collection operated in the following sequence. First, participants, seated in front of the cameras, were given two minutes to put on and adjust an N95 FFR. QNFT tests were carried out at the beginning and end of the collection. It consisted of three exercises: normal breathing (50 seconds), deep breathing (50 seconds), and normal breathing (50 seconds). The two QNFT allowed verification that the N95 FFR fit did not change during the collection. The difference X (with $X = FF1 - FF2$) and the average between these two FF were then calculated. The difference enabled to class the reliability of each test. The greater difference, the less reliable the data. Indeed, a large difference meant the N95 FFR fit had changed during test. On the other hand, the average gave a global FF of the test.

The aim of the database is to correlate FF with IR videos, so 3 exercises were selected to observe the same leakage during the IR test. Exercises and sample time were selected from the eight exercises outlined in the OSHA protocol, as they are less likely to modify the face seal during testing.

During the IR test, the subject breathed normally and assumed four different positions over 35 seconds, positioning their face in front of the cameras, upwards, to the left,

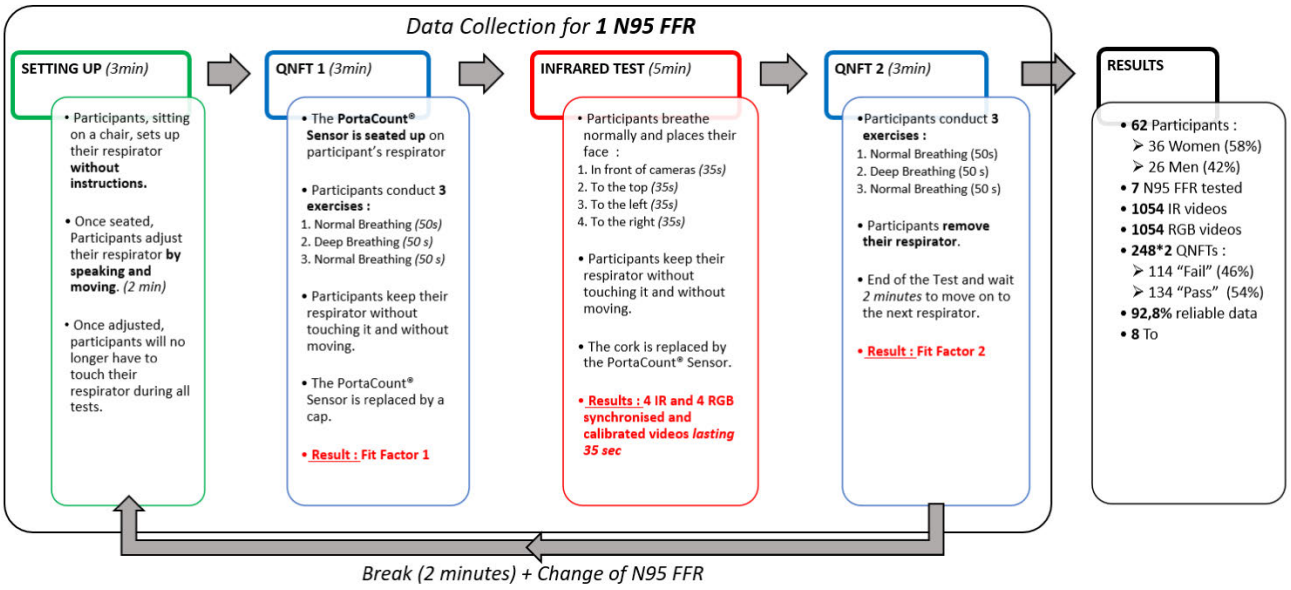

FIGURE 5. Detailed data collection protocol for 1 N95 FFR tested.

and finally to the right. These positions enabled to capture exactly and totally the participant face seal. Indeed, with one view, for example in front of cameras, the IR camera can't capture the entire face seal. To take these positions, the participants used the swivel rotation to avoid breaking the face seal and not changing their N95 FFR fit. It was requested that the participants minimize their head movements. The sweating of these participants was not controlled. Between each QNFT and the IR test, a replacement between a cap and the PortaCount® sensor was done. It was enabled to capture IR videos without the PortaCount® sensor influencing temperature variations on the N95 FFR or the face seal in IR videos. A cap was used because a QNFT requires the N95 FFR to be perforated to accommodate the PortaCount® sensor. Time recording was chosen to capture enough breathing cycle to study them. For a normal human breathing, frequency breathing is comprised between 12 and 20 cycles per minutes [27]. So, a time recording equal to 35 seconds represents several cycles captured between 7 and 12 cycles. At the end of each N95 FFR (starting from the 11th participant) a question about a possible feeling of leakage was asked to the participant. Their answer enables cross-reference information between an IR video, an FF and a participant's feelings. This information makes it easier to locate leakage with certainty.

Between each N95 FFR, the participant had a break of 2 minutes to breathe normally without N95 FFR. When the participant's face temperature was back to normal at the end of data collection, a last IR and RGB video recording of the participants without wearing an N95 FFR was done. This last recording enabled the evaluation of the size of the participant's face with an algorithm which calculates the number of pixels compared to a known face reference. Face length and face width of each participant were measured, and so it enabled the placement of each participant in the bivariate NIOSH Panel (Fig. 6). This figure shows the diversity of participant facial morphologies in this data collection, which is one of the aims of this study.

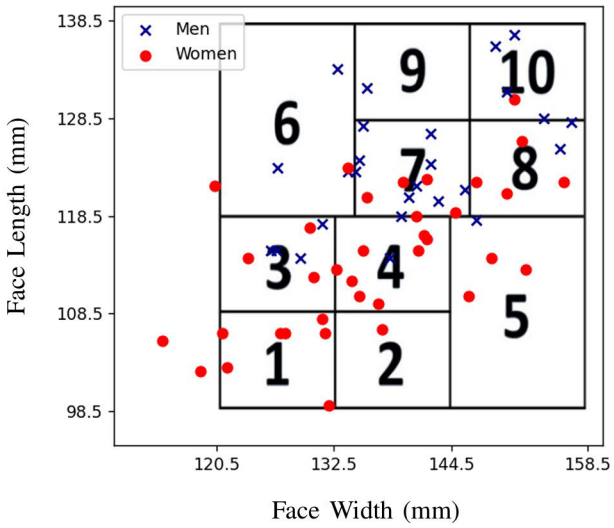

FIGURE 6. NIOSH bivariate panel as determined by Zhuang et al. [28] and distribution of 62 participants' face length and width.

III. RESULTS

A. RECORDING VISUALIZATIONS

As described previously, for each participant and each N95 FFR, IR and RGB videos lasting 35 seconds were captured in four different positions as shown in Fig. 7. OBStudio Software [29] (OBStudio, Inc.) enables the recording and export of RGB video in.mp4 format, while ResearchIR Max [30](FLIR Systems, Inc., Wilsonville, Oregon, USA) records in.ats format, a proprietary FLIR format that is

TABLE 4. Test reliability classification according to the difference between FF1 and FF2.

Reliability	Difference X	Test Count	Percentage(%)
Very reliable	$0 \leq X \leq 25$	212	85,5
Reliable	$25 < X \leq 50$	18	7,3
Little reliable	$50 < X \leq 100$	14	5,6
Unreliable	$100 < X \leq 200+$	4	1,6
Total	$0 \leq X \leq 200+$	248	100

unusable without Research IR Max and so in algorithms. The.tiff format, known for its high-quality images, was finally used to export these videos to avoid information and quality loss. For each participant, 34 videos were recorded, 17 IR videos (.tiff and.ats) and 17 RGB videos (.mp4). 4 positions for each of 4 N95 FFR = 16 videos + 1 video without an N95 FFR. As mentioned before, the four positions allow visualization of the face seal entirely. Additionally, the IR camera's high sensitivity and high acquisition frame rate allow for precise monitoring of temperature variations around the face seal, with a sensitivity of less than 20 mK.

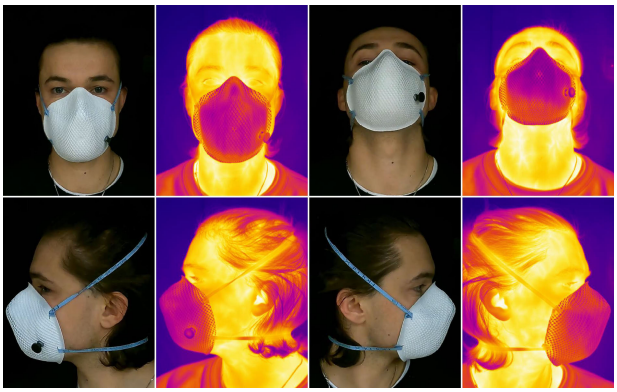

FIGURE 7. Visualization of IR and RGB images in 4 different positions: front, top, left, right.

B. TEST RELIABILITY

In addition to IR and RGB videos, each N95 FFR tested by a participant involved two QNFT, resulting in two measured fit factors. The difference and the average of the fit factors were calculated to classify each test. The difference $|FF1 - FF2|$ was used to classify the reliability of a test, as shown in the Table. 4. There were, in totality, 62 participants, and each one wore 4 N95 FFR, so there were 248 (62*4) tests. This classification was decided according to the accuracy of PortaCount® which is ±20 when the higher fit factor measurable is 200 [31]. With this classification, more than 92.8% of data collected are considered as reliable or very reliable. A difference between FF1 and FF2 greater than 100 indicates that the N95 FFR fit changed significantly during data collection. This classification helps determine which data will be used first and which will be discarded.

C. TEST CLASSIFICATION

Regarding the average between FF1 and FF2, this value was used to classify each test according to the FF. A distribution

TABLE 5. Example of 2 tests for 2 participants.

Participant N°	N95 Type	Fit Factor	Leakage Area Feeling[a]
60	3M 8210	10.5	Left Nose
41	3M 8210	200+	No Feeling

[a]The point of view on the leakage area feeling is always provided by the data tester, namely the observer.

of the number of QNFT based on FF is presented in Fig. 8. This distribution can also be used to count how many tests are classified as 'Pass' and 'Fail.' A test is considered a 'Pass' if its FF is higher than 100 [5]. In these tests, 114 (46%) are considered as "Fail" and 134 (54%) as "Pass". The database is then constituted for each test by the bivariate parameter of the participant, 17 IR videos, 17 RGB videos, 2 FF labels and a test reliability.

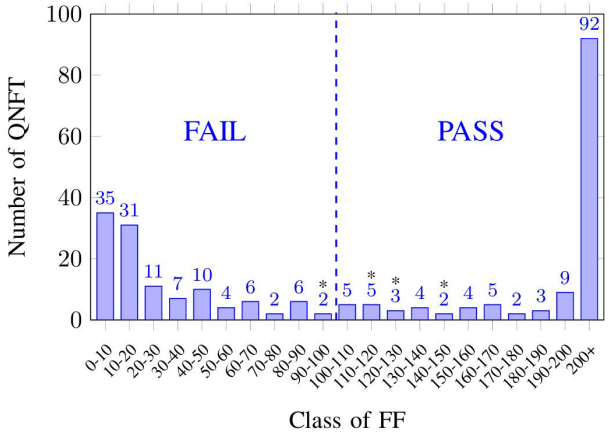

FIGURE 8. Test distribution according to the average between FF1 and FF2 (*Corresponds to the class of FF with 1 unreliable test).

D. PRELIMINARY RESULTS

To show an example of using this database, sequences from two different participants, were processed and compared. The sequences from participants number 60 and 41 are used as an example. The information regarding these tests is detailed in Table. 5.

For each participant and each recorded point of view, it is possible to visualize the temperature variations between exhalation and inhalation over a single breathing period. These variations are calculated as the pixel-wise subtraction between two images corresponding to the peak temperature of the exhalation and the inhalation: $I_{exhalation}$ and $I_{inhalation}$:

$$I(i,j) = I_{\text{exhalation}}(i,j) - I_{\text{inhalation}}(i,j), \tag{1}$$

where i and j represent the pixel coordinates, with $i \in [0, 1280]$ and $j \in [0, 1024]$. Fig. 9 presents these temperature variations for one single breathing period. These heatmaps align with the leakage feeling reported by participant 60 in the area of the left nostril and the absence of such a feeling reported by participant 41. This presence and absence of leakage are also consistent with the FF measurements collected for these two participants wearing a 3M 8210 N95 (Table 5).

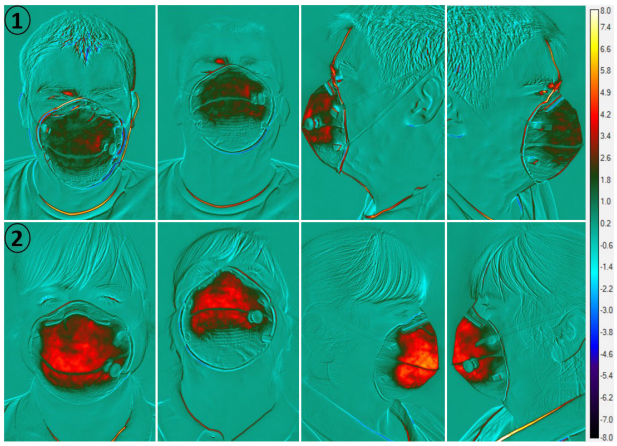

FIGURE 9. Variation of temperature (in °C) over a single breathing period for each recorded point of view. 1) Participant 60, 2) Participant 41.

However, this subtraction method has its limitations, which are evident in the heatmaps (Fig. 9). Specifically, some temperature variations are not due to leakage. For instance, temperature variations of approximately 7-8°C are observed near each participant's collar. This phenomenon is also evident for participant 60, particularly around the face seal and near the right ear in the "front" view, as well as at the forehead level in the "right" view ((1) in Fig. 9). These temperature variations are caused by movement and can be attributed to the temperature difference between the pullover and the skin in the collar area. Even though these two participants exhibit only slight movements, small movements can lead to errors in temperature readings. Overall, accounting for participant movement is crucial for accurate leakage detection, a finding consistent with the study conducted by Bari et al. [16].

The method used to account for human movements in this study is the MediaPipe [18] approach, which utilizes both RGB and IR videos. Specifically, the MediaPipe method enables the tracking of key points on a moving human face in RGB videos. After synchronizing the RGB and IR 3, stereo camera system calibration is applied [21], [22] using the checkerboard shown in Figure 2. MediaPipe is applied on the RGB images, as shown in Fig. 10 (left side). The information is then transferred to the IR sequence, where the landmarks of the face mesh detected by MediaPipe are mapped onto the IR images, as illustrated in Fig. 10 (right side). This process ensures accurate correspondence between the RGB and IR data, enabling robust facial feature detection across both modalities.

After identifying the landmarks, it is possible to extract the temperature at specific points on the face (Fig. 10). In this case, landmarks numbers 56 and 464 are used. The results of the temperature measurements at these points are shown in Fig. 11. This approach enables precise thermal analysis of the face with a sensitivity of less than 20 mK, based on accurately mapped landmarks from RGB images, even when the participant moves during the recording.

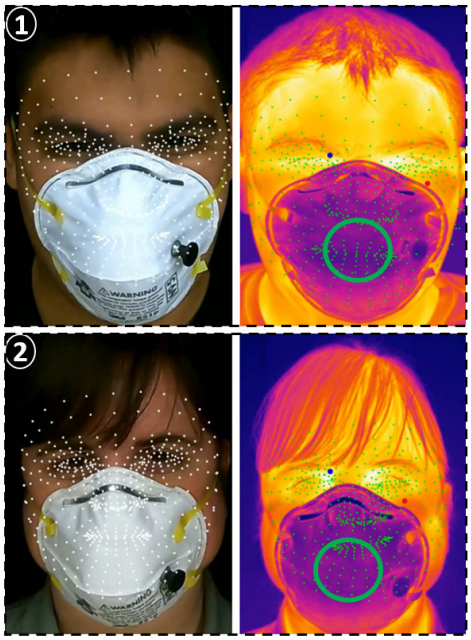

FIGURE 10. Application of MediaPipe on RGB/IR Images after synchronization and calibration. 1) Participant 60, 2) Participant 41. Landmark 56: blue point on the left side, at eye level; Landmark 464: red point on the right side, at cheek level; Center of mask: green circle. The size of the landmarks is enlarged for better visibility; their original size is 4*4 pixels.

After extracting the landmarks on the IR images, landmarks that could potentially indicate thermal leakage were selected. This selection allows visualizing the temperature at these critical points. Fig. 10 shows the locations of these selected landmarks ((blue point for landmark 56 on the left side, at eye level, and red point for landmark 464 on the right side, at cheek level). Fig. 11 presents a diagram of the temperature changes over time at these two points for participants 60 and 41. This analysis helps in understanding the thermal behavior of the face at specific landmarks under different conditions.

This diagram is consistent with the heatmaps (Fig. 9). It's also noticeable that the mean temperature fluctuates over the recording period depending on the landmark. Landmark 56 registers a higher mean temperature compared to landmark 464. For the same landmark, this mean temperature also varies between participants. As for temperature fluctuations, they are not constant throughout the test, as illustrated by the blue curve for participant 60. The preliminary results, therefore, show that the method is capable of showing the presence of potential leakage.

It is also valuable to analyze the temperature evolution of the N95 FFR, as it provides essential insights into each participant's breathing patterns, including respiratory rate and amplitude. However, detecting the center of the mask to calculate the respiratory temperature was challenging, while the mask was not part of the face. To address this issue, a semantic segmentation method was implemented using a U-Net variant proposed by Arbane et al. [32]. This deep

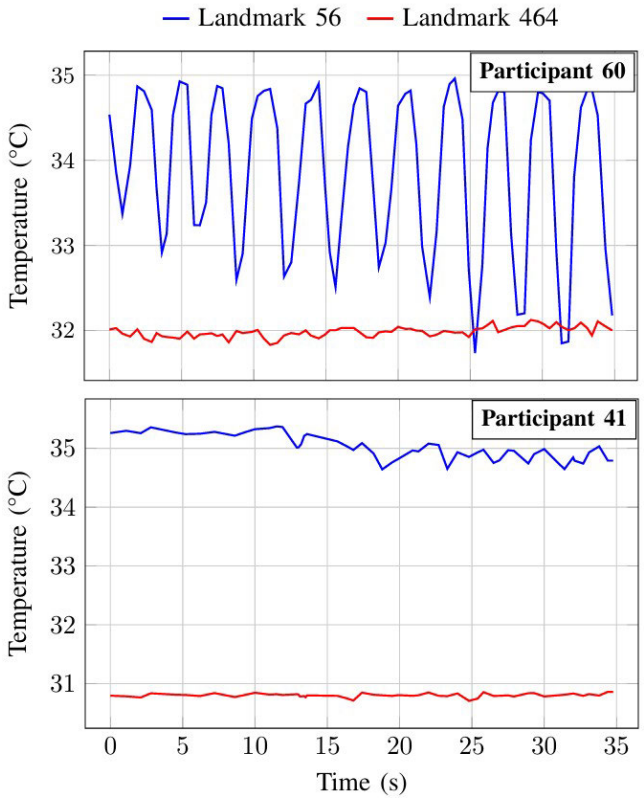

FIGURE 11. Comparative analysis of temperature variations between two participants at identical landmarks.

learning model enables the automation of N95 FFR detection and was developed on human subjects wearing N95 FFR. After segmentation, the center of the mask (in green in Fig. 10) was selected to measure the breathing pattern and temperature variations, including frequency and amplitude. Fig. 12 presents the two participants' average temperature evolution on the N95 FFR. Additionally, a spectral analysis could be performed to identify the dominant frequency components.

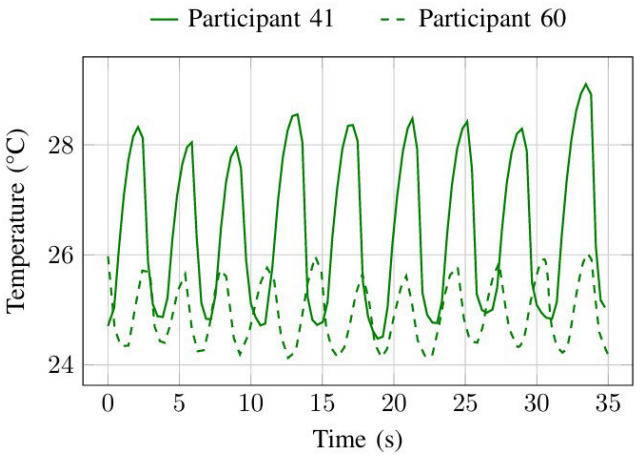

FIGURE 12. Evolution of the average temperature across all pixels within the green circle at the center of the N95 FFR, using mask segmentation [32].

To determine whether temperature variations are due to a leakage rather than movements, blinking, or external factors, one approach is to analyze the similarity between thermal signals recorded at the N95 FFR (Fig.12) and at the leakage site (Fig.11) for each participant. This can be achieved using normalized cross-correlation [33], which measures the similarity between two signals with a time lag (τ). This method disregards the continuous component and the signal amplitudes, focusing solely on temperature variations, which are indicative of leakage [11]. A high correlation value (close to 1) indicates a strong similarity between these thermal signals and suggests the presence of a potential leakage. Indeed, the breathing pattern will be more pronounced in areas with leakage than in those without.

These two thermal signals are discrete and sampled at a frame rate of 30 Hz over a duration of 35 seconds, resulting in N (the number of samples) being 1050. Formulas (2) enables to normalize a discrete signal $g[k]$ with μ_g the mean and σ_g the standard deviation of the discrete signal.

$$g_{\text{norm}}[k] = \frac{g[k]-\mu_g}{\sigma_g}, \text{ where :}$$
$$\mu_g = \frac{1}{N}\sum_{k=1}^{N} g[k] \;\; ; \;\; \sigma_g = \sqrt{\frac{1}{N}\sum_{k=1}^{N}\left(g[k]-\mu_g\right)^2} \quad (2)$$

The normalized cross-correlation $R_{gf}^{\text{norm}}[n]$ between two discrete signals $g[k]$ and $f[k]$, where n represents the sample lag and $*$ denotes the convolution product, is defined by formula (3).

$$R_{gf}^{\text{norm}}[n] = (f_{\text{norm}} * g_{\text{norm}})[n]$$
$$R_{gf}^{\text{norm}}[n] = \sum_{k=0}^{N-1} f_{\text{norm}}[k] \cdot g_{\text{norm}}[k+n] \quad (3)$$

Once calculated, this normalized cross-correlation can be expressed as a function of the time delay τ using the frame rate. Fig. 13 presents the normalized cross-correlation R for two studied landmarks (56 & 464) with the thermal signal at the N95 FFR for each participant as a function of the time lag (τ). A strong correlation is observed for landmark 56 of participant 60, reaching 0.91 at a time lag of 0.26 seconds ($R(0.26) = 0.91$, the black cross on Fig. 13). This strong correlation supports the potential leakage detected in Fig. 11. In contrast, for the other landmarks, the correlation is significantly lower, falling below 0.35.

The calculation of the normalized cross-correlation at each Mediapipe landmark with the thermal signal at the FFR could allow for precise leakage detection. Other methods to check the similarity between two signals, such as cross-spectral analysis [34] or Pearson correlation [35], could also be explored. Future work will investigate these methods and determine which is most suitable for detecting N95 leakage. Additionally, future efforts will focus on developing a method to quantify each leakage by analyzing the thermal signal amplitude at specific landmarks around the face seal. These

methods will be applied to the entire dataset, facilitating the efficient training of deep learning models.

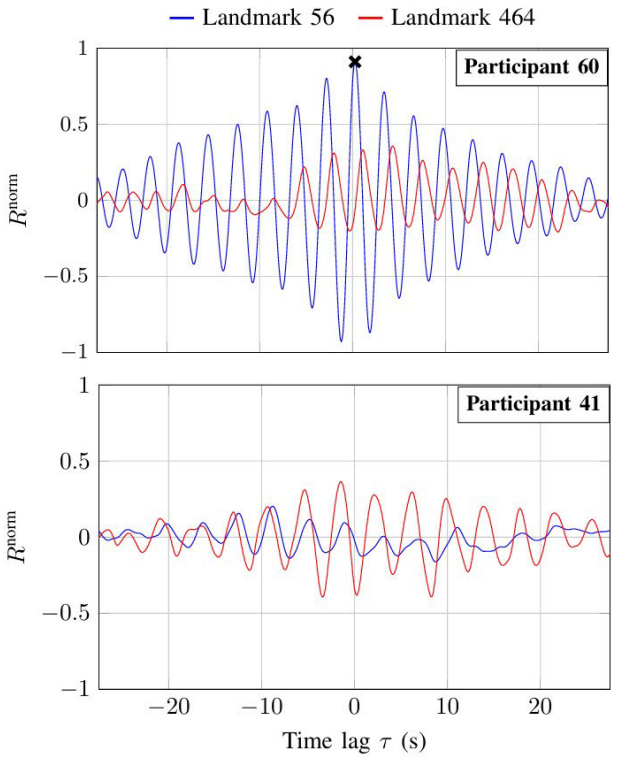

FIGURE 13. Normalized cross-correlation R^{norm} between breathing pattern and each studied landmark (56 & 464) for two participants (60 & 41).

More recently, Arbane et al. employed their semantic segmentation approach [32] for a purpose different from that of this study. They used it to eliminate the need for RGB videos by applying their model to each frame, enabling the detection of FFR and the face seal at each position of a participant. This allows for the study of the face seal independently of the participant's movements.

IV. DISCUSSION

The development of the testing installation has allowed for the collection and compilation of a database of participants wearing N95 FFR in various positions. Preliminary results demonstrate the method's capacity to detect potential leakage. Concerning the reliability of data collected, based on the difference between FF1 and FF2, 85.5% of the data are considered very reliable, 7.3% are considered reliable, 5.6% are considered little reliable and 1.6% are considered unreliable. The unreliable data is explained by change in the FFR fit during the recording of IR and RGB videos. These videos are still usable, but the labeling of the FF on these tests remains unreliable.

Recording videos to accurately capture the face seal proved complex during data collection. Positioning the participant with meticulous precision is imperative to obtain appropriate data. Excessive rotation of the chair results in partial capture of the face seal. Using four views of the participant's face ensured capturing the entire face seal. However, achieving adequate capture might require fewer views.

The objective is not only to locate leakage, but also to quantify it. Labeling each test using the FF will allow leakage-level classes to be created. Currently, the two main existing classes are "Pass" and "Fail", for the two fit testing methods: QNFT and QLFT. However, given the distribution of PortaCount® measures (Fig. 8), there is potential for refining and multiplying these classes.

This database could be also used to detect respiratory issues by studying breathing patterns through the mask, assessing the thermal impact of wearing an N95 FFR, or studying the fluid mechanics of breathing through an N95 FFR. For example, Arbane et al. [32] have already utilized these data to develop a deep learning model aimed at improving the segmentation of an N95 FFR using IR videos. This model demonstrates high accuracy and enables precise analysis of the face seal. Future work will focus on an in-depth investigation of the face seal to enable automatic leakage detection, alongside exploring alternative correlation methods proven to enhance this process. Statistical analyses will be employed to determine the most effective approach. Making this localization and quantification automatic would also allow detecting leakage at workstations close to the operators, ensuring them respiratory protection throughout their activity. Many other fields where hazardous fine particles are present and where respiratory protection is essential, such as construction, healthcare, manufacturing, mining, laboratories, and firefighting, could benefit from this technology. All things considered, this database could play a significant role in occupational safety and respiratory health research.

V. CONCLUSION

A database of high-quality IR and RGB videos was created. 62 participants, 36 women and 26 men, each tested 4 FFR in 4 different positions (front, top, left, right) and they performed 2 QNFT for each FFR tested: one before video recording and one after. This database comprises 1054 IR, 1054 RGB videos, and 496 QNFT, totaling 8To. To our knowledge, it currently represents the most comprehensive database in the field of N95 FFR leakage detection using IR imaging.

This database has been specifically created to develop deep learning models for comprehensive N95 FFR leakage detection. These models could automatically locate and quantify leakage across the entire face seal of N95 FFR. This deep learning technology has the potential to provide an alternative to current methods, ensuring adequate respiratory protection for all N95 FFR users, particularly healthcare workers.

DATA ACCESSIBILITY

A website[1] has been developed to showcase a sample database and the procedure to follow in order to obtain it. This database is available only to students, research groups,

[1]https://saferespirator.uqar.ca/

or research institutions with approval from an authorized authority. Therefore, we will not accept applications from generic email addresses (gmail.com, hotmail.com, etc.); only applications from email addresses associated with non-profit institutions such as schools or research institutes will be considered.

This website provides the rules and the license agreement that must be signed and returned. The use of participants' data is clearly outlined in these rules. Any participant who has not signed the consent form to share their face must have their eye area blurred or hidden before their data can be used. A list of each participant's consent status is available on this website and in the database.

Concerning the data, only raw data is provided. The videos are available in.tiff and.ats formats for IR recordings and.mp4 format for RGB videos. For the QNFT results, the Portacount® output is provided as a PDF summarizing the participant number, the N95 FFR model, and the fit factor.

Regarding data organization, the dataset is divided into two collection phases. The first phase includes 35 participants, while the second phase includes 27 participants. For each participant, the data is organized by N95 FFR model. Additionally, for each N95 FFR, the corresponding IR, RGB, and FF data are provided in the previously specified formats, with recordings captured from four different viewpoints: top, left, front, and right.

Additionally, no scripts are included in the dataset. However, an Excel file named *SummaryTable_ToShare* is provided, summarizing participant information such as their number, sex, and facial dimensions (height and width). This file also includes a summary of leakage feeling for each participant and each N95 FFR, numbered 11 to 62, as well as a summary of the QNFT results conducted by the participants.

ACKNOWLEDGMENT

The authors would like to thank all the participants who took part in their data collection. Clemente Ibarra Castanedo and Denis Ouellet for their assistance throughout this study and the individuals working at the 3D printing services at UQAR and ULaval.

REFERENCES

[1] L. A. Pompeii, C. S. Kraft, E. A. Brownsword, M. A. Lane, E. Benavides, J. Rios, and L. J. Radonovich, "Training and fit testing of health care personnel for reusable elastomeric half-mask respirators compared with disposable N95 respirators," *JAMA*, vol. 323, pp. 1849–1852, Mar. 2020.

[2] M. Clayton and N. Vaughan, "Fit for purpose? The role of fit testing in respiratory protection," *Ann. Occupational Hygiene*, vol. 49, no. 7, pp. 545–548, 2005.

[3] S. A. Grinshpun, H. Haruta, R. M. Eninger, T. Reponen, R. T. McKay, and S.-A. Lee, "Performance of an N95 filtering facepiece particulate respirator and a surgical mask during human breathing: Two pathways for particle penetration," *J. Occupational Environ. Hygiene*, vol. 6, no. 10, pp. 593–603, Sep. 2009.

[4] R. J. Roberge, W. D. Monaghan, A. J. Palmiero, R. Shaffer, and M. S. Bergman, "Infrared imaging for leak detection of N95 filtering facepiece respirators: A pilot study," *Amer. J. Ind. Med.*, vol. 54, no. 8, pp. 628–636, Aug. 2011.

[5] *1910.134 App A—Fit Testing Procedures (Mandatory)*. Accessed: Apr. 4, 2024. [Online]. Available: https://www.osha.gov/laws-regs/regulations/standardnumber/1910/1910.134AppA

[6] A. Regli, A. Sommerfield, and B. S. von Ungern-Sternberg, "The role of fit testing N95/FFP2/FFP3 masks: A narrative review," *Anaesthesia*, vol. 76, no. 1, pp. 91–100, Jan. 2021.

[7] Y. J. Huh, H. M. Jeong, J. Lim, H. Y. Park, M. Y. Kim, H. S. Oh, and K. Huh, "Fit characteristics of N95 filtering facepiece respirators and the accuracy of the user seal check among Koreans," *Infection Control Hospital Epidemiology*, vol. 39, no. 1, pp. 104–107, Jan. 2018.

[8] S. C. Lam, J. K. L. Lee, S. Y. Yau, and C. Y. C. Charm, "Sensitivity and specificity of the user-seal-check in determining the fit of N95 respirators," *J. Hospital Infection*, vol. 77, no. 3, pp. 252–256, Mar. 2011.

[9] A. K. Sahu, V. Amrithanand, R. Mathew, P. Aggarwal, J. Nayer, and S. Bhoi, "COVID-19 in health care workers—A systematic review and meta-analysis," *Amer. J. emergency Med.*, vol. 38, no. 9, pp. 1727–1731, 2020.

[10] S. L. Burrer, M. A. de Perio, M. M. Hughes, D. T. Kuhar, S. E. Luckhaupt, C. J. McDaniel, R. M. Porter, B. Silk, M. J. Stuckey, and M. Walters, "Characteristics of health care personnel with COVID-19—United States, February 12-april 9, 2020," *MMWR. Morbidity Mortality Weekly Rep.*, vol. 69, no. 15, pp. 477–481, Apr. 2020.

[11] J. Kerl, M. Wenzel, and D. Köhler, "Thermal imaging of mask leakage during pressure-controlled ventilation (bipap therapy)," *Somnologie*, vol. 8, no. 3, pp. 83–86, 2004.

[12] J. Dowdall, I. Pavlidis, and J. A. Levine, "Thermal image analysis for detecting facemask leakage," in *Thermosense*, vol. 5782. Bellingham, WA, USA: SPIE, 2005, p. 46.

[13] P. Harber, J. Su, A. D. Badilla, R. Rahimian, and K. R. Lansey, "Potential role of infrared imaging for detecting facial seal leaks in filtering facepiece respirator users," *J. Occupational Environ. Hygiene*, vol. 12, no. 6, pp. 369–375, Jun. 2015.

[14] D. Chapman, C. Strong, K. D. Tiver, D. Dharmaprani, E. Jenkins, and A. N. Ganesan, "Infra-red imaging to detect respirator leak in healthcare workers during fit-testing clinic," *IEEE Open J. Eng. Med. Biol.*, vol. 5, pp. 198–204, 2024.

[15] C. R. Siah, S. T. Lau, S. S. Tng, and C. H. M. Chua, "Using infrared imaging and deep learning in fit-checking of respiratory protective devices among healthcare professionals," *J. Nursing Scholarship*, vol. 54, no. 3, pp. 345–354, May 2022.

[16] A. Bari, R. Lamoureux-Lévesque, A. Ahmed Si, J. Brousseau, A. Bahloul, B. Clothilde, Y. Yaddaden, and X. Maldague, "COVID-19, wearing N-95 masks in clinical environments: Thermographic detection of air leaks," in *Proc. Int. Conf. Quant. Infr. Thermography*, 2022, pp. 1–10.

[17] Z. Jiang, M. Hu, Z. Gao, L. Fan, R. Dai, Y. Pan, W. Tang, G. Zhai, and Y. Lu, "Detection of respiratory infections using RGB-infrared sensors on portable device," *IEEE Sensors J.*, vol. 20, no. 22, pp. 13674–13681, Nov. 2020.

[18] Google. (2023). *Mediapipe Face*. [Online]. Available: https://developers.googleblog.com/en/mediapipe-enhancing-virtual-humans-to-be-more-realistic/

[19] J. Richter, C. Wiede, S. Kaden, M. Weigert, and G. Hirtz, "Skin temperature measurement based on human skeleton extraction and infrared thermography—An application of sensor fusion methods in the field of physical training," in *Proc. 12th Int. Joint Conf. Comput. Vis., Imag. Comput. Graph. Theory Appl.*, 2017, pp. 59–66.

[20] M. Brenner, N. H. Reyes, T. Susnjak, and A. L. C. Barczak, "RGB-D and thermal sensor fusion: A systematic literature review," *IEEE Access*, vol. 11, pp. 82410–82442, 2023.

[21] C. Chen, B. Yang, S. Song, M. Tian, J. Li, W. Dai, and L. Fang, "Calibrate multiple consumer RGB-D cameras for low-cost and efficient 3D indoor mapping," *Remote Sens.*, vol. 10, no. 2, p. 328, Feb. 2018.

[22] I. R. Spremolla, M. Antunes, D. Aouada, and B. Ottersten, "RGB-D and thermal sensor fusion-application in person tracking," in *Proc. Int. Conf. Comput. Vis. Theory Appl.*, vol. 4, 2016, pp. 610–617.

[23] R. Beschi, X. Feng, S. Melillo, L. Parisi, and L. Postiglione, "Stereo camera system calibration: The need of two sets of parameters," 2021, *arXiv:2101.05725*.

[24] S. Marinetti and P. G. Cesaratto, "Emissivity estimation for accurate quantitative thermography," *NDT & E Int.*, vol. 51, pp. 127–134, Jun. 2012.

[25] K. Rakrueangdet, N. Nunak, T. Suesut, and E. Sritham, "Emissivity measurements of reflective materials using infrared thermography," in *Proc. Int. Multi. Conference Engineers Comput. Scientists (IMECS)*, 2016, pp. 1–12.

[26] Q. Gu, K. Herakleous, and C. Poullis, "3DUNDERWORLD-SLS: An open-source structured-light scanning system for rapid geometry acquisition," 2014, *arXiv:1406.6595*.

[27] G. Yuan, N. A. Drost, and R. A. McIvor, "Respiratory rate and breathing pattern," *McMaster Univ. Med. J.*, vol. 10, no. 1, pp. 23–25, 2013.
[28] Z. Zhuang, B. Bradtmiller, and R. E. Shaffer, "New respirator fit test panels representing the current us civilian work force," *J. Occupational Environ. Hygiene*, vol. 4, no. 9, pp. 647–659, 2007.
[29] *OBStudio Software*. Accessed: May 22, 2024. [Online]. Available: https://obsproject.com/
[30] FLIR Syst. Inc. *ResearchIR Max Software*. Accessed: May 20, 2024. [Online]. Available: https://www.flir.eu/products/flir-research-studio?vertical=rd+science&segment=solutions
[31] (2024). *Manuel D'utilisation PortaCount Pro 8030/8038*. [Online]. Available: https://tsi.com/getmedia/c8670f72-bd42-4281-9dac-42b09690adb2/8030-8038_PortaCountPro-Manual-FR-6001873?ext=.pdf
[32] M. Arbane, G. Marchais, B. Topilko, Y. Yaddaden, J. Brousseau, X. Maldague, C. Brochot, and A. Bahloul, "Enhanced face mask segmentation on infrared images using lightweight u-net techniques," in *Proc. IEEE Int. Multi-Conference Smart Syst. Green Process-2024*, Apr. 2024, pp. 1–14.
[33] S. Chandaka, A. Chatterjee, and S. Munshi, "Cross-correlation aided support vector machine classifier for classification of EEG signals," *Expert Syst. Appl.*, vol. 36, no. 2, pp. 1329–1336, Mar. 2009.
[34] L. B. White and B. Boashash, "Cross spectral analysis of nonstationary processes," *IEEE Trans. Inf. Theory*, vol. 36, no. 4, pp. 830–835, Jul. 1990.
[35] P. Sedgwick, "Pearson's correlation coefficient," *Bmj*, vol. 345, pp. 1–26, Apr. 2012.

GEOFFREY MARCHAIS received the Master of Engineering (M.Eng.) degree from the École Nationale Supérieure d'Arts et Métiers (ENSAM) and the Master of Science degree (M.Sc.A) in applied sciences from the Université du Québec Ã Rimouski (UQAR), Québec City, Canada. He is currently pursuing the Ph.D. degree with the École de Technologie Supérieure (ETS), Montreal, specializing in the dynamic study of vibrations in suspension seats. His research interests include collaborations with various institutions and experts in mechanical and biomedical engineering.

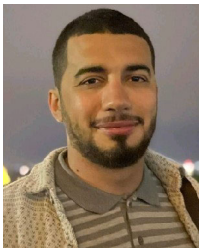

MOHAMED ARBANE (Graduate Student Member, IEEE) received the B.S. degree in electronics from the University of M'sila, Algeria, in 2019, and the master's degree in embedded systems in Algeria. He is currently pursuing the master's degree in engineering with UQAR/Laval, Canada. His research interests include artificial intelligence, deep learning, computer vision, natural language processing, data science, and infrared technology.

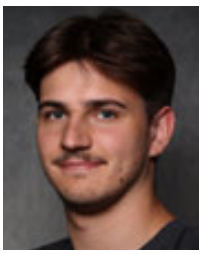

BARTHELEMY TOPILKO received the M.S. degree in engineering from the Université du Québec Ã Rimouski and the Engineering Diploma degree from the Ecole Nationale Supérieure d'Arts et Métiers, in 2024. Since September 2024, he has been a Thermal Engineer with the start-up NAAREA. He is the author of two conference papers (LATAM SHM 2023 and IEEE UBMK 2024). His research interests include CFD and thermal finite element computation and infrared imaging technologies.

JEAN BROUSSEAU received the Ph.D. degree in mechanical engineering from Laval University, Québec City. He is currently a retired Professor with the Université du Québec Ã Rimouski, where he is actively engaged in research as an Associate Professor. He held the NSERC-UQAR Research Chair in design engineering, until 2023. His research interests include mechanical system design, material behavior, finite element modeling and simulation, and industrial applications of 3D metal printing. He is also a member of the Ordre des Ingénieurs du Québec.

CLOTHILDE BROCHOT received the M.S. degree in physics from the University of Lyon 1, France, in 2008, and the Ph.D. degree in process engineering from the University of Lorraine, France, in 2012. She is currently an IRSST Research Professional and an Associate Professor with ÉTS and UQAR. Between 2013 and 2021, she was with IRSST and Concordia University (a Postdoctoral Fellow and a Research Associate) setting up and managing a particle filtration research laboratory. She has worked for both research institutes and companies, mainly in the field of respiratory protection equipment. Her research interests include the protection of workers exposed to airborne contaminants in their working environment, particularly from the point of view of aerosol physics and filtration mechanics.

YACINE YADDADEN is a professor in the Department of Mathematics, Computer Science, and Engineering at the Université du Québec à Rimouski (UQAR). His research focuses on applied artificial intelligence, particularly in computer vision, machine learning, and smart systems.

He holds a B.Sc. and M.Sc. degrees in electrical engineering from the Université des Sciences et de la Technologie Houari Boumediene (USTHB) in Algeria, with a specialization in intelligent and communicating systems. He began his doctoral studies in telecommunications before transitioning to Canada, where he pursued a Ph.D. in information science and technology at the Université du Québec à Chicoutimi (UQAC). His doctoral research centered on the application of artificial intelligence to ambient intelligence in smart homes.

Following his Ph.D., he completed a postdoctoral fellowship at Université Laval, during which he also lectured at UQAR and the Cégep de Limoilou. Since joining UQAR in 2020, he has been actively involved in multidisciplinary research projects, leveraging artificial intelligence to address real-world challenges across various sectors, including health, transportation, and smart environments.

ALI BAHLOUL has been a Researcher with IRSST, since 2005, has developed expertise in the field of industrial ventilation and indoor air quality. He is currently an Associate Professor with the Montréal's École de Technologie Supérieure and Concordia University and an Adjunct Professor with the Université de Montréal. His research interests include anticipate, identify, evaluate, and control exposure to chemical substances and biological agents. His work focuses on developing and validating methods for revaluating ventilation efficiency, studying ventilation system components and aeraulic parameters of emission, and developing and validating source capture devices. He also works on developing and using analytical methods. In addition, he has expertise in hydrodynamic instability, dual diffusion, and heat and mass transfers.

XAVIER MALDAGUE (Life Senior Member, IEEE) received the B.Sc., M.Sc., and Ph.D. degrees in electrical engineering from Université Laval, Québec City, QC, Canada, in 1982, 1984, and 1989, respectively. He has been a Full Professor with the Department of Electrical and Computing Engineering, Université Laval, since 1989, where he was the Head of the Department, in 2003, 2008, 2018, 2023, 2024, and 2025. He has trained over 50 graduate students (M.Sc. and Ph.D.) and has more than 300 publications. His research interests include infrared thermography, nondestructive evaluation (NDE) techniques, and vision/digital systems for industrial inspection. He is a Honorary Fellow of Indian Society of Nondestructive Testing. He is also a fellow of Engineering Institute of Canada Canadian Engineering Institute, the American Society of Nondestructive Testing, and the Alexander von Humbolt Foundation, Germany. He holds the Tier 1 Canada Research Chair in Infrared Vision. In 2019, he was bestowed an Doctor Honoris Causa in Infrared Thermography by University of Antwerp, Belgium.

Annexe B

Titre :
A TestBench for Replicating Human Breathing : Evaluating Thermal Effects of N95 Filtering Facepiece Respirator Leaks – Preliminary Findings

---

Résumé - *Nous décrivons un banc d'essai fermé qui reproduit fidèlement la respiration humaine en contrôlant le débit, la température et la génération de particules grâce à un simulateur pulmonaire ASL5000, une chambre de chauffage thermostatisée et un filtre HEPA. Deux supports interchangeables, une plaque plane en HDPE et une tête artificielle StAH, sont équipés d'orifices calibrés (0,84 et 3,5 mm) afin de créer des scénarios de fuite parfaitement maîtrisés. Les mesures infrarouges (640 * 512 px, 30 Hz) et les tests quantitatifs PortaCount permettent de valider le système : équilibre débit entrant/sortant , exhalation portée à la température corporelle, et moins d'une particule cm-3 à l'intérieur du masque. Les premiers essais montrent qu'une fuite plus large entraîne simultanément une baisse du Fit Factor et un contraste thermique accru. Les limites actuelles concernent l'absence de contrôle d'humidité et l'inertie thermique des mannequins, que nous comptons lever via un modèle multiphysique COMSOL et des tests sur volontaires humains*

Mots clés :
Respirateur N95, Banc d'essai, Simulation de respiration, Thermographie infrarouge, Quantitative Fit Test, Fuites, Tête StAH

A Test Bench for Replicating Human Breathing: Evaluating Thermal Effects of N95 Filtering Facepiece Respirator Leaks – Preliminary Findings

Geoffrey Marchais
Université du Québec a Rimouski,
Rimouski Canada
Geoffrey.Marchais@uqar.ca

Barthelemy Topilko
Université du Québec a Rimouski,
Rimouski Canada

Mohamed Arbane
Université du Québec a Rimouski
Rimouski Canada

Jean Brousseau
Université du Québec a Rimouski
Rimouski Canada

Clothilde Brochot
Université Laval
Québec Canada

Yacine Yaddaden
Université du Québec a Rimouski
Rimouski Canada

Ali Bahloul
Université du Québec a Rimouski
Rimouski Canada
Institut de recherche Robert-Sauvé en santé et en Sécurité du travail
Montréal Canada

Xavier Maldague
Université Laval
Québec Canada

2024 9th International Conference on Computer Science and Engineering (UBMK) | 979-8-3503-6588-7/24/$31.00 ©2024 IEEE | DOI: 10.1109/UBMK63289.2024.10773589

***Abstract*—Following the COVID-19 pandemic, it seemed important to develop alternative methods for verifying the fit of a filtering facepiece respirator (FFR). Infrared technology, promising in the assessment of the fit of a FFR, still requires a thorough study of the thermal effect of a N95 FFR leak. This pilot study aims to design a test bench capable of replicating human breathing as faithfully as possible, focusing on three aspects: breathing airflow, breathing temperature, and particle generation. The humidity aspect is not replicated in this study. To achieve this, the ASL 5000® Breathing Simulator, a heating chamber, and a HEPA filter were employed. These three aspects were validated through various tests on the test bench. The primary objective of this test bench is to assess the thermal impact of different leaks from an N95 FFR on two different test devices designed for this study: a flat model and a Static Advanced Headform (StAH). The thermal impact of the leaks was captured using an infrared (IR) camera. Additionally, a particle counter, the PortaCount® Instrument, was integrated into the test bench to quantify N95 FFR leaks and was used as a reference. In the near future, this test bench will enable the development of methods to locate and quantify N95 FFR leaks, which will subsequently be applied to human subjects.**

***Keywords*—Occupational Health and Safety, Respiratory Protection, Infrared Imaging, Quantitative Fit Testing, Artificial Human Breathing, N95 FFR Leak**

I. Introduction

A. Literature Review

Many issues have been highlighted in the wake of the global COVID-19 pandemic, such as the Filtering Facepiece Respirator (FFR) fit for healthcare professionals. Indeed, before each use of an FFR, the wearer has to carry out a Fit Check, which consists of using different tests (positive pressure and negative pressure tests) to check the airtightness of an FFR. Regli et al. [1] have shown that this Fit Check is unreliable in detecting proper fit or leaks. Before COVID-19, Huh et al. [2] already questioned the accuracy (<50%) of this fit check and showed that a large number of users do not perform an adequate verification.

For N95 FFR, the biggest contributory factor to the loss of protection is a leak through the face seal [3], [4]. This implies that the protection offered by an FFR is significantly affected by the impaired fit between the FFR and the face [5]. Quantitative or qualitative methods can determine FFR fit : Quantitative Fit Test (QNFT) or Qualitative Fit Test (QLFT). These methods are used for training and enable workers to choose the FFR best suited to their face. Furthermore, none of the current methods can identify the position and extent of leaks. It seems essential to find alternative methods to conventional fit testing and fit checking [6] by simplifying, shortening, visualizing and quantifying the N95 leaks, the avenue is to use infrared (IR) technology.

There is relatively little research into using IR imaging to study face seal quality. The principle of using an IR camera to detect seal leaks is based on visualizing changes in facial surface temperature that occur near the FFR face seal and are caused by the flow of hot exhaled air [7]. Dowdall et al. [8] have shown that thermal imaging cameras can detect leaks and assess whether the FFR is properly worn. Roberge et al. [5] experimentally detected exhalation leaks in several subjects using IR imaging. Harber et al. [9] assessed the importance of leaks detected by IR imaging on a four-point scale and established a general relationship between this score and the fit factor (FF). They also showed that it is possible to identify situations with poor FF. According to Harber et al. [9], there is a relationship between FF and leak detection using IR imaging. Still, this study is not sufficient to allow IR imaging to supplant QNFTs. Most recently, Siah et al. [10] have shown that IR imaging has the potential to play a complementary role in FFR Quantitative Fit Testing, particularly with front-line nurses. Chapman et al. [11], as well as, Bari et al. [12] have also demonstrated the capacity of IR imaging to locate N95 FFR leak thank to deep neural network architecture using a PortaCount® instrument as a reference to ensure the presence of a leak or not. However, no study has yet located and quantified automatically leaks detected by IR imaging.

B. Objectives

With the future aim of locating and quantifying an N95 FFR leak, a more detailed study on a leak thermal impact has to be carried out. Objectives of this pilot study are :

- The construction of a test bench reproducing human breathing as faithfully as possible ;
- The design of two test devices wearing an N95 FFR: a flat model and a Static Advanced Headform (StAH) ;
- A preview of the thermal impact of a N95 FFR leak on several leak scenarios.

Indeed, before working with human subjects, it is necessary to work in a controlled environment, with controlled leaks and

a controlled geometry, enabling us to gain a better understanding of the thermal impact of different leak scenarios. Each leak scenario includes one or several leaks, and for each leak, it has got a location and a size.

On one hand, the test bench must accurately replicate human breathing. To accomplish this challenging and complex task, the ASL 5000®, the world's most advanced breathing simulator, will be used in this study. In order to validate its capacity to reproduce human breathing, this test bench must be calibrated and validated.

On the other hand, concerning these two test devices wearing an N95, they must be designed to control the number, location, and size of leaks to assess the thermal impact of different leak scenarios. The FLIR X8501sc Infrared Camera (FLIR Systems, Inc., Wilsonville, Oregon, USA) is used in this study to capture the thermal impact of each leak scenario. In addition, a PortaCount® Instrument Model 8038 (TSI Incorporated, Shoreview, Minnesota, USA) is also used to carry out QNFTs on these two test devices to quantify the severity of leaks. This instrument is used as a reference in this study because healthcare, industrial, agricultural workers and many other users frequently need to carry out QNFT with this instrument. Bergman et al. [13], [14] have already shown the potential of StAH for assessing fit for some N95 FFR models/sizes carrying out a QNFT on a StAH.

II. Modelling and Design

A. Functional Analysis

To accurately replicate human breathing, several key aspects for this study must be considered: the breathing airflow, the breathing temperature, and the number of generated particles. The humidity aspect is not replicated in this study, indeed Topilko et al. [15] have shown that humidity does not have influence on thermal impact on a flat model. To address the first aspect : breathing airflow, the Active Servo Lung (ASL) 5000® Breathing Simulator (IngMar Medical, Pittsburgh, Pennsylvania, USA) was used. This instrument allows for emulating the breathing patterns of a typical adult, with control over breath rate and minute ventilation (Minute ventilation is a measurement of the amount of air that enters the lungs per minute [16]). It operates using a controlled piston mechanism that mimics both inhalation and exhalation. It can create repeatable breath patterns at a high level of accuracy for respiratory device product development with the smart pump

However, the ASL 5000® Breathing Simulator cannot regulate the temperature of breathing. Most machines, such as heated humidifiers, exist to heat the inhaled airflow for humans, but not the exhaled air for a StAH. Consequently, a supplementary system must be devised to heat the exhaled airflow without affecting the temperature of the inhaled airflow. Notably, the investigation of the N95 FFR leak or leaks relies on temperature differentials [7]. These variations stem from disparities between exhalation temperature (approximately at body temperature [5]) and inhalation temperature (at ambient temperature).

Concerning generated particles, it is imperative to establish a sealed and airtight environment to minimise particle dispersion during exhalation. In fact, reducing the number of generated particles will increase the accuracy of the Fit Factor (FF). Therefore, including a filtering component is essential to trap particles generated during inhalation.

Fig. 1 illustrates a simplified closed system that replicates human breathing responding to these three aspects. A valve connection has been engineered to facilitate directional airflow within the system. This Fig. 1 also shows these two test devices, the flat model (1) and the StAH (2), used at the end of the system. These test devices will enable the creation of different leak scenarios, which will be captured thanks to the IR camera.

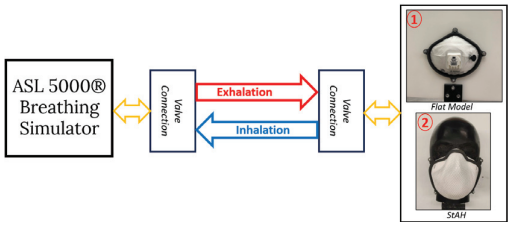

Fig. 1. Overview of the proposed test bench

B. Test Bench

The test bench was designed using a CAO software, SolidWorks ® 2022 (Dassault Systèmes, Waltham, Massachusetts, USA), incorporating all essential components illustrated in Fig. 2.

At the beginning of the system, the ASL 5000® Breathing Simulator (1), is linked to a High Efficiency Particulate Air (HEPA) filter (2) that effectively captures particles within the closed system. Then the airflow traverses a first valve connection (3), crafted with Mask Replacement One-way Valves and 3D-printed components, guiding the flow precisely. Following this path, the airflow enters a heating chamber (4), custom-made with dual incandescent bulbs and twin fans to ensure uniform air heating. The chamber's operation is governed by a precise thermostat, the DIGITEN DHTC-1011 Temperature Controller, ensuring a stable expiring temperature while maintaining the internal temperature below 85°C to safeguard against the degradation of 3D printing components. The heating chamber has a volumetric capacity of 2.5 litres (approximately five exhalations [17]), paired with the 40W heating power of the bulbs. This combination ensures consistent temperature maintenance within the chamber, which is vital for accurate testing protocols with a constant breathing temperature. Exiting the chamber, the airflow encounters another valve connection, linked to both the inhalation flexible, maintained at ambient temperature, and the test device in this picture : the flat model (6).

A wooden board (5) was introduced to the installation to enhance testing precision, effectively isolating the test device from heating elements such as the chamber, the ASL 5000®, and the computers. This isolation facilitates IR visualisation, allowing precise temperature monitoring of N95 leaks. Enabling this visualisation is a fundamental aspect of the test bench. This is made possible by including the IR camera (7), which is widely recognised for its precision, exceptional performance, and high acquisition frequency. It is an essential tool for conducting a thorough study of the thermal impact of a scenario.

C. Test Devices

Once the test bench is built to replicate human breathing, it becomes imperative to design test devices for studying the thermal impact of N95 leak. These test devices, comprising

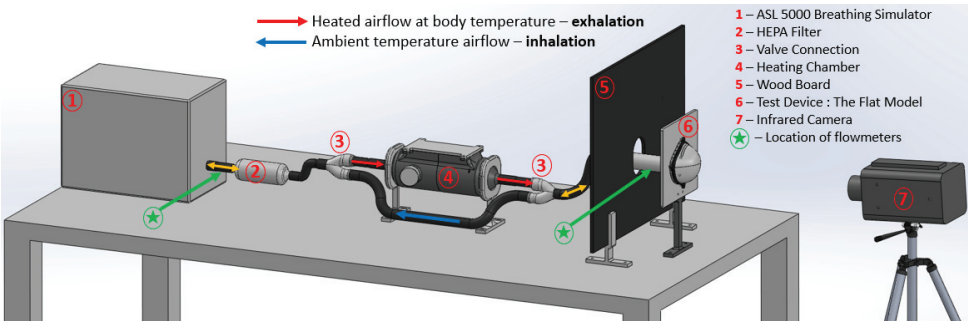

Fig. 2. Complete Test Bench Modelling

a flat model ((1) in Fig. 3) and a StAH ((2) in Fig. 3), must meet specific criteria: controlling the number of leaks, size, and location. High-density polyethylene (HDPE) was selected for the flat model (30cm×30cm) to achieve this. HDPE offers a thermal conductivity ranging between 0,4 and 0,43 $W.m^{1}.K^{-1}$, aligning closely with the skin's thermal conductivity of 0,4 to 0,45 $W.m^{1}.K^{-1}$ [18]. The exact composition of the StAH remains unknown, but it primarily comprises rubber.

Each test device, as depicted in Fig. 3, consists of three components: a holed piece (red), a clamp (green) and an FFR N95 (white), designed to integrate seamlessly with each test device. To achieve this precision, the Creaform3D C-Track 780 HandyProbe scanner (Creaform, Lévis, Quebec, Canada) was employed to scan the StAH and its meshing has been used on SolidWorks® 2022. Furthermore, an N95 geometry has been projected on this meshing to design some pieces which fit perfectly with this StAH. For each case, the holed piece is in contact with the test device, with the flat model, this contact has been carried out with 4 bolts and for the StAH with a fixative silicone.

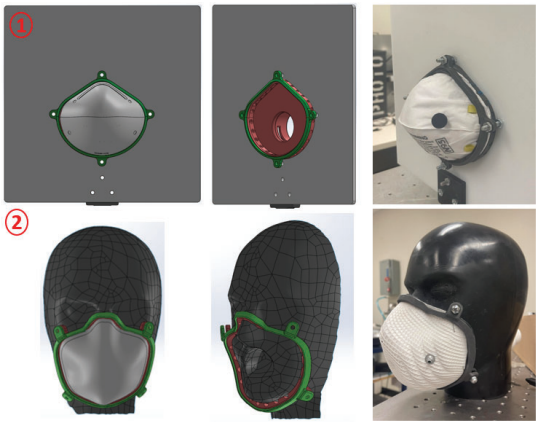

Fig. 3. Modelling and Design of Two Test Devices

On one hand, the holed piece in red in the Fig. 3 enables the creation of diverse leak scenarios, with each scenario specifying the number, size, and location of leaks. The holed piece for each test device is shown in the Fig. 4a for the flat m odel a nd i n t he F ig. 4 b f or t he S tAH. E ach h ole of this piece has a diameter equal to 5 mm and can be plugged with a plug or opened with a tube. Concerning the plug, it is designed with O-ring to ensure airtightness. For the tube, standardised needles have been used to create controlled diameter leaks as have done Rengasamy et al. [19], each standardised tube has been cut and sanded from a standardised needle. Incorporating these standardised tubes with gum in a hole, ranging in diameter from 3.5 mm to 0.84 mm (8G to 18G), with a length equal to 1 cm, it allows variability in leak size. These tubes, during a scenario test, must be tangent to the test device in order to simulate real-life leak situation. On the other hand, the clamp in green in the Fig. 3 secures the N95 FFR onto the perforated piece, ensuring airtightness during testing and thus providing complete control over leaks.

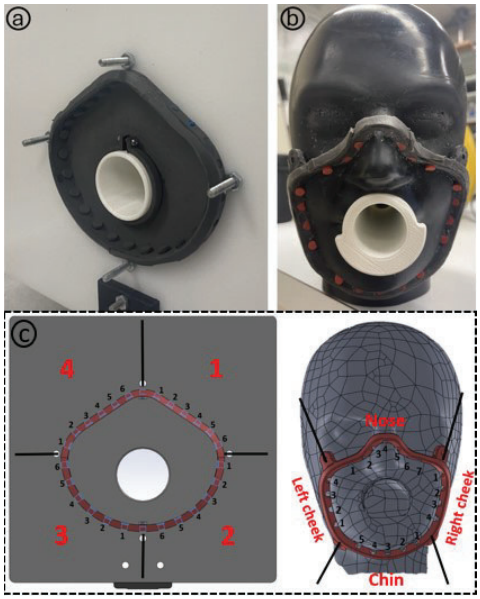

Fig. 4. Control of Number, Size and Location Leak(s)

D. Design and Assembly

Most of the pieces have been printed with the Ultimaker S5 3D Printer (Ultimaker B.V., Utrecht, Netherlands) : valve connections, supports, and plugs. However, the pieces requiring very high print and high-temperature resistance (the heating chamber, holed pieces and clamps) were printed in Nylon on a Formlabs Fuse 1 3D Printer (Formlabs Inc., Somerville, Massachusetts, USA). All pieces that need to be airtight are assembled with hose clips. The final test bench is illustrated in Fig. 5.

III. Experimental Validation

This work is focused on the test bench validation, and this paper is mainly focused on these three aspects : the breathing airflow, the breathing temperature, and a limited number of particles generated.

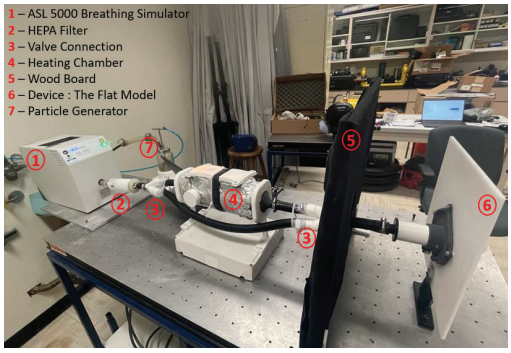

Fig. 5. Final Test Bench

A. Breathing Airflow

An experiment was conducted on the test bench to validate the first aspect. Instead of using the ASL 5000® Breathing Simulator, a constant input flow of pressurised air was employed. The objective of this test was to evaluate the integrity of the closed system and ensure the absence of leaks. Two flowmeters, Model 4040 Series (TSI Incorporated, Shoreview, Minnesota, USA) were strategically placed, spotted by a ($\star$) in the Fig. 2. By monitoring the flow rates at these critical points, we could ascertain the system's airtightness and ability to maintain a consistent airflow without any losses. The test aimed to replicate normal conditions using a flow range of 0-50L/min. A balanced flow between input and output, as illustrated in the Fig. 6, confirmed the absence of leaks in this closed system.

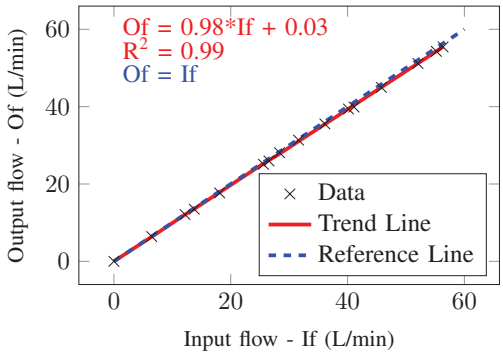

Fig. 6. Output Flow Rate as a Function of Input Flow Rate

B. Breathing Temperature

Once the airflow aspect is validated, assessing the adequacy of the released breathing temperature becomes necessary. To achieve this, it's crucial to replicate normal breathing conditions, encompassing both inhalation and exhalation. Indeed, maintaining a constant airflow using pressurised air, as used in III.A, can only mimic pure exhalation, without replicating the complexities of human respiration. Therefore, to accurately simulate human breathing, it's essential to incorporate mechanisms that enable both inhalation and exhalation, ensuring a realistic representation of breathing temperature. The ASL 5000® Breathing Simulator has been used, and an adult normal pre-recorded scenario in the software has been selected. Then, it is possible to control the Breath rate (Br) and the Minute Ventilation (MV) on the software. MV is calculated using the following formula: 1. A normal adult Br is comprised between 12 and 20 breaths per minute [20] and the mean Tidal Volume TV (the volume of air that moves into and out of the lungs during normal breathing) is around 0.66 Litres for a man [17]. For a breathing rate equal to 15 breaths per minute, MV is equal to :

$$MV = Br \times TV$$
$$MV = 15 \times 0.66 = 10L/min \quad (1)$$

These parameters will be used to simulate normal breathing throughout the study on the ASL 5000® Software. The Fig. 7 shows the pre-recorded breathing pattern used: the instantaneous flow depending on time. It is a periodic but non-sinusoidal cycle, which closely resembles the human breathing cycle [21]. However, the ASL® 5000 software does not provide a mathematical function to characterize this cycle.

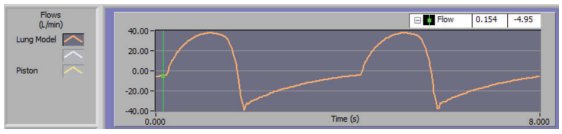

Fig. 7. Breathing Pattern on the ASL 5000 Software

Once this normal breathing setup is completed, it is necessary to adjust the heating chamber thermostat to achieve the final breathing temperature. Unfortunately, thermal sensors have response times that are too slow to measure and follow the temperature changes between inhalation and exhalation. Instead of using sensors, the thermal response was recorded using IR videos of two human subjects wearing an N95 FFR during normal breathing. Indeed, an IR camera has a response time small enough to detect and track the temperature variations of the mean temperature of Region Of Interest (ROI) located on the N95 FFR. By analysing the IR images, with the FLIR software, ResearchIR Max software (FLIR Systems, Inc., Wilsonville, Oregon, USA), it was possible to calibrate the thermostat to control the exhalation temperature. Fig. 8 shows the temperature variations measured on N95 ROI worn by two consenting human subjects and the N95 ROI installed on the flat m odel t est d evice w hen t he t hermostat i s s et to 80°C. As observed in Fig. 8, the temperature differentials ΔT (ΔT=Tmax-Tmin) obtained are quite similar. However, it can also be observed that there is a difference between the breathing patterns. Two elements can be stated to explain those differences. Han et al. [22] have shown that an awareness of the recording of breathing caused an increase of TV. Indeed, a higher tidal volume (TV) results in a greater volume of exhaled and inhaled air, leading to a more intense flow of hot and cold air passing through the N95 mask. This, in turn, causes more significant w arming a nd c ooling effects. Concerning the breath rate, the short difference between the two subjects can be explained by the fact that the breath rate of a human is between 12 and 20 cycles per minute, while a breath rate equal to 15 has been selected in the ASL 5000® Software. Finally, concerning the breathing pattern, Benchetrit [23] has demonstrated the existence of individual variations in breathing patterns among human subjects. This explains the differences in breathing patterns between these two individuals and the selected breathing pattern in the ASL 5000® software.

C. Number of Generated Particles

To address the final aspect, ensuring the absence of generated particles or any particles within the system was crucial.

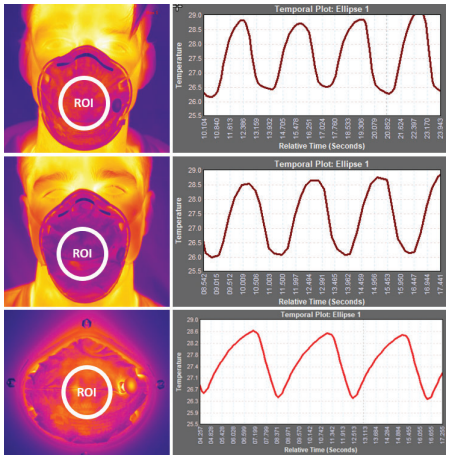

Fig. 8. Temperature Variations of ROI During a Normal Breathing

To achieve this, all openings in the holed piece were sealed thanks to corks to prevent any potential leaks and the ingress of particles. The PortaCount® instrument was used for this purpose, specifically focusing on its real time monitoring tab within the software . This feature enabled us to accurately measure the particle count within the FFR and in the ambient air. Comprehensive tests were conducted using both test devices: the flat model and the StAH. A particle generator, the 24-Jet Collision Nebulizer (BGI Inc., Waltham, USA) (piece (7) in the Fig. 5), has been used to generate enough particles. This control of particle generation is also part of the establishment of a controlled environment, for that a constant pressure (P = 30 PSI) and a constant 2,3% NaCl solution concentration (c=0,05g/mL) a have been used. A minimal presence of particles (around one particle/cm^3) in the N95 FFR using the StAH (Fig. 9) was detected. While there are many particles in ambient air, around 10000 particles/cm^3. The average diameter of the generated particles was less than 100 nanometers. This particle level has been reached for each test to reduce interference. Even if the recommended particle level (1500 particles/cm3) has been exceeded, this high particle concentration does not affect the QNFT results. The FF, which represents the ratio between the number of particles in the ambient air and those within the FFR, enables the assessment of FFR fit. The PortaCount® instrument used in this study has an FF range between 0 and 200. For an N95 FFR, the success criterion to pass a QNFT is an FF higher than 100 [6].

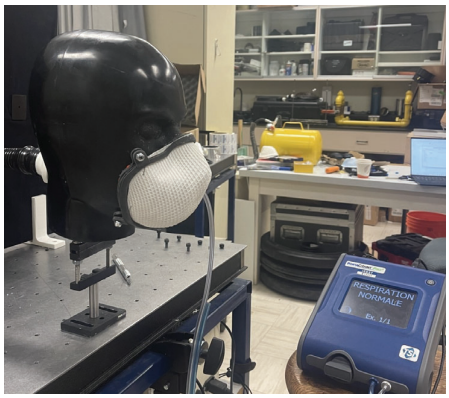

Fig. 9. Validation of Limited Number of Generated Particles

IV. Preliminary Results and Discussion

A. Visualisation

Initial tests can be conducted once the test bench is set up, validated, and capable of simulating human breathing. For each test, a leak scenario is created as described in section II.C, and it can be tested on both devices. The potential leak locations are shown in Fig. 4c. Each device is divided into four quadrants, with each quadrant (red) further subdivided into several holes (black). Each hole can accommodate standardized tubes ranging in diameter from 3.5 mm to 0.84 mm.

For the flat model, only one 30-second IR video is recorded, whereas for the StaH model, four 30-second IR videos are captured in different positions: (a) the front of the face, (b) the right side of the face, (c) the left side of the face, and (d) the bottom of the face mask with the head facing upward. To fully capture the face seal, it is necessary to record four different views [10]. Each video is recorded with a sampling frequency equals to 30Hz, this frequency enables a precise temperature variation monitoring.

Concerning the PortaCount® Instrument, it is used to assign each scenario an FF, enabling the quantification of leak severity. Only one exercise (Normal Breathing) is carried out for 1 minute and 30 seconds. Each scenario underwent a QNFT including this exercise to assign the test an FF.

The Fig. 10 illustrates the necessary views and five different leak scenarios on test devices. Scenarios No 1 and 4 are scenarios without leak on both devices. Whereas scenario No 2,3 and 5 are scenarios with two leaks, these leaks have, in these scenarios a different size. For example, the fifth scenario, two leaks are located in the nose quadrant, the first one in the third hole with a diameter equal to 2.3mm of and the second leak in the fifth hole with a diameter equal to 3.5mm. Unfortunately, the images cannot show the temperature variations over time at the leak locations. However, these temperature variations follow a pattern similar to the Fig.8, with much lower amplitudes.

These first results show that the FF decreases when the size of the leak increases, this agrees well with the results of the studies cited in I.A. A greater thermal impact for a larger leak is also remarkable. These results provide a promising beginning for visualising various leaks according to their number, size, and position.

B. Discussion

Subsequently, a more in-depth study on various leak scenarios will be carried out to assess the influence of the number, location, and size of leaks on the thermally affected area and on the FF. Indeed, in the Fig. 10, a difference in thermal impact between the flat model and the StAH is perceptible, it can be explained by the difference in relief between these two test devices. The upcoming study will enable a better understanding of leaks and the development of methods to locate and quantify N95 leaks. Multiphysics models, using COMSOL Multiphysics® will be developed to validate these future results.

Deep Learning Models will be developed to recognise leak automatically, location and severity. These models on these two test devices will enable the study of the feasibility of detecting efficiently an N95 leak. Once these methods are proven and validated, a study on human subjects will be conducted, with the realisation of a complete database composed of IR videos, RGB videos and QNFTs of human

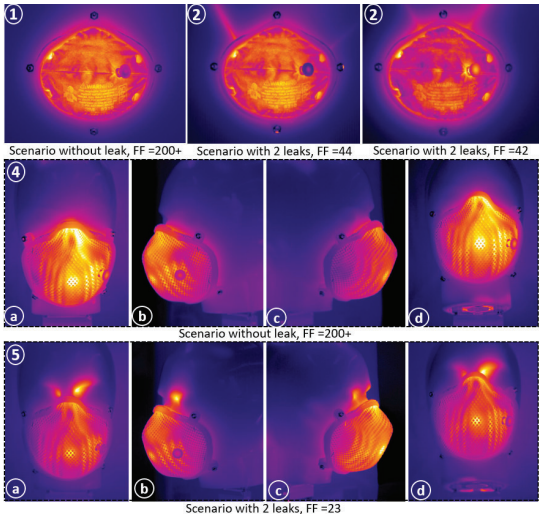

Fig. 10. Different Leak Scenarios with a FF Labelling

subjects wearing an N95. Data will be collected following a detailed protocol.

However, it is important to note that this pilot study is being carried out on two test devices that react differently to heat and temperature variations than a human subject. Moreover, achieving high precision in reproducing human breathing remains a significant c h allenge. E v en w i th t h e A S L 5000, the world's most advanced breathing simulator, the integration of the entire system (comprising the heating chamber and experimental devices) at the simulator's output) impact the thermal effects of leaks.

V. Conclusion

This pilot study shows the implementation of a complete test bench enabling it to reproduce a human breathing. This paper also shows the design of two test devices (a flat model and a StAH) allowing the creation of different leak scenarios with total control of calibrated leak(s) (number, location, size). This test bench combined with these two test devices show that the infrared technology can present many advantages, which could be beneficial f or l eak d etection. I ndeed, a s s hown in first results, the I R t echnology e nables a leak visualisation, a simplification a nd a s hortening o f l eak d etection. This pilot study enables in a near future to work on a potential correlation between the thermal impact of a leak and the FF, this correlation would enable the quantification o f t he l eak. A Multiphysics study will also be carried out in the future to validate the experimental results.

Acknowledgement

This work is supported by the "FFR Protective Devices—Development of an easy-to-use Method to detect leaks and assess face seal tightness using IR Imaging" project, which IRSST (No 2022-0008) and Mitacs (No IT37899) fund under grant agreement.

References

[1] A. Regli, A. Sommerfield, and B. von Ungern-Sternberg, "The role of fit testing n95/ffp2/ffp3 masks: a narrative review," *Anaesthesia*, vol. 76, no. 1, pp. 91–100, 2021.

[2] Y. J. Huh, H. M. Jeong, J. Lim, H. Y. Park, M. Y. Kim, H. S. Oh, and K. Huh, "Fit characteristics of n95 filtering facepiece respirators and the accuracy of the user seal check among koreans," *infection control & hospital epidemiology*, vol. 39, no. 1, pp. 104–107, 2018.

[3] M. Clayton and N. Vaughan, "Fit for purpose? the role of fit testing in respiratory protection," *Annals of Occupational Hygiene*, vol. 49, no. 7, pp. 545–548, 2005.

[4] S. A. Grinshpun, H. Haruta, R. M. Eninger, T. Reponen, R. T. McKay, and S.-A. Lee, "Performance of an n95 filtering facepiece particulate respirator and a surgical mask during human breathing: two pathways for particle penetration," *Journal of occupational and environmental hygiene*, vol. 6, no. 10, pp. 593–603, 2009.

[5] R. J. Roberge, W. D. Monaghan, A. J. Palmiero, R. Shaffer, and M. S. Bergman, "Infrared imaging for leak detection of n95 filtering facepiece respirators: a pilot study," *American journal of industrial medicine*, vol. 54, no. 8, pp. 628–636, 2011.

[6] "1910.134 App A - Fit Testing Procedures (Mandatory). | Occupational Safety and Health Administration." [Online]. Available: https://www.osha.gov/laws-regs/regulations/standardnumber/1910/1910.134AppA

[7] J. Kerl, M. Wenzel, and D. Köhler, "Thermal imaging of mask leakage during pressure-controlled ventilation (bipap therapy)," *Somnologie*, vol. 8, no. 3, pp. 83–86, 2004.

[8] J. B. Dowdall, I. T. Pavlidis, and J. Levine, "Thermal image analysis for detecting facemask leakage," in *Thermosense XXVII*, vol. 5782. SPIE, 2005, pp. 46–53.

[9] P. Harber, J. Su, A. D. Badilla, R. Rahimian, and K. R. Lansey, "Potential role of infrared imaging for detecting facial seal leaks in filtering facepiece respirator users," *Journal of Occupational and Environmental Hygiene*, vol. 12, no. 6, pp. 369–375, 2015.

[10] C.-J. R. Siah, S. T. Lau, S. S. Tng, and C. H. M. Chua, "Using infrared imaging and deep learning in fit-checking of respiratory protective devices among healthcare professionals," *Journal of Nursing Scholarship*, vol. 54, no. 3, pp. 345–354, 2022.

[11] D. Chapman, C. Strong, K. D. Tiver, D. Dharmaprani, E. Jenkins, and A. N. Ganesan, "Infra-red imaging to detect respirator leak in healthcare workers during fit-testing clinic." *IEEE Open Journal of Engineering in Medicine and Biology*, 2023.

[12] A. Bari, R. Lamoureux-Lévesque, A. Ahmed Si, J. Brousseau, A. Bahloul, B. Clothilde, Y. Yaddaden, and X. Maldague, "Covid-19, wearing n-95 masks in clinical environments: Thermographic detection of air leaks," in *Proceedings of the 2022 International Conference on Quantitative InfraRed Thermography*. QIRT Council, 2022.

[13] M. S. Bergman, X. He, M. E. Joseph, Z. Zhuang, B. K. Heimbuch, R. E. Shaffer, M. Choe, and J. D. Wander, "Correlation of respirator fit measured on human subjects and a static advanced headform," *Journal of occupational and environmental hygiene*, vol. 12, no. 3, pp. 163–171, 2015.

[14] M. S. Bergman, Z. Zhuang, D. Hanson, B. K. Heimbuch, M. J. McDonald, A. J. Palmiero, R. E. Shaffer, D. Harnish, M. Husband, and J. D. Wander, "Development of an advanced respirator fit-test headform," *Journal of Occupational and Environmental Hygiene*, vol. 11, no. 2, pp. 117–125, 2014.

[15] B. Topilko, G. Marchais, M. Arbane, J. Brousseau, A. Bahloul, X. Maldague, C. Brochot, and Y. Yaddaden, "Development of multiphysics models for the study of airflow and thermal effects during the use of filtering facepiece respirator," in *2024 9th International Conference on Computer Science and Engineering (UBMK)*, IEEE. unpublished, 2024, pp. 1–6.

[16] S. Hallett, F. Toro, and J. V. Ashurst, *Physiology, tidal volume*. StatPearls Publishing, Treasure Island (FL), 2018.

[17] C. Needham, M. C. Rogan, and I. McDonald, "Normal standards for lung volumes, intrapulmonary gas-mixing, and maximum breathing capacity," *Thorax*, vol. 9, no. 4, p. 313, 1954.

[18] P. J. Rodríguez de Rivera, M. Rodríguez de Rivera, F. Socorro, J. A. Calbet, and M. Rodríguez de Rivera, "Advantages of in vivo measurement of human skin thermal conductance using a calorimetric sensor," *Journal of Thermal Analysis and Calorimetry*, vol. 147, no. 18, pp. 10 027–10 036, 2022.

[19] S. Rengasamy, B. C. Eimer, and J. Szalajda, "A quantitative assessment of the total inward leakage of nacl aerosol representing submicron-size bioaerosol through n95 filtering facepiece respirators and surgical masks," *Journal of occupational and environmental hygiene*, vol. 11, no. 6, pp. 388–396, 2014.

[20] G. Yuan, N. A. Drost, and R. A. McIvor, "Respiratory rate and breathing pattern," *McMaster Univ. Med. J*, vol. 10, no. 1, pp. 23–25, 2013.

[21] A. Scheinherr, L. Bailly, O. Boiron, A. Lagier, T. Legou, M. Pichelin, G. Caillibotte, and A. Giovanni, "Realistic glottal motion and airflow rate during human breathing," *Medical engineering & physics*, vol. 37, no. 9, pp. 829–839, 2015.

[22] J. Han, K. Stegen, M. Cauberghs, and K. Van de Woestijne, "Influence of awareness of the recording of breathing on respiratory pattern in healthy humans," *European Respiratory Journal*, vol. 10, no. 1, pp. 161–166, 1997.

[23] G. Benchetrit, "Breathing pattern in humans: diversity and individuality," *Respiration physiology*, vol. 122, no. 2-3, pp. 123–129, 2000.

Annexe C

Titre :
Poster de participation au Forum Innovation, Ingénierie, Informatique et Entrepreneuriat (FI3E) en 2024 & Poster de participation au 6th Workplace and Indoor Aerosols Conference Angevin Aragonese Castle, May 6-8 2025, Gaeta, Italy 2024

Introduction - *À chaque phase du projet, dès l'obtention de résultats préliminaires, je participe à des colloques et conférences pour recueillir des avis et suggestions en vue d'optimiser notre travail. En 2024, j'ai présenté un poster au FI3E portant sur la segmentation sémantique, puis en 2025 j'ai contribué à WIAC25 avec un support axé sur la corrélation et la détection. Par ailleurs, mon poster FIE3 a été distingué par le premier prix en ingénierie en tant que meilleur poster de recherche.*

AMÉLIORATION DE LA SEGMENTATION SÉMANTIQUE FACIALE EN IR

Mohamed Arbane[1], **équipe de recherche : Geoffrey Marchais**[1],**Barthelemy Topilko**[1], **Yacine Yadadden**[1], **Jean Brousseau**[1], **Xavier Maldague**[2], **Clothilde Brochot**[3], **Ali Bahloul**[3]
[1]Université du Québec à Rimouski (*UQAR*), [2]Université Laval (*ULaval*),
[3]Institut de recherche Robert-Sauvé en santé et en sécurité du travail (*IRSST*)

Problématique

1. La segmentation sémantique avec l'imagerie infrarouge présente des défis spécifiques tels que le faible contraste, le bruit élevé et la sensibilité aux variations des conditions lumineuses
2. Les architectures UNet existantes ont tendance à surajuster, sont intensives en calcul et luttent pour maintenir la précision dans des conditions de faible visibilité [1]

Objectifs

— Le principal objectif est de modifier l'architecture UNet traditionnelle pour mieux s'adapter à l'imagerie infrarouge, en se concentrant spécifiquement sur les tâches de segmentation sémantique.

— Visant à améliorer la précision et l'efficacité informatique de la segmentation sémantique dans les images infrarouges, en particulier pour la détection de masques faciaux dans diverses positions.

— L'intégration de la convolution séparable dans l'architecture UNet réduit la complexité du modèle et améliore la vitesse de traitement sans compromettre les performances.

Bases de données et labellisation

— L'ensemble de données a été développé par notre équipe de recherche dans le cadre d'un sous-projet intitulé 'Partie Expérimentale'. Il comprend des images infrarouges capturées à l'aide d'une caméra FLIR.

— Les images ont été collectées auprès de différentes personnes, incluant une variété de zones et de positions du visage pour assurer la diversité (Fig.1).

— L'ensemble de données inclut des scénarios avec différents types de masques faciaux portés par les sujets, reflétant les conditions réelles.

— L'étiquetage de l'ensemble de données a été réalisé à l'aide de l'outil VGG Image Annotator, dont les détails sont illustrés dans la Fig.2.

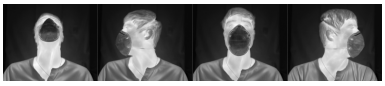

FIGURE 1 – Exemple d'images de la base de données

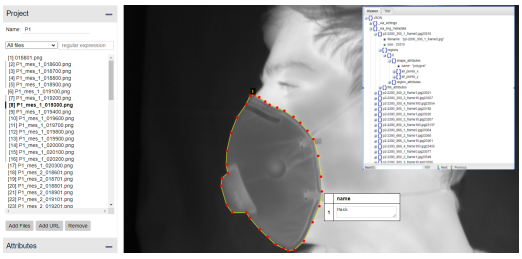

FIGURE 2 – Interface de l'annotateur d'images vgg

Modèle

— Utilise une structure UNet améliorée avec des blocs CNN et des convolutions séparables en profondeur, conçue pour gérer efficacement les tâches de segmentation sémantique dans l'imagerie infrarouge.

— Intègre des connexions directes et une régularisation par dropout au sein de chaque bloc CNN pour améliorer la stabilité de l'apprentissage et permettre des configurations de réseau plus profondes sans augmenter le coût computationnel

— Comprend un chemin de contraction pour le sous-échantillonnage et l'extraction de caractéristiques, ainsi qu'un chemin expansif avec des convolutions transposées pour une localisation précise et un suréchantillonnage.

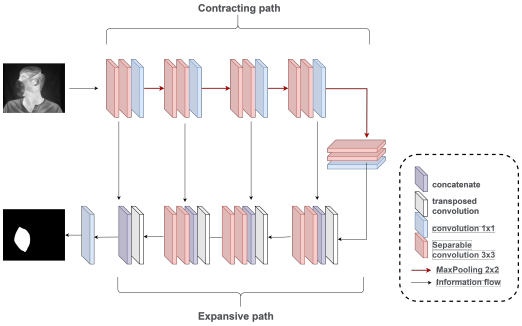

FIGURE 3 – Architecture du modèle proposé

Résultats

TABLE 1 – Comparaison entre la méthode proposée et les méthodes existantes

Method	Accuracy	mIoU	Training Time
Proposed Model	0.98	0.96	441s
Unet	0.98	0.95	660s
Unet++	0.94	0.78	500s
Mask R-CNN+ResNet [2]	0.90	0.89	-

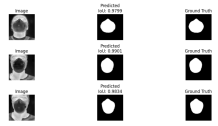

FIGURE 4 – Résultats de la segmentation

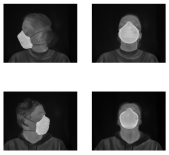

FIGURE 5 – Visualisation de la segmentation

Conclusion

— **Réduction de complexité :** L'intégration des convolutions séparables dans le modèle U-Net réduit le nombre d'opérations nécessaires, le rendant plus rapide et plus léger, idéal pour les applications en temps réel.

— **Utilisation flexible :**Le modèle fonctionne bien même avec de petites quantités de données et réduit la probabilité d'erreurs dues au surajustement.

— **Installation simplifiée :** Grâce à sa structure allégée, le modèle peut être installé et utilisé plus facilement sur de nombreux types d'appareils, facilitant son déploiement généralisé.

— **Travaux futurs – Suivi du masque en temps réel :** Ce modèle pourrait être développé pour suivre le masque en temps réel, même lorsque le porteur est en mouvement. Cela améliorerait significativement la capacité à détecter les fuites autour du masque

Références

[1] Zülfiye Kütük and Görkem Algan. Semantic segmentation for thermal images : A comparative survey. In *Proceedings of the IEEE/CVF Conference on Computer Vision and Pattern Recognition*, pages 286–295, 2022.

[2] Min Zhang, Kai Xie, Yu-Hang Zhang, Chang Wen, and Jian-Biao He. Fine segmentation on faces with masks based on a multistep iterative segmentation algorithm. *IEEE Access*, 10 :75742–75753, 2022.

Next-Gen Respiratory Safety: Synchronizing Thermal Imaging and AI for N95 Leak Assessment

Mohamed Arbane[1],
Yacine Yadadden[1], **Jean Brousseau**[1], **Xavier Maldague**[2], **Clothilde Brochot**[3], **Ali Bahloul**[3]
[1]University of Quebec at Rimouski (*UQAR*), [2]laval university (*ULaval*),
[3]Institut de recherche Robert-Sauvé en santé et en sécurité du travail (*IRSST*)

WIAC2025

Motivation & Objectives

→ **Problem :** Minor Filtering facepiece respirator N95 (FFR N95) leaks drastically reduce protection.

→ **Gap 1 :** Current leak detection methods are limited : no localisation, no quantification, no visualisation, no automation.

→ **Gap 2 :** The fit test (PortaCount®) must be performed by user before wearing a mask, yet its reliability is low and it demand specific skills and time

→ **Objective :** To develop an automated, robust, real-time system that detects and accurately localizes leaks in FFR N95 using infrared imaging, deep learning, and advanced segmentation techniques.

Experimental Design

1. **Controlled Mannequin Tests :**
   → Artificially introduced leaks of known sizes (8G–18G).
   → PortaCount® as the normative reference for fit quantification.

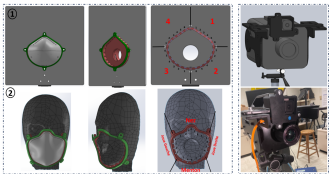

Figure 1 – Controlled Mannequin Setup

2. **Human Subject Trials :**
   → Natural head movements, varied facial shapes.
   → Ethical approval : consent and protocol for data collection
   → Real-time IR video capture and portacount fit factors [1]

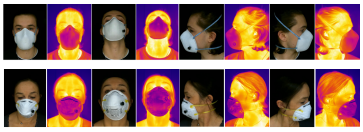

Figure 2 – Human Subject Trial Configuration

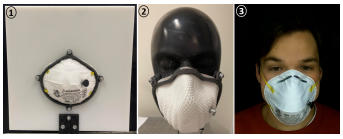

Figure 3 – Overall Dataset Overview

Segmentation Pipeline

— **Initial Segmentation :**
Applied a custom lightweight U-Net model specialized for infrared mask segmentation to define the mask boundary accurately.[2]

— **Dynamic Segmentation :**
Leveraged Segment Anything Model 2 (SAM2) prompted by U-Net outputs to dynamically track mask contour movements in real-time.

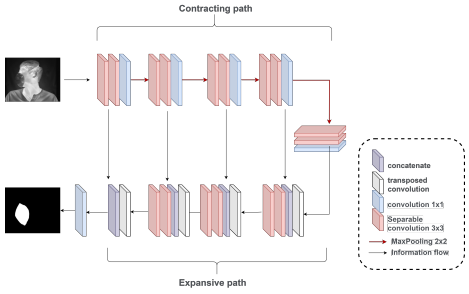

Figure 4 – the proposed U-Net Architecture

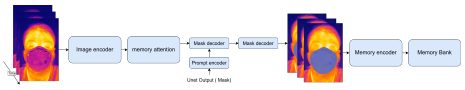

Figure 5 – Dynamic Segmentation with SAM2

Feature Extraction & Classification

— **Spectrogram Generation :** FFT on temperature signals along contour.
— **ResNet50** : deep feature embeddings.
— **SVM Classifier :** Leak vs. No-Leak decision boundary.

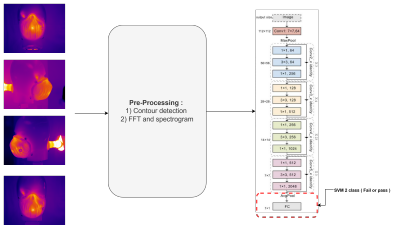

Figure 6 – ResNet50+SVM Classification Model

Correlation-Based Localization

— Contour into 100 ROIs.
— Extract FFT signal per ROI center region.
— Compute Pearson as correlation method
— Highlight top-correlated ROI(s) as leak site(s).

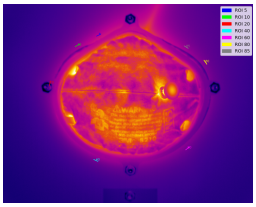

Figure 7 – Example of ROI Extraction and Highlighting

Results

Table 1 – Segmentation Performance Comparison

Method	Accuracy	mIoU	Training Time
Proposed Model	0.98	0.96	441s
Unet++	0.94	0.78	500s
Mask R-CNN+ResNet	0.90	0.89	-

Table 2 – Key results of the proposed leak detection and localization pipeline

Scenario	Precision	F1-Score	Localization Accuracy
controlled environment	0.98	0.97	$> 95\%$ ROIs within ± 5 segments
Human subjects	0.95	0.94	$\rho > 0.85$ flags true leaks

Conclusion & Future Work

— **Conclusion :** Pipeline enables scalable, non-invasive, continuous fit-checking of N95s.
— **Next Steps :**
  — **Quantitative Leak Mapping :** Integrate area-based metrics to quantify leak size and spatial distribution around the entire mask contour, enabling severity scoring and threshold alarms.
  — **Dedicated Detection Station :** Design and build a turnkey infrared/AI-powered fit-testing kiosk—complete with guided user interface.

References

[1] Geoffrey Marchais, Barthelemy Topilko, Mohamed Arbane, Jean Brousseau, Clothilde Brochot, Yacine Yaddaden, Ali Bahloul, and Xavier Maldague. A test bench for replicating human breathing : Evaluating thermal effects of n95 filtering facepiece respirator leaks – preliminary findings. In *2024 9th International Conference on Computer Science and Engineering (UBMK)*, pages 695–700, 2024.

[2] Mohamed Arbane, Geoffrey Marchais, Barthelemy Topilko, Yacine Yaddaden, Jean Brousseau, Clothilde Brochot, Ali Bahloul, and Xavier Maldague. Advanced infrared face mask segmentation using a custom lightweight u-net model. In *2024 IEEE International Multi-Conference on Smart Systems Green Process (IMC-SSGP)*, pages 1–6, 2024.

Bibliographie

[1] Aicha BARI et al. « Covid-19, wearing N-95 masks in Clinical Environments : Thermographic Detection of Air Leaks ». In : *16th Quantitative InfraRed Thermography Conference*. 2022.

[2] D. CHAPMAN et al. « Infrared thermography and machine learning for leak detection in P2 respirators ». In : *Scientific Reports* (2023). Protocol improvements et détection des fuites sur le masque.

[3] Darius CHAPMAN et al. « Infra-Red Imaging to Detect Respirator Leak in Healthcare Workers During Fit-Testing Clinic ». In : *IEEE Open Journal of Engineering in Medicine and Biology* 5 (2024), p. 198-204. DOI : 10.1109/OJEMB.2023.3330292.

[4] Darius CHAPMAN et al. « Personalized 3D-printed frames to reduce leak from N95 filtering facepiece respirators : A prospective crossover trial in health care workers ». In : *Journal of Occupational and Environmental Hygiene* 20.7 (2023), p. 304-314.

[5] Y. CHENG et al. « Face masks effectively limit the probability of SARS-CoV-2 transmission ». In : *Science* 372.6549 (2021), p. 1439-1443. DOI : 10.1126/science.abg6296.

[6] S Jakob CLAPHAM et al. « Comparison of N95 disposable filtering facepiece fits using Bitrex qualitative and TSI Portacount® quantitative fit testing ». In : *International journal of occupational and environmental health* 6.1 (2000), p. 50-54.

[7] J.C. CORBIN, G.J. SMALLWOOD et P.R. LEROUEIL. *Systematic experimental comparison of particle filtration efficiency of respiratory masks*. 2021. arXiv : 2108.13620 [physics.med-ph].

[8] N. F. DEGESYS et AL. « Correlation between N95 extended use and reuse and fit failure in an emergency department ». In : *JAMA* (2020).

[9] Centers for DISEASE CONTROL et PREVENTION. *Laboratory Performance Evaluation of N95 Filtering Facepiece Respirators*. 2008. URL : https://cdc.gov.

[10] Ethan D FECHTER-LEGGETT et al. « Estimated N95 Respirator Needs for Nonhealthcare Essential Workers in the United States During Communicable Respiratory Infectious Disease Pandemics ». In : *Health security* 20.2 (2022), p. 127-136.

[11] André F GIRÃO et al. « Localization of Air Leaks Using an Infrared Thermography Camera : An Experimental Study ». In : *Design, Simulation, Manufacturing : The Innovation Exchange*. Springer. 2025, p. 192-200.

[12] P. HARBER et al. « Potential role of infrared imaging for detecting facial seal leaks in filtering facepiece respirator users ». In : *Journal of Occupational and Environmental Hygiene* 12.6 (2015), p. 369-375. DOI : 10.1080/15459624.2015.1006636.

[13] Prasanna HARIHARAN et al. « A computational model for predicting changes in infection dynamics due to leakage through N95 respirators ». In : *Scientific reports* 11.1 (2021), p. 10690.

[14] Kaiming HE et al. « Deep residual learning for image recognition ». In : *Proceedings of the IEEE conference on computer vision and pattern recognition*. 2016, p. 770-778.

[15] Jin HUANG et Charles X LING. « Using AUC and accuracy in evaluating learning algorithms ». In : *IEEE Transactions on knowledge and Data Engineering* 17.3 (2005), p. 299-310.

[16] TSI INCORPORATED. *How technology enables PortaCount Respirator Fit Testers to fit test any respirator*. 2024. URL : `https://tsi.com`.

[17] Center for INFECTIOUS DISEASE RESEARCH et Policy (CIDRAP). *Study finds no significant difference between N95 and surgical masks*. `https://www.cidrap.umn.edu/news-perspective/2023/03/study-finds-no-significant-difference-between-n95-and-surgical-masks`. 2023.

[18] Zheng JIANG et al. « Combining visible light and infrared imaging for efficient detection of respiratory infections such as COVID-19 on portable device ». In : *arXiv preprint arXiv :2004.06912* (2020).

[19] Hyunjin KIM et al. « Thermal imaging and deep learning-based fit-checking for respiratory protection ». In : *Scientific Reports* 14.1 (2024), p. 24407.

[20] Natalia KOWALCZYK, Jacek RUMIŃSKI et Magdalena MAZUR-MILECKA. « Improving the quality of respiratory signals extracted from the segmented mask area ». In : *Biocybernetics and Biomedical Engineering* 45.3 (2025), p. 457-468.

[21] Marcin KOWALSKI et Krzysztof MIERZEJEWSKI. « Detection of 3D face masks with thermal infrared imaging and deep learning techniques ». In : *Photonics Letters of Poland* 13.2 (2021), p. 22-24.

[22] Geoffrey MARCHAIS. « Localisation et quantification des fuites d'un masque n95 par imagerie infrarouge : développement d'installations pour l'étude expérimentale des fuites d'un masque n95 sur des systèmes à complexité croissante ». Thèse de doct. Université du Québec à Rimouski, 2024.

[23] Geoffrey MARCHAIS et al. « A Test Bench for Replicating Human Breathing : Evaluating Thermal Effects of N95 Filtering Facepiece Respirator Leaks – Preliminary Findings ». In : *2024 9th International Conference on Computer Science and Engineering (UBMK)*. 2024, p. 695-700. DOI : 10.1109/UBMK63289.2024.10773589.

[24] Geoffrey MARCHAIS et al. « SafeRespirator : Comprehensive Database for N95 Filtering Facepiece Respirator Leak Detection Including Infrared, RGB Videos, and Quantitative Fit Testing ». In : *IEEE Access* (2024).

[25] Public Health ONTARIO. *Medical Masks versus N95 Respirators for Preventing COVID-19 among Health Care Workers : A Review of the Comparative Clinical Effectiveness*. https://www.publichealthontario.ca/-/media/Documents/nCoV/ipac/2022/04/covid-19-medical-masks-n95-respirators.pdf. 2022.

[26] Keiron O'SHEA et Ryan NASH. « An introduction to convolutional neural networks ». In : *arXiv preprint arXiv :1511.08458* (2015).

[27] P.V. PERSSON. *Side-leakage of facemask*. 2021. arXiv : 2105.03088 [physics.flu-dyn].

[28] Micah DJ PETERS. « N95 respirators for health care workers : the importance of fit, comfort, and usability ». In : *The Medical Journal of Australia* 217.2 (2022), p. 83.

[29] L.J. RADONOVICH et al. « N95 respirators vs medical masks for preventing influenza among health care personnel ». In : *JAMA* 322.9 (2019), p. 824-833. DOI : 10.1001/jama.2019.11645.

[30] A. REGLI et B. S. von UNGERN-STERNBERG. « The role of fit testing N95/P2 masks : a narrative review ». In : *Anaesthesia* (2020).

[31] R. J. ROBERGE et al. « Infrared imaging for leak detection of N95 filtering facepiece respirators : a pilot study ». In : *American Journal of Industrial Medicine* 54.8 (2011), p. 628-636. DOI : 10.1002/ajim.20970.

[32] Raymond J ROBERGE et al. « Infrared imaging for leak detection of N95 filtering facepiece respirators : a pilot study ». In : *American journal of industrial medicine* 54.8 (2011), p. 628-636.

[33] Jean SCHMITT et Jing WANG. « A critical review on the role of leakages in the facemask protection against SARS-CoV-2 infection with consideration of vaccination and virus variants ». In : *Indoor air* 32.10 (2022), e13127.

[34] C.-J. Rosalind SIAH et al. « Using infrared imaging and deep learning in fit-checking of respiratory protective devices among healthcare professionals ». In : *Journal of Nursing Scholarship* 54.3 (2022), p. 345-354. DOI : 10.1111/jnu.12736.

[35] A. SMITH et B. JONES. « The adequacy of user seal checking for N95 respirators compared to fit testing ». In : *Journal of Hospital Infection* (2022).

[36] Jeffrey D SMITH et al. « Effectiveness of N95 respirators versus surgical masks in protecting health care workers from acute respiratory infection : a systematic review and meta-analysis ». In : *Cmaj* 188.8 (2016), p. 567-574.

[37] Mupparaju SOHAN, Thotakura SAI RAM et Ch Venkata RAMI REDDY. « A review on yolov8 and its advancements ». In : *International Conference on Data Intelligence and Cognitive Informatics*. Springer. 2024, p. 529-545.

[38] Maddison STRICKLING et al. « A comparison of fit, heat stress, oxygen saturation and comfort between a novel reusable mask and disposable N95 respirator ». In : *PloS one* 20.4 (2025), e0321538.

[39] UNKNOWN. *Infra-Red Imaging to Detect Respirator Leak in Healthcare Workers*. PMC article summary. confirming enhanced sensitivity via IR imagery and limitations in flow quantification. 2023.

[40] F. WANG. « Evaluation of the performance of respiratory protective devices ». In : *International Journal of Respiratory Protection* (2024).

[41] Xiaodan XU et al. « Conducting quantitative mask fit tests : application details and affecting factors ». In : *Frontiers in Public Health* 11 (2023), p. 1218191.

[42] Z. ZHUANG et al. « Recommended test methods and pass/fail criteria for a respirator fit capability test of half-mask air-purifying respirators ». In : *Journal of Occupational and Environmental Hygiene* (2017).